"Si ringraziano specialmente:

i genitori per avermi sempre sostenuto e guidato col loro esempio in questi anni, tutti quegli amici con cui ho condiviso fantastiche esperienze ma che ci sono anche sempre stati nei momenti difficili.

Un grazie speciale va anche al Professor Fernando Briz per la sua infinita pazienza e dedizione nel seguirmi, e a tutti i ragazzi del laboratorio per il tempo che sempre mi hanno dedicato incondizionatamente."

University of Padova

Department of Electrical Engineering
Padova, Italy

Master's Thesis

Sensorless Control of an Interior Permanent Magnet Synchronous Motor in all the Speed Range, Including Position Control

Supervisor: Ch.mo Prof. Nicola Bianchi

Co-supervisor: Ch.mo Prof. Fernando Briz

Student: Giorgio Valente

Academic year

2013 - 2014

Contents

Abstract

A drive can be defined as a system capable to produce and control the motion of a mechanical element, called load. Each drive includes an organ of power, said actuator, capable to produce mechanical work and to transmit it to the load. This can be hydraulic, pneumatic,piezoelectric or electric. The field of electrical engineering makes use of electric actuators, and for this reason it is called electric drive.
An electric drive makes use of position sensors (encoders) to control the machine. These are quite bulky devices that are applied to the shaft of the machine to measure instantaneously its position and speed. This device strongly affects the price, the reliability and the inertia of the electric drive.
The objective of this thesis is the study and the implementation of sensorless control techniques in order to remove the position sensor and, consequently, to avoid its negative aspects. The developed sensorless control technique is applied to the electric drives using permanent magnet synchronous motors (PMSM). In particular, the control has been developed using two techniques: one designed for medium to high speeds and the other suitable for low and zero speed, including position control. Both techniques are combined in order to operate over the entire speed range of the motor.
The first chapter contains the bibliographic research that has been done in order to understand the state of the art in the field of sensorless control.
The following chapters, then,show the results of the implementation that has been done as simulation using Simulink, a Matlab toolbox. In particular, Chapter 2 contains the theoretical aspects and the simulation results regarding medium to high operating speed while Chapter 3 deals with low and zero speed, including position control. In Chapter 4 the simulation results of the combination of the two techniques is then presented.
Finally, as for the experimental verification, unfortunately the whole speed-range sensorless control combining both methods could not be completed due to time restrictions. The last chapter (Chapter 5) contains the experimental results showing full sensorless control in the medium-high speed range. As regards low and zero speed, only preliminary experimental results are shown, since the implementation of all the signal processing needed for full sensorless control could not be completed.

Versione italiana:

Un azionamento puo' essere definito come un sistema in grado di produrre e controllare il movimento di un elemento meccanico, chiamato carico. Ciascun azionamento comprende un organo di potenza, detto attuatore, in grado di produrre lavoro meccanico e di trasmetterlo al carico. L'attuatore puo essere idraulico, pneumatico, elettrico o piezoelettrico e il settore dell'ingegneria elettrica fa uso esclusivamente di quelli elettrici, e per questo motivo si parla appunto di azionamenti elettrici.
Un motore elettrico fa uso di sensori di posizione (encoder) per controllare il motore. Questi dispositivi vengono applicati all'albero della macchina per misurare istantaneamente la posizione e la velocita'; hanno lo svantaggio di essere piuttosto ingombranti e di influenzare fortemente il prezzo, l'affidabilita' e l'inerzia del motore elettrico.
L'obiettivo di questa tesi e' lo studio e l'implementazione di tecniche di controllo sensorless per rimuovere il sensore di posizione. La tecnica sensorless sviluppata viene applicata agli azionamenti elettrici con motori sincroni a magneti permanenti (PMSM). In particolare, il controllo e' stato sviluppato utilizzando due metodi: uno in grado di operare con velocita' medio - alte e l' altro adatto a velocita' basse o nulle. Quest'ultima tecnica sensorless e' adatta quindi anche per il controllo di posizione ed entrambe le tecniche sono poi combinate al fine di poter operare nell'intero campo di velocita' del motore.
Il primo capitolo contiene una ricerca bibliografica, compiuta per comprendere lo stato dell'arte nel campo del controllo sensorless. I capitoli successivi, poi, mostrano i risultati dell'implementazione eseguita a livello di simulazione con Simulink, un toolbox di Matlab. Piu' precisamente, il secondo capitolo contiene gli aspetti teorici ed i risultati della simulazione del metodo operante a velocita' medio - alte mentre il terzo capitolo tratta il metodo destinato a velocita' basse o nulle, compreso il controllo di posizione. Nel quarto capitolo sono poi presentati i risultati delle simulazioni in cui le due tecniche sensorless vengono combinate, per poter operare nell'intero campo di velocita' del motore.
Infine, per quanto riguarda la verifica sperimentale, non e' stato completato, per mancanza di tempo, il controllo sensorless nell'intero range di velocita'. Nel quinto capitolo sono comunque presenti i risultati sperimentali che mostrano il controllo sensorless nel range di velocita' medio-alta e risultati sperimentali preliminari per quanto riguarda la tecnica operante con velocita' basse o nulle.

In the following table all the acronyms that have been used in this thesis work are listed.

Acronysm	**Complete Name**
PMSM	Permanent Magnet Synchronous Machine
BLAC	Brush-Less Alternating Current
SPMSM	Superficial Permanent Magnet Synchronous Machine
IPMSM	Interior Permanent Magnet Synchronous Machine
IM	Induction Machine
MBST	Model Based Sensorless Technique
HFIST	High Frequency Injection Sensorless Technique
MTPA	Maximum Torque Per Ampere
MRAS	Model Reference Adaptive System
EMF	Electromotive Force
EKF	Extended Kalman Filter
PLL	Phase-Lock Loop
LPF	Low-Pass Filter
HPF	High-Pass Filter
BSF	Band-Stop Filter
PWM	Pulse-Width Modulation
FFT	Fast Fourier Transormate
DSP	Digital Signal Processor
IGBT	Insulated-Gate Bipolar Transistor

Introduction

In the last few decades there has been a drastic change of course in the global energetic context. It has been noticed that the planet is running out of energy resources because of its indiscriminate exploitation.In addition, the massive use of fossil fuels has resulted in a rate of pollution that has reached alarming levels. Among the energy policies that have been proposed to reverse this negative trend, certainly energy efficiency is one of the most promising. This is based on the simple principle stating that the best energy is the saved one. To this regard, figure 1 shows the development of primary energy demand in Europe, in which the quantity "negajoules" represents the saved energy. It is interesting to notice that the "negajoules" significantly increased in the last few decades due to a global awareness of the problem.

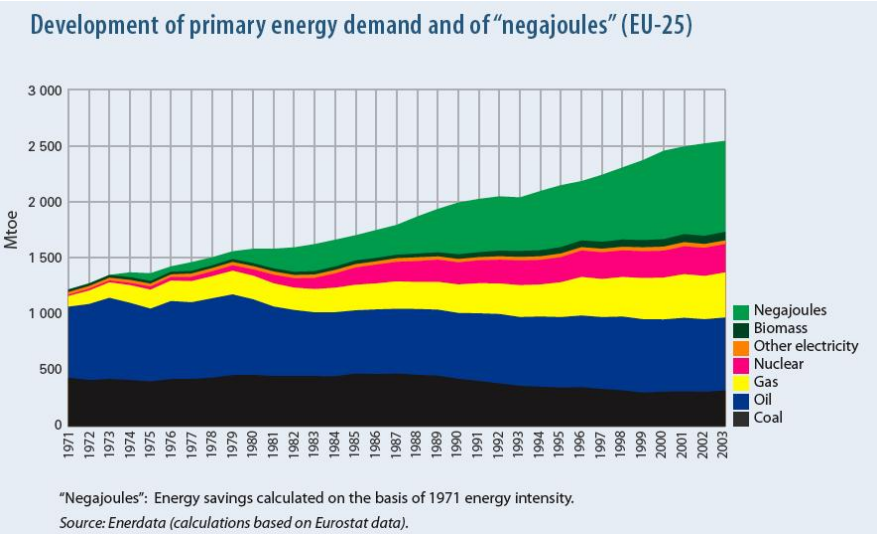

Figure 1: Development of energy demand in Europe [16]

In this regard, there has been an impressive increase in the use of electric motors that are definitely more efficient than the internal combustion engines

(ICE). And in particular, among the different electric motors designs, the permanent magnet synchronous machine (PMSM) has received increasing attention in recent years. PMSM presents higher efficiency than other machine designs because, as it is well known, the excitation of these is provided by the permanent magnets. The only flaw is the high cost that the raw materials and the manufacturing of permanent magnets have recently reached. In fact, excluding the magnets made of ferrite used for low power applications, almost all of these motors use rare earths including samarium cobalt (SmCo) and Neodymium magnet (NdFeB) which,in recent years, have become a monopoly of Chinese manufactures.This is the reason why China, taking advantage of this situation, has ballooned the cost of these magnets.
Despite these economic difficulties, in recent years the research has focused more on these kinds of motors. In particular, thanks to the exponential growth of digital processors able to implement in real time the required calculations and control algorithms, and power electronics able to transmit to the machine the required voltages/currents, these motors are associated with a control. The result of this combination of devices is called electric drive. Figure 2 is a simple but effective block diagram with the essential elements which constitute the electric drive.

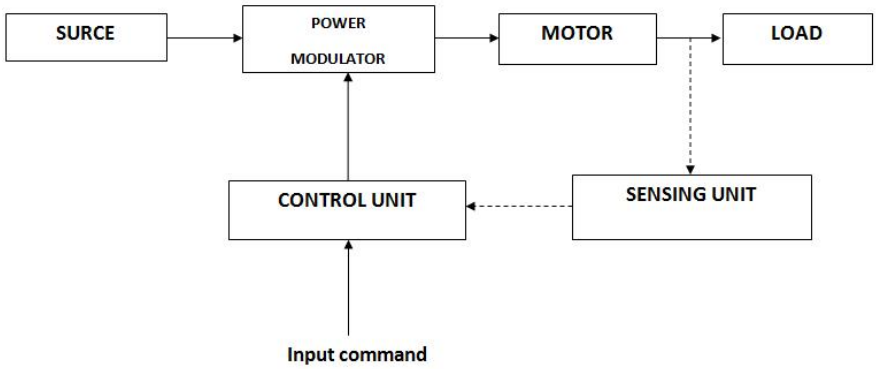

Figure 2: Constitutive elements of an electric drive

An electric drive is therefore a complex set of elements, carefully designed and assembled to precisely and efficiently control the torque/motion produced by the electric machine. It is interesting to realize, in this regard, the different engineering fields that it includes. This is schematically represented in the diagram of figure 3.

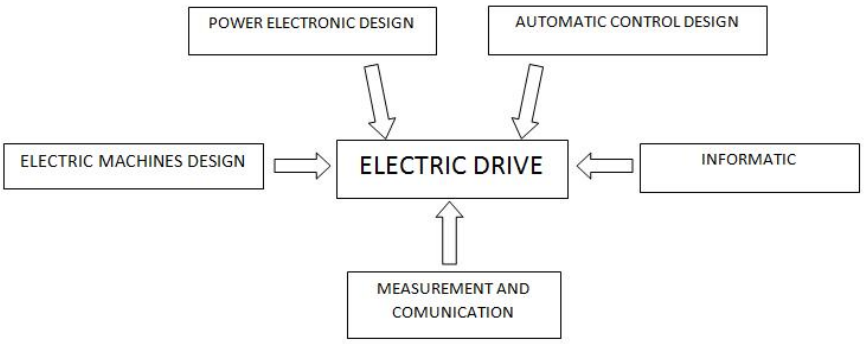

Figure 3: Engineering fields necessary to design an electric drive

Figure 4 shows the main elements of an electric drives with a permanent magnet synchronous motor (PMSM). It is observed that there is a position sensor, which is typically an encoder, attached to the motor shaft which has the function of providing the rotor position (and therefore the magnet position) in real time. Knowledge of the magnet and rotor position will be needed to control the torque produced by the machine, as well as for motion (speed and position) control.

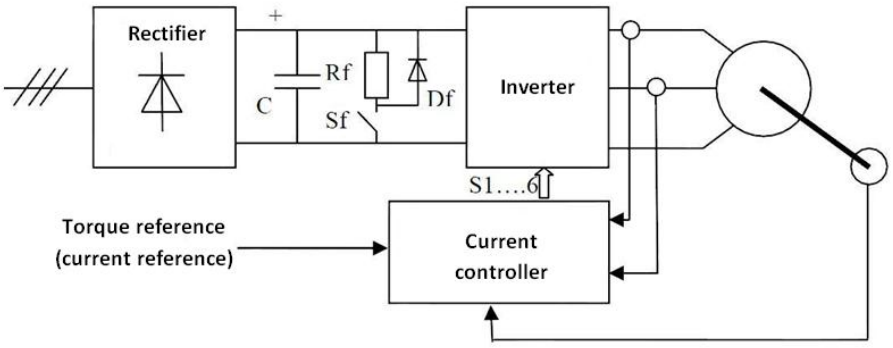

Figure 4: Traditional electric drive using the encoder [15]

The development of methods to eliminate the position sensor has been an intensive line of research in the field of electrical drives for the last two decades. A reason for this is that the cost of this device is relatively large especially for small and medium power drives, having therefore a determinant impact on the final cost of the product. Furthermore, the cabling required to transmit the measured velocity (or position) from the motor to the control can compromise the reliability of the machine drive and further increase the cost. In addition, for special applications where a very low inertia is required or the available space is

limited, the presence of an encoder becomes annoying. Electric drives on which control of the electromechanical system is not based on direct measurements of velocity or position, but it is provided by means of the estimators (or observers) are called "sensorless electric drives" . In these drives the position of the rotor and its angular speed are obtained through the measurement and processing of the three-phase currents and/or voltages (see figure 5).

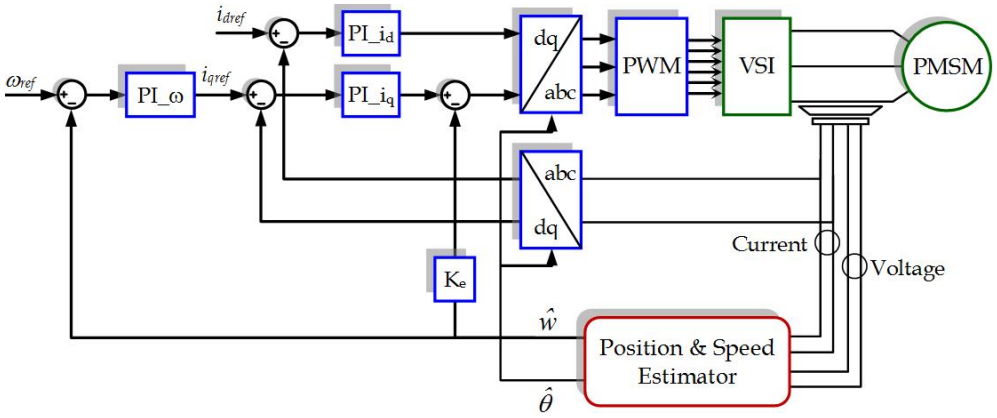

Figure 5: Sensorless electric drive

Sensorless electric drives can also be divided depending on the speed at which the machine is working: in particular, for medium-high speeds, the estimation of the angular speed and of the position can be made using the fundamental equations of the machine, from which is possible to get a quantity (the back electromotive force) that contains the desired information. This type of techniques are often called Model-Based sensorless techniques (MBST).
The EMF varies proportionally to the speed of the rotor and consequently below certain speeds it becomes too small to make an accurate estimate of the motor speed, due to the influence of the parameter-estimation error and to the measurement noise.
For low and zero speed, alternative techniques must be used in order to track the speed and the position of the rotor. In salient machines (IPMSM), voltage test signals can be injected and the resulting currents are processed to obtain a rotor position estimate based on intrinsic salience of the rotor, independent from the back EMF and model parameters. The test signal can be a continuous high-frequency (HF) voltage, discrete voltage pulses, or modified pulse width-modulation (PWM) pulses. These methods work by tracking the intrinsic salience of the machine arising from the difference between the d- and q-axis inductance and they are called High Frequency Injection sensorless techniques (HFIST). Even for surface-mount permanent magnet (SMPM) machines, normally considered nonsalient, the difference arising from the saturation induced by the rotor magnets to the stator-teeth iron is sufficient to yield robust position estimates.
However, injection methods have two disadvantages: at higher speeds the additional voltage needed for signal injection becomes a restriction and the HF currents cause unnecessary losses in the motor.

Another problem is that the HF methods can only track the position of the d-axis, but not the magnet polarity. So,in order to start up the drive, some strategy to detect the magnet polarity must be implemented. One means to get this information consists in the injection of a voltage pulse in both directions of the d-axis. Such voltage pulses are generated by the inverter. It is then possible to recognize polarity of the magnets from the maximum values of the resulting current [6].
As it has been mentioned before, high frequency injection sensorless techniques can be applied to both surface-mount and interior permanent magnet synchronous machine. In this thesis, only interior permanent magnet synchronous machines (IPMPM) are considered.
Finally, the combination of the salience- and the EMF-based estimation method is needed to achieve wide-speed operation including standstill for sensorless permanent magnet synchronous motor (PMSM). In this thesis work, several hybrid solutions found in the literature will be considered, and one will be chosen and implemented as starting point for the wide-speed range implementation.

CHAPTER 1

THEORETICAL ASPECTS

1.1. Introduction

This chapter deals with the theoretical aspects of this thesis. In particular, after a quick summary of the fundamental equations of the PMSM, a review of the model based methods and high frequency signal injection methods that have been proposed for the rotor position and speed estimation will be presented, including the physical and mathematical background. Then, in the chapters dedicated to the simulations of both methods, the details for the selected methods will be given.
Finally, the last part of the chapter will focus on the hybrid techniques that combine MBSTs with HFISTs in order to operate in the whole speed range. Therefore this part is the result of the bibliographic research that has been done.

1.2. PM machine model

In this section a quick overview of the fundamental equations of PM machines is given in order to give to the reader the basics to understand the matters that will be treated later. Both Surface Permanent Magnet (SPMSM) and Interior Permanent Magnet Synchronous Machines (IPMSM) will be considered.
The voltage equation for a SPMSM in the stationary reference frame is

$$v^s_{dq} = Ri^s_{dq} + L\frac{di^s_{dq}}{dt} + j\omega_r\psi^s_{pm} \tag{1.1}$$

where R is the stator resistant, $L = L_{ss}+|L_{Mss}|$ is the synchronous inductance, with L_{ss} and L_{Mss} the auto and mutual inductance respectively, which, as the machine is isotropic, are equal for the three phases.

This equation can be rewritten making explicit its real ($d^s - axis$) and imaginary ($q^s - axis$) components:

$$\begin{aligned} v_d^s &= Ri_d^s + L\frac{di_d^s}{dt} + j\omega_r\psi_{_d^s,pm} \\ v_q^s &= Ri_q^s + L\frac{di_q^s}{dt} + j\omega_r\psi_{_q^s,pm} \end{aligned} \tag{1.2}$$

For the IPMSM the stator voltage equation showing the two components is given by:

$$\begin{vmatrix} v_d^s \\ v_q^s \end{vmatrix} = R\begin{vmatrix} i_d^s \\ i_q^s \end{vmatrix} + \frac{d}{dt}\cdot\begin{vmatrix} \Sigma L + \Delta L\cos(2\vartheta_r) & \Delta L\sin(2\vartheta_r) \\ \Delta L\sin(2\vartheta_r) & \Sigma L - \Delta L\cos(2\vartheta_r) \end{vmatrix}\begin{vmatrix} i_d^s \\ i_q^s \end{vmatrix} + j\omega_r\Psi_{pm}\begin{vmatrix} \cos(\vartheta_r) \\ \sin(\vartheta_r) \end{vmatrix} \tag{1.3}$$

where ΣL and ΔL are respectively the average inductance and the differential inductance which are defined as follows:

$$\begin{aligned} \Delta L &= \tfrac{L_d+L_q}{2} \\ \Sigma L &= \tfrac{L_q-L_d}{2} \end{aligned} \tag{1.4}$$

To realize the control of the motor it is useful to transform these equations into a rotor synchronous reference frame. Hence, this second reference frame is rotating with the speed ω_r and it has the real axis coincident with the polar axis of the rotor, so that the spatial vector ψ_{pm}^r is composed by only the real component:

$$\psi_{pm}^r = \Psi_{pm} + j0 \tag{1.5}$$

This fact leads to a further simplification of the stator voltage equation. The axes of these reference frames are shown in figure 1.1, where the stationary reference frame is defined by $d^s - q^s$ axes while the synchronous reference frame is defined by $d^r - q^r$ axes and g stands for a generic complex variable.

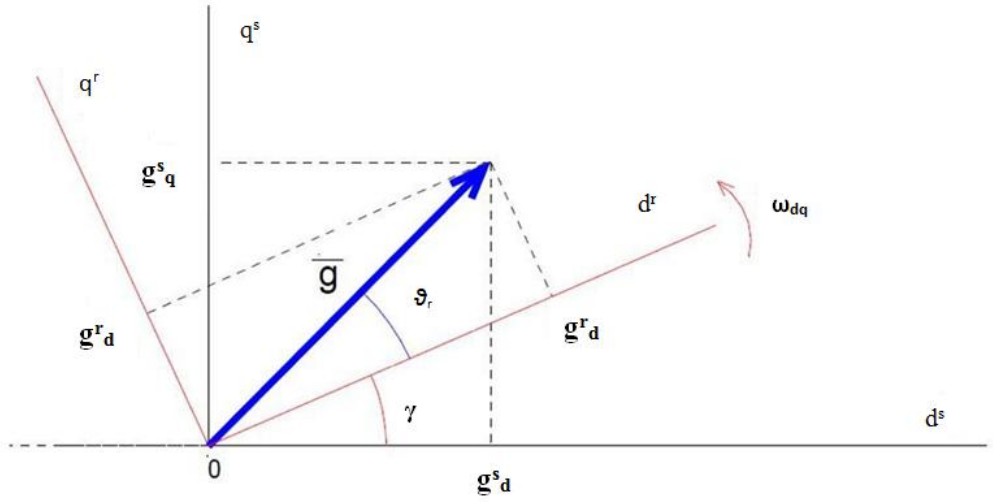

Figure 1.1: Space vector in both stationary and synchronous reference frame

With the help of figure 1.1 the mathematical relation between stationary and synchronous reference frame, and viceversa, are obtained as follow:

$$g_{dq}^{s} = |g|e^{j(\gamma+\vartheta_r)} = |g|e^{j(\gamma)}e^{j(\vartheta_r)} = g_{dq}^{r}e^{j(\vartheta_r)} \tag{1.6}$$

to pass from the stationary to the synchronous reference frame, and the inverse transformation:

$$g_{dq}^{r} = g_{dq}^{s}e^{j(-\vartheta_r)} \tag{1.7}$$

to pass from synchronous to the stationary reference frame. The transforming matrices are given by:

$$\begin{aligned} g_{dq}^{s} &= \begin{vmatrix} \cos(\vartheta_r) & \sin(\vartheta_r) \\ -\sin(\vartheta_r) & \cos(\vartheta_r) \end{vmatrix} g_{dq}^{r} \\ g_{dq}^{r} &= \begin{vmatrix} \cos(\vartheta_r) & -\sin(\vartheta_r) \\ \sin(\vartheta_r) & \cos(\vartheta_r) \end{vmatrix} g_{dq}^{s} \end{aligned} \tag{1.8}$$

It is now possible to write the stator voltage equations of both SPMSM and IPMSM in the synchronous reference frame separating the real and the imaginary part as follow:

$$\begin{aligned} v_d^r &= Ri_d^r + L\tfrac{di_d^r}{dt} - \omega_r L i_d^r \\ v_q^r &= Ri_q^r + L\tfrac{di_q^r}{dt} + \omega_r L i_d^r + \omega_r \Psi_{pm} \end{aligned} \tag{1.9}$$

for the SPMSM and

$$\begin{aligned} v_d^r &= Ri_d^r + L_d\frac{di_d^r}{dt} - \omega_r L_q i_q^r \\ v_q^r &= Ri_q^r + L_q\frac{di_q^r}{dt} + \omega_r L_d i_d^r + \omega_r \Psi_{pm} \end{aligned} \tag{1.10}$$

for the IPMSM.
It is also useful to have a global view of all the dimensions using a vector chart. As an example, figure 1.2 shows the graphical representation of 1.9.

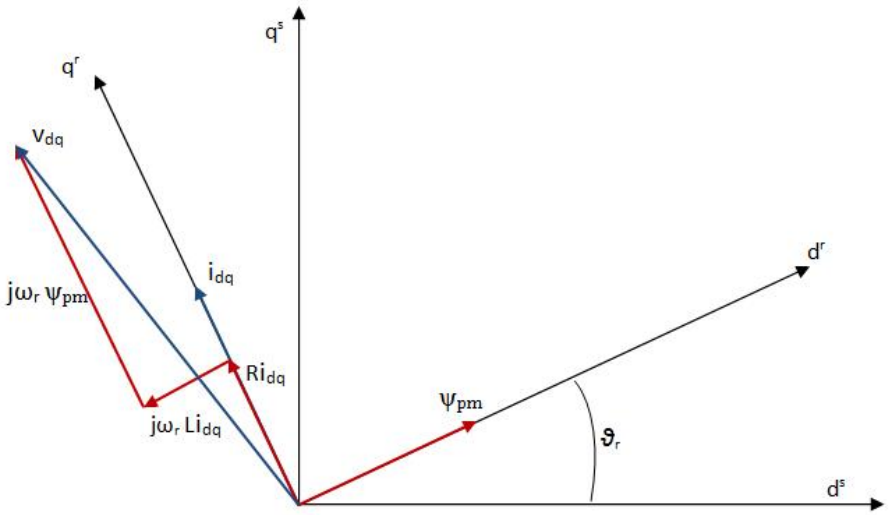

Figure 1.2: Vector chart of the voltage equation of an SPMSM

1.3. Model Based Method Sensorless Techniques (MBSTs)

As it has been said in the introduction two type of sensorless techniques can be found depending on the operating speed: MBST suitable for medium to high speed and HFIST for low and zero speed.
Now that a panoramic view of the voltage equations of the machine has been presented, it is possible to introduce the first group of sensorless techniques that is considered in this thesis.
MBSTs obtain the the angular speed and the position of the polar axis of the rotor from the back-EMF induced in the stator windings, using the fundamental model of the machine. To get this information the stator currents and voltages are needed. The stator currents can be easily measured, while the stator voltages are not normally measured but can be estimated from the voltage commands to the inverter.
Three different MBSTs will be considered: open-loop estimators, close loop Model Reference Adaptive Systems (MRASs) and closed-loop observers.

1.3.1. Estimators (open-loop)

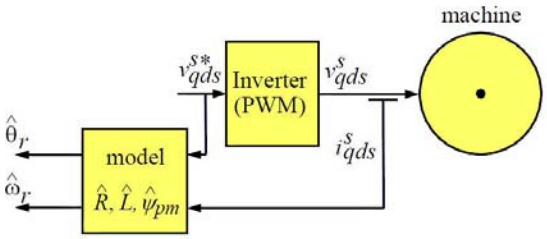

Figure 1.3: General structure of an estimator (open loop) [12]

Figure 1.3 schematically shows how an estimator is implemented.It uses a model of the motor that contains the rotor position together with the measured stator current and voltage and to solve it getting, at the end, the rotor position as a function of measured quantities. As regard the SPMSMs, an example of that kind of model is the equation 1.1 that can be rewritten in this manner:

$$v^s_{dq} = Ri^s_{dq} + \frac{d\psi^s_{dq}}{dt} = Ri^s_{dq} + \frac{(Li^s + \psi^s_{pm})}{dt} = Ri^s_{dq} + \frac{di^s_{dq}}{dt} + \frac{d\psi^s_{pm}}{dt} \tag{1.11}$$

from this equation is possible to obtain:

$$\frac{d\psi^s_{pm}}{dt} = v^s_{dq} - Ri^s_{dq} - \frac{di^s_{dq}}{dt} \tag{1.12}$$

and by integrating it:

$$\psi^s_{pm} = \Psi_{pm} e^{j\vartheta_r} = \int_{-\infty}^{t} (v^s_{dq} - Ri^s_{dq})\, dt - Li^s_{dq} = \psi^s_{pm}(0) + \int_{0}^{t} (v^s_{dq} - Ri^s_{dq})\, dt - Li^s_{dq} \tag{1.13}$$

From the last equation it is clear that the results of the integration provides the space vector of the magnetic flux due to the permanent magnets ψ^s_{pm} linked by the stator windings. The position of this gives the exact position of the rotor which is the wanted information. Equation 1.13 is schematically represented with the block diagram in figure 1.4.

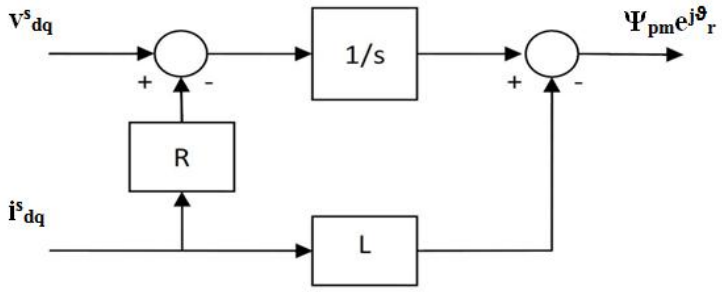

Figure 1.4: Block diagram of the selected open loop estimator [15]

For the IPMSMs a suitable model is given by equation 1.3 that can be also written as follow:

$$\begin{vmatrix} v_d^s \\ v_q^s \end{vmatrix} = R \begin{vmatrix} i_d^s \\ i_q^s \end{vmatrix} + \frac{d}{dt} \cdot \Sigma L \begin{vmatrix} i_d^s \\ i_q^s \end{vmatrix} + \frac{d}{dt} \cdot \Delta L \begin{vmatrix} \cos(2\vartheta_r) & \sin(2\vartheta_r) \\ \sin(2\vartheta_r) & -\cos(2\vartheta_r) \end{vmatrix} \begin{vmatrix} i_d^s \\ i_q^s \end{vmatrix} + j\omega_r \Psi_{mg} \begin{vmatrix} \cos(\vartheta_r) \\ \sin(\vartheta_r) \end{vmatrix} \tag{1.14}$$

It is clear from equation 1.14 that, while in a SPMSM there is only one term function of the rotor position, in a IPMSM both the inductance matrix and the back-EMF depend on the rotor position. For this reason the voltage equation 1.14 of an IPMSM has to be mathematically elaborated. This process can be carried out in two manner, depending on the implementation, providing an equation with only one term function of the rotor position. The result of this process is shown in the following equations.

- First implementation [4]:

$$\begin{vmatrix} v_d^s \\ v_q^s \end{vmatrix} = \begin{vmatrix} R & -2\omega_r \Delta L \\ 2\omega_r \Delta L & R \end{vmatrix} \begin{vmatrix} i_d^s \\ i_q^s \end{vmatrix} + \frac{d}{dt} \cdot \begin{vmatrix} L_d & 0 \\ 0 & L_d \end{vmatrix} \begin{vmatrix} i_d^s \\ i_q^s \end{vmatrix} + \begin{vmatrix} e_d^s \\ e_q^s \end{vmatrix} \tag{1.15}$$

  In the right term of equation 1.15 a new term appears: this term is called extended back-EMF e_{dq}^s and it is given by:

$$\begin{vmatrix} e_d^s \\ e_q^s \end{vmatrix} = (\omega_r[(L_d - L_q)i_d^r + \psi_{mg}^s] - (L_d - L_q)\frac{d}{dt} \cdot i_d^r) \begin{vmatrix} -\sin(\vartheta_r) \\ \cos(\vartheta_r) \end{vmatrix} \tag{1.16}$$

- Second implementation [1]:

$$\begin{vmatrix} v_d^s \\ v_q^s \end{vmatrix} = \begin{vmatrix} R & 0 \\ 0 & R \end{vmatrix} \begin{vmatrix} i_d^s \\ i_q^s \end{vmatrix} + \frac{d}{dt} \cdot \begin{vmatrix} L_q & 0 \\ 0 & L_q \end{vmatrix} \begin{vmatrix} i_d^s \\ i_q^s \end{vmatrix} + \begin{vmatrix} e_d^s \\ e_q^s \end{vmatrix} \tag{1.17}$$

where the extended back-EMF e^s_{dq} in equation 1.17 is given by equation 1.18.

$$\begin{vmatrix} e^s_d \\ e^s_q \end{vmatrix} = \frac{d}{dt} \cdot \psi_{ext} \begin{vmatrix} \cos(\vartheta_r) \\ \sin(\vartheta_r) \end{vmatrix} \tag{1.18}$$

with $\psi_{ext} = \psi_{mg} + (L_d - L_q) i^r_d$.

The extended back-EMF concept is therefore useful as it eliminates the dependence of the inductance matrix form the rotor position.

1.3.2. Model Reference Adaptive Systems (closed-loop)

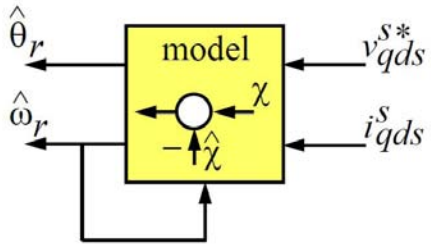

Figure 1.5: General structure of an adaptive model [12]

A simple scheme that shows how Adaptive Models work is presented in figure 1.5. As it can be seen from figure 1.5 the main difference with the previous approach is the feedback of a certain dimension in order to improve the dynamic of the whole system.
In this method, the same variable x is obtained, from direct measurement at the machine, using two different mathematical models: the result of one $\tilde{x}$ independent from the rotor position while the result of the other $\tilde{x^{\vartheta}}$ dependent on that variable. The former will be called reference model while the latter adaptive model. The difference between the output of the two models indicates that the rotor position estimation is not correct. An adaption mechanism is then needed to correct the position estimation. Only when the results obtained with the two models are equal, the estimated position coincides with the real one.
For the SPMSMs, the space vector of the flux due to the permanent magnet ψ^s_{pm} can be used as estimated variable $\tilde{x}$, which is obtained from the stator voltage and current. So the reference model can be described by the equation 1.13 that does not need the rotor position information. Whereas the adaptive model that has to contain the rotor position information can be written as:

$$\psi^{s(\vartheta)}_{pm} = \Psi_{pm} e^{j\vartheta_r} \tag{1.19}$$

In this case it does not require any measurement from the machine. The estimator MRAS for this specific case is shown in figure 1.6.

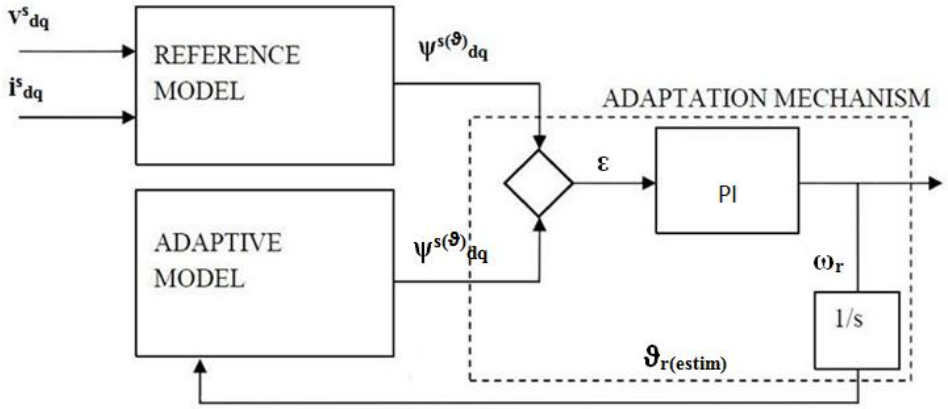

Figure 1.6: Block diagram of an MRAS estimator for an SPMSM [15]

In conclusion the target of the MRAS estimator is to produce an estimated position $\vartheta_{r(estim)}$ that has to "run after" the ϑ_r which is given by the flux of the permanent magnet obtained with the reference model. The phase lag between the space vector of the flux obtained ψ^s_{pm} with the reference model and the one $\psi^{s(\vartheta)}_{pm}$ obtained with the adaptive model is used as estimation error ϵ. This can be written in the following way:

$$\begin{aligned}\epsilon &= Im(\psi^s_{pm}\hat{\psi}^{s(\vartheta)}_{pm}) = |\psi_{pm}||\hat{\psi}^{(\vartheta)}_{pm}|\sin(\vartheta_r - \vartheta_{r(estim)}) \\ &= \psi^s_{pm,q}\psi^{s(\vartheta)}_{pm,d} - \psi^s_{pm,d}\psi^{s(\vartheta)}_{pm,q}\end{aligned} \tag{1.20}$$

where the $\wedge$ stands for complex conjugate. If the argument of the *sin* (and so the phase lag between the two estimated flux vectors) is small it is possible to write:

$$\sin(\vartheta_r) \approx \vartheta_r \tag{1.21}$$

and so the adaptation mechanism can be designed as in figure 1.7, where it is assumed that the magnitude of both the reference and the adaptive model is Ψ_{pm}.

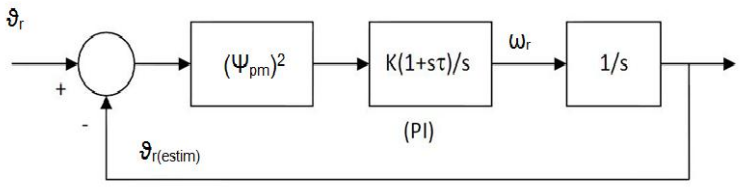

Figure 1.7: Loop of the adaptive system [15]

The method described for a SPMSM, can be modified to be applied to IPMSM. Considering first the stator voltage equation in the synchronous reference frame, this is given by equation 1.10 and can be rewritten:

$$v_{dq}^{r} = Ri_{dq}^{r} + \frac{d\psi_{dq}^{r}}{dt} + j\omega_r \psi_{pm}^{r} \tag{1.22}$$

with

$$\psi_{dq}^{r} = |L|i_{dq}^{r} + \psi_{pm}^{r} \tag{1.23}$$

and the product $|L|i_{dq}^{r}$ is a complex number given by the matrix product:

$$|L|i_{dq}^{r} = \begin{vmatrix} L_d & 0 \\ 0 & L_q \end{vmatrix} \begin{vmatrix} i_d^r \\ i_q^r \end{vmatrix} = L_d i_d^r + L_q i_q^r \tag{1.24}$$

From these equations it is possible to obtain the space vector of the flux produced by the permanent magnet, which is given by:

$$\psi_{pm}^{r} = \Psi_{pm} e^{j\vartheta_r} = \int_{-\infty}^{t} (v_{dq}^{r} - Ri_{dq}^{r} - j\omega_r \psi_{dq}^{r})\, dt - |L|i_{dq}^{r} \tag{1.25}$$

which in figure 1.8 is represented as block scheme.

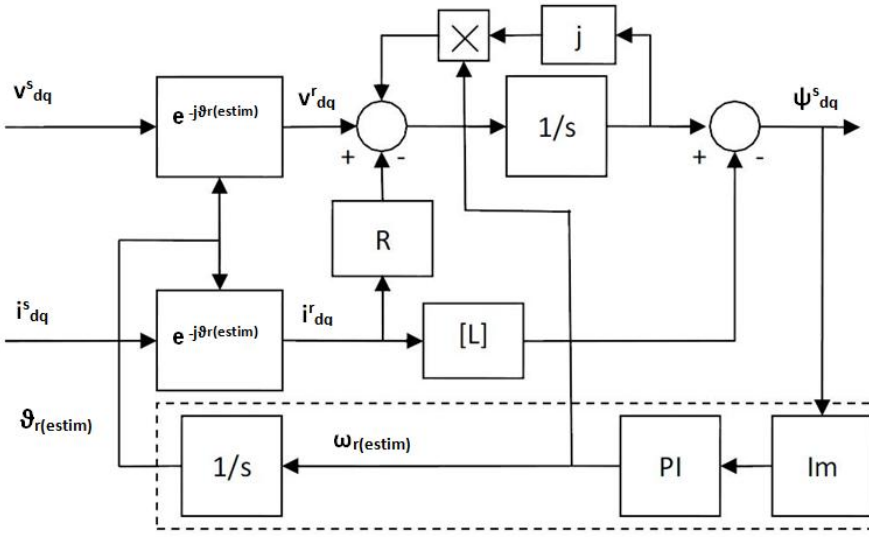

Figure 1.8: Block diagram of an MRAS estimator for an IPMSM [15]

As it is shown in figure 1.8 for this configuration the stator current and voltage have to be measured and then transformed in the reference frame synchronous with the rotor using the estimated position $\vartheta_{r(estim)}$. By definition, in the reference frame considered, the space vector of the flux produced by the permanent magnet

should have an imaginary component equal to zero according to equation 1.5. So the presence of an imaginary component different form zero means that the rotor position estimation is not correct. For this reason the imaginary part of the space vector of the flux is used as estimation error ϵ which can be the input of an adaptation mechanism similar to the one used for SPMSM in figure 1.7.

1.3.3. Observer (closed-loop) [18]

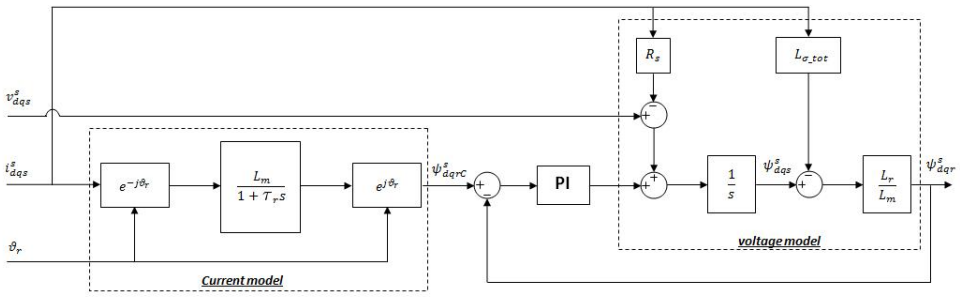

Figure 1.9: Block diagram of a closed-loop flux observer

The example of observer presented in this section can be only applied to IM while does not make sense for PMSM. In the block diagram of figure 1.9 two models providing the same quantity can be distinguished: the current model (utilizing the measured stator speed) and the voltage model (utilizing the measured stator voltage and current). The estimated quantity is the rotor flux from which the speed and the angle necessary for the IM control can be then estimated by means of a PLL.
The two models forming the closed-loop observer are both open-loop rotor flux observer connected by a PI regulator which guarantees a smooth transition between them. In particular, when the fundamental frequency is below the PI bandwidth, the latter forces the voltage model output to follow the current model output which behaves as reference. While, if the fundamental frequency exceeds the PI bandwidth, the overall output is directly the output of the voltage model as the current model stops acting as a reference.

The practical implementation of these solutions presents some problems, including:

- Parametric dependence: the estimator needs to know the parameters R and L with a great precision. But it is known that they depend on the operating condition (for example the resistance changes with temperature). Furthermore, the measurement of the stator current can be affected by errors.

- Computational difficulties: this results from the fact that we are making use of pure integrators. This is not possible in the practice due to two reason: first, it is necessary to know of the initial conditions of the integrators otherwise the output presents a constant error (offset). Second, small offsets at the input of the integrators will produce a drift of the output. To solve these two problems, the integrator can be replaced by a low pass filter with the cut off frequency smaller than the lower operation speed.

1.4. High Frequency Injection Sensorless Techniques (HFISTs)

The estimation methods that have been reported so far make use of the fundamental equations of the machine, in particular of the stator voltage, and they obtain in different manner the rotor position from the back-EMF induced by the variation of the flux produced by the permanent magnets. Therefore, as it is evident analyzing the back-EMF equation, these method cannot operate at low and zero speed, since the value of the key variable which is needed for the estimation is proportional to the operative speed and so below a certain minimum speed we cannot relay on them.
To overcome this limitation, sensorless control methods based on tracking the position of the saliences (asymmetries) in electric machines have been proposed. Such methods have the capability of providing accurate, high bandwidth, position, speed, disturbance torque estimates, and/or flux estimates in the low-speed range, including zero speed and frequency. These techniques measure the response of the machine when high frequency excitation, distinct from the fundamental excitation used for torque production, is applied via the inverter.
The pros of these methods compared to MBST include the reduction of the parameter sensitivity, and the fact that they can work at very low and zero speed. On the other hand, to efficiently implement these method, the design of the machine have to be very precise and sometimes additional sensors are required and for this reason the cost of the drive could increase. Furthermore the injection of high frequency signals or the modification of the PWM pattern can results in unwanted effects such as vibration, noise and additional loses.
In this section only a panoramic review of HFIM is given, the details will be discussed in a further section.

The superficial and interior permanent magnet synchronous machines are treated in two different sections and in particular the IPMSM is analyzed first as it is the natural candidate for the HFISTs. In fact while a IPMSM presents a natural salience, a SPMSM exploits the saturation induced in the stator teeth.

1.4.1. Internal Permanent Magnet Synchronous Machine (IPMSM)

The high-frequency model of the machine can be derived from the corresponding fundamental frequency models, the discussion following being valid both for induction and permanent magnet synchronous machines (PMSMs).If a high frequency excitation is injected into the stator windings, the resistive terms can be neglected compared to the inductive terms. In addition, the fact that the high-frequency signal is spectrally separated from the fundamental excitation frequency allows the back-EMF to be eliminated. With these two assumptions, the high-frequency model can be considered as a pure inductive load, with the phase inductance magnitudes being a function of rotor position. Furthermore, at low operating speeds the high-frequency excitation signals occur at frequencies significantly larger than the fundamental frequency, and so, assuming that the position dependent inductances are composed by a single harmonic, the time rate of change of the inductances is small and can be safely ignored. With these assumptions, the high-frequency model is given by:

$$\begin{aligned} v_a - v_n = v_{an} &= (\Sigma L_{\sigma s} + 2\Delta L_{\sigma s}\cos(h_r(\vartheta_r)) \cdot \tfrac{di_a}{dt} \\ v_b - v_n = v_{bn} &= (\Sigma L_{\sigma s} + 2\Delta L_{\sigma s}\cos(h_r(\vartheta_r - \tfrac{2\pi}{3})) \cdot \tfrac{di_b}{dt} \\ v_c - v_n = v_{cn} &= (\Sigma L_{\sigma s} + 2\Delta L_{\sigma s}\cos(h_r(\vartheta_r - \tfrac{4\pi}{3})) \cdot \tfrac{di_c}{dt} \end{aligned} \tag{1.26}$$

where v_a, v_b, and v_c are the voltages applied by the inverter to the machines terminals relative to the negative rail of the dc bus, v_n is the voltage induced in the neutral point of the stator windings and it is given by:

$$v_n = -\frac{v_a L_{\sigma b} L_{\sigma c} + v_b L_{\sigma a} L_{\sigma c} + v_c L_{\sigma a} L_{\sigma b}}{L_{\sigma b} L_{\sigma c} + L_{\sigma a} L_{\sigma c} + L_{\sigma a} L_{\sigma b}} \tag{1.27}$$

$\Sigma L_{\sigma s}$ and $\Delta L_{\sigma s}$ are the average and differential stator high-frequency inductances, $L_{\sigma a}$, $L_{\sigma b}$, and $L_{\sigma c}$ the inductance terms within brackets in equation 1.26, h_r is the harmonic order of the salience relative to electrical angular units, and ϑ_r is the angular position of the rotor in electrical radians. It is then useful to write equation 1.26 in matrix form, getting equation 1.28.

$$\begin{vmatrix} v_a \\ v_b \\ v_c \\ 0 \end{vmatrix} = \begin{vmatrix} L_{\sigma a} & 0 & 0 & 1 \\ 0 & L_{\sigma b} & 0 & 1 \\ 0 & 0 & L_{\sigma c} & 1 \\ 1 & 1 & 1 & 0 \end{vmatrix} \cdot \begin{vmatrix} \frac{di_a}{dt} \\ \frac{di_b}{dt} \\ \frac{di_c}{dt} \\ 0 \end{vmatrix} \tag{1.28}$$

and finally the transformation to the stationary reference frame $d^s - q^s$ lead to the following equations:

$$\begin{vmatrix} v_q^s \\ v_d^s \\ v_0^s \end{vmatrix} = L_{\sigma qd0}^s \frac{d}{dt} \cdot \begin{vmatrix} i_q^s \\ i_d^s \\ v_0^s \end{vmatrix} \tag{1.29}$$

where $L_{\sigma qd0}^s$ is given by:

$$L_{\sigma qd0}^s = \Sigma L_{\sigma s} \begin{vmatrix} 1 & 0 & 0 \\ 0 & 1 & 0 \\ 0 & 0 & 1 \end{vmatrix} + \Delta L_{\sigma s} \begin{vmatrix} \cos(h_r\vartheta_r) & -\sin(h_r\vartheta_r) & 2\cos(h_r\vartheta_r) \\ -\sin(h_r\vartheta_r) & -\cos(h_r\vartheta_r) & 2\sin(h_r\vartheta_r) \\ \cos(h_r\vartheta_r) & \sin(h_r\vartheta_r) & 0 \end{vmatrix} \tag{1.30}$$

It is now possible to get the phase-to-neutral voltages which is defined as the mean value of the phase-to neutral voltages. Its expression is given by the following equation:

$$v_{\sigma n} = \frac{v_{an} + v_{bn} + v_{cn}}{3} = \frac{v_a + v_b + v_c}{3} - v_n \tag{1.31}$$

The main high-frequency sensorless control methods can be divided depending on the type of high-frequency signal excitation and the signals which are measured. In particular, considering the type of excitation, it can be continuous, discontinuous, periodic and PWM and depending on the choice done, different techniques can be applied. If continuous excitation is used, a high-frequency signal is always present and superimposed to the fundamental excitation. On the contrary a discontinuous excitation injects the high-frequency signal periodically and so the result is that it does not provide a continuous rotor position estimation.
On the other hand the excitation is considered periodic when it injects a periodic high-frequency carrier signal (usually in the range of several hundred hertz up to a few kilohertz) superimposed on the fundamental excitation while a PWM excitation uses modified forms of PWM, and it measures the response to particular states of the inverter to track the rotor position.
The signal measured also contribute to distinguish various methods. In particular the signal measured can be the phase current figure 1.10a, the phase current derivative figure 1.10b, the zero-sequence voltage figure 1.10c and d and the zero-sequence current/zero-sequence current derivative for delta-connected machine figure 1.10e.

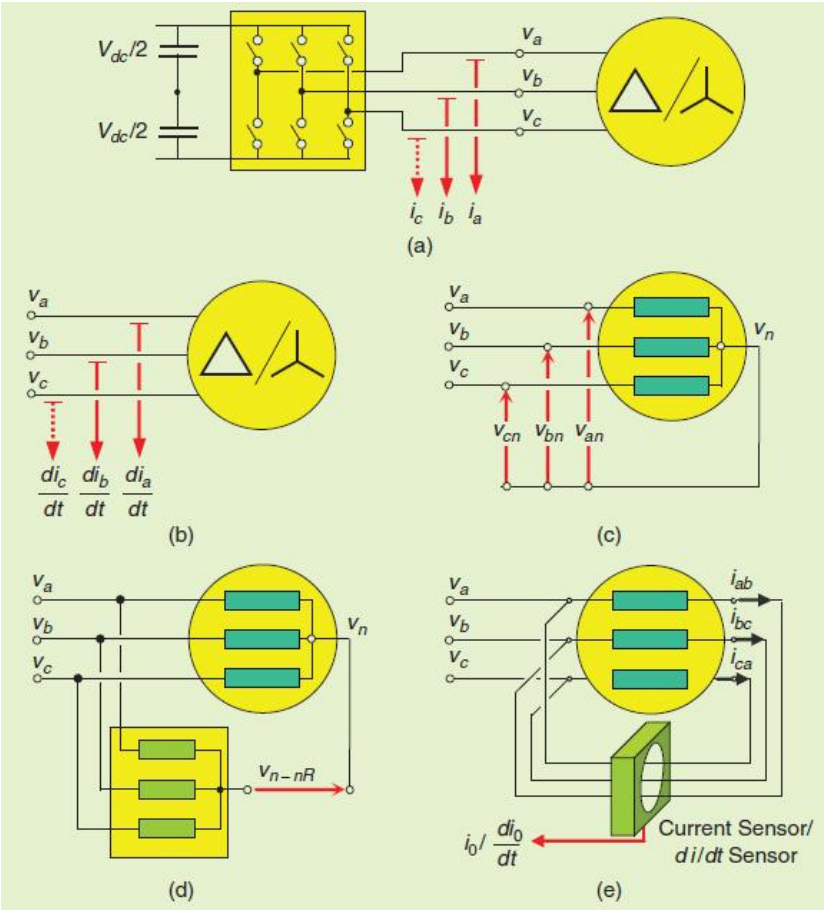

Figure 1.10: Signal measurement: (a) phase currents using two/three sensors, (b) phase currents derivative using two/three sensors, (c) and (d) zero-sequence voltage using three voltage sensors/a single sensor and an auxiliary resistor network (wye-connected machine), and (e) zero-sequence current/zero-sequence current derivative (delta-connected machine) [13]

It is also interesting to note that most of industrial drives include phase current sensors and often a dc bus-voltage sensor. Sensorless methods that rely on only these signals could be considered as no cost from a hardware perspective. Opposite to this are the methods that require additional signals and associated hardware cost, e.g., sensors, cabling, A/D channels, and signal-conditioning circuits. In the end, these methods replace a position/speed sensor by a different type of sensor, which obviously limits the intended benefits of sensorless control. It will be considered first the different kind of signal excitation, focusing the attention on the continuous excitation-based methods, since the differences with the discontinuous one do not affect the physical aspects but only the implementation strategies.

Rotating Carrier-Signal Voltage:

This strategy consist on superimposing a high-frequency rotating carrier-signal voltage to the fundamental voltage applied by the inverter to the machine terminals. Equation 1.32 gives the signal in form of spatial vector.

$$v^s_{qd} = v^s_d + jv^s_q = V_c e^{j\omega_c} \tag{1.32}$$

This signal interacts with the salience present in the stator transient inductance to produce two types of signals that can be used for rotor position estimation: the negative-sequence current and the zero-sequence voltage.
As far as the negative-sequence current is concerned, the rotating carrier-signal voltage applied to the machine create a carrier-signal current which can be modeled using 1.26. Analyzing the spectrum of this current it is possible to see that it is composed of two components (analytically represented in equation 1.33 and shown in figure 1.11), respectively the negative-sequence and the positive-sequence current.

$$i^s_{qd_c} = -jI_{cp}e^{j\omega_c} - jI_{cn}e^{-j\omega_c + h_r\omega_r} \tag{1.33}$$

The magnitude of the two components is given by the equation 1.34.

$$\begin{aligned} I_{cp} &= \frac{Vc}{\omega_c} \cdot \frac{\Sigma L_{\sigma s}}{\Sigma L_{\sigma s} - \Delta L_{\sigma s}} \\ I_{np} &= \frac{Vc}{\omega_c} \cdot \frac{\Delta L_{\sigma s}}{\Sigma L_{\sigma s} - \Delta L_{\sigma s}} \end{aligned} \tag{1.34}$$

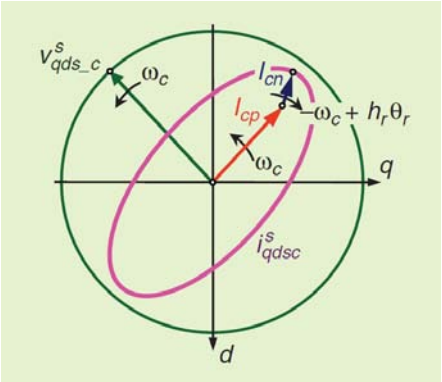

Figure 1.11: Complex vector representation of the carrier voltage and the resulting carrier current shown in the stationary reference frame [13]

But, as equation 1.33 shows, only the negative-sequence current given by equation 1.35 and represented in figure 1.12 provides the wanted information that is the rotor position.

$$i^{cn}_{qd_cn} = -jI_{cn}e^{jh_r\omega_r} \tag{1.35}$$

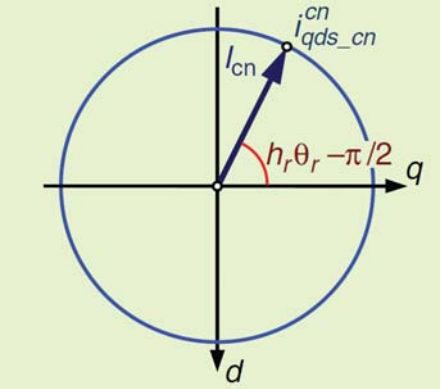

Figure 1.12: Negative-sequence carrier-signal current. Superscript "cn" stands for carrier negative reference frame [13]

Implementation of this method requires the measurement of two out of three phase currents (see figure 1.10a).

In regard the zero-sequence voltage, it can be also modeled by using the high-frequency model of the machine 1.26. Equation 1.36 shows the resulted zero-sequence voltage where it can be seen that the rotor position is again contained in the phase of this signal.

$$v^s_{0c} = \frac{v_{an} + v_{bn} + v_{cn}}{3} \approx V_{0ch}\cos(\omega_c t + h_r\vartheta_r) \tag{1.36}$$

Implementation of this method requires measurement of the three phase-to-neutral voltages, see figure 1.10c, or the method shown in figure 1.10d using a single-voltage sensor.

Amplitude-Modulated Carrier-Signal Voltage:

This method consists on injecting a amplitude-modulated carrier-signal voltage using the inverter feeding the machine. The injected voltage, assuming that the injection angle coincides with the estimated angle, is given in the synchronous reference frame by equation 1.37.

$$v^r_{qd_c} = v^r_{q_c} + jv^r_{d_c} = V_c\cos(\omega_c t + h_r\vartheta_r) \tag{1.37}$$

and the resulting current can still be modeled by 1.26 to get equation 1.38.

$$i^r_{qd_c} = \frac{1}{2}(I_{cp} + I_{cn}e^{j2\vartheta})\sin(\omega_c t) \tag{1.38}$$

where $\vartheta_{err} = \vartheta - \tilde{\vartheta}$.
The process to obtain the rotor position is quite similar to the one used for the negative-sequence current: once the fundamental current has been eliminated

and 1.38 is obtained, its imaginary component 1.40 can then be demodulated and low-pass filtering with equation 1.41 being the output.

$$i_{q_c}^r = \frac{1}{2} I_{cn} \sin(\vartheta_{err}) \sin(\omega_c t) \approx \frac{1}{2} I_{cn} \vartheta_{err} \sin(\omega_c t) \tag{1.39}$$

$$I_{err} = \frac{1}{4} I_{cn} \sin(\vartheta_{err}) \approx \frac{1}{4} I_{cn} \vartheta_{err} \tag{1.40}$$

PWM-Based Methods:

Another way to get the salience position is to use the voltage variations produced by the switching of the inverter during PWM operation. Figure 1.13 shows the six switching state vectors. Two types of signals have been proposed for use in wye-connected machines: the derivative of the current and the zero-sequence voltage induced in the stator windings.

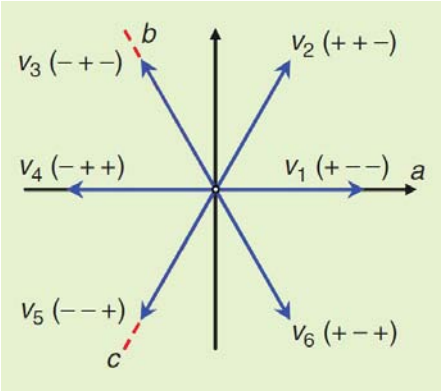

Figure 1.13: Switching state vectors (the sign of the phase potentials is indicated in brackets) [13]

Considering first the technique that makes use of the derivatives of the phase currents, it can be seen from 1.26 that they are a function of the instantaneous voltages and of the equivalent high-frequency inductances. Consequently it is possible to calculate the derivative of the currents when a new inverter state is applied by replacing v_a, v_b, and v_c in 1.26 with the corresponding voltages applied by the inverter.
In the literature, and in particular in [17], a complex vector quantity ρ_{dq}, see equation 1.41 was defined where the terms ρ_a, ρ_b, and ρ_c are calculated from the derivative of the phase currents for different states of the inverter.

$$\rho_{qd} = \frac{2}{3}(\rho_a + \rho_b e^{j2\pi/3} + \rho_b e^{j4\pi/3}) \tag{1.41}$$

Implementation of this method requires the use of di/dt sensors in figure 1.10e.

Finally, as far as zero-sequence voltage is concerned, it can be obtained, after applying a particular inverter state, from equation 1.27 by substituting v_a, v_b, and v_c by the corresponding voltage levels applied by the inverter. Based on this, three different zero-sequence voltage vectors can be defined each obtained by applying inverter states in the a, b, and c directions (see Figure 1.13) of the complex plane. A complex voltage vector, $v_{qd\sigma}$ (equation 1.42) is defined using the three measurements, which can be written in the form of equation 1.43. As can be observed from equation 1.43 this complex vector contains the information of the salience position in its phase. Implementation of this method requires measurement of three phase to neutral voltages (see figure 1.10c).

$$v_{qd\sigma} = \frac{2}{3}(v_{a\sigma} + v_{b\sigma}e^{j2\pi/3} + v_{c\sigma}e^{j4\pi/3}) \tag{1.42}$$

$$v_{qd\sigma} = -\frac{3\Delta L_{\sigma s}\Sigma L_{\sigma s}}{L_{\sigma b}L_{\sigma c} + L_{\sigma a}L_{\sigma c} + L_{\sigma a}L_{\sigma b}} \cdot e^{jh_r\vartheta_r} \tag{1.43}$$

Delta-Connected Machines:

All the considerations and analysis that have been done so far can be also considered valid for a delta-connected machine. However, in delta-connected machines, no zero-sequence voltage can be induced in the stator windings. In this case, the zero-sequence current replaces the zero-sequence voltage [see figure 1.10(e)].

1.4.2. Superficial Permanent Magnet Synchronous Machine (SPMSM)

Despite natural candidates for these method are naturally salience machines and so IPMSMs, HFIM can be also effectively applied to SPMSMs exploiting the saturation-induced salience produced by the stator flux. In fact, the iron saturation, mainly in the stator teeth, creates a modulation in machines' inductance. In contrast with inherently salient machines, like the interior PM machines, the salience in the surface mount machines does not correspond exactly with the rotor position. Although the salience position is dominated by the rotor position due to the high magnetic flux density imposed by the rotor magnets and the low stator inductances, a shift occurs in the salience position under load due to the relative shifts in the stator flux. For this reason a phase correction to account for the shift of the saturation salience due to the stator current. An example of this correction is given by figure 1.14.

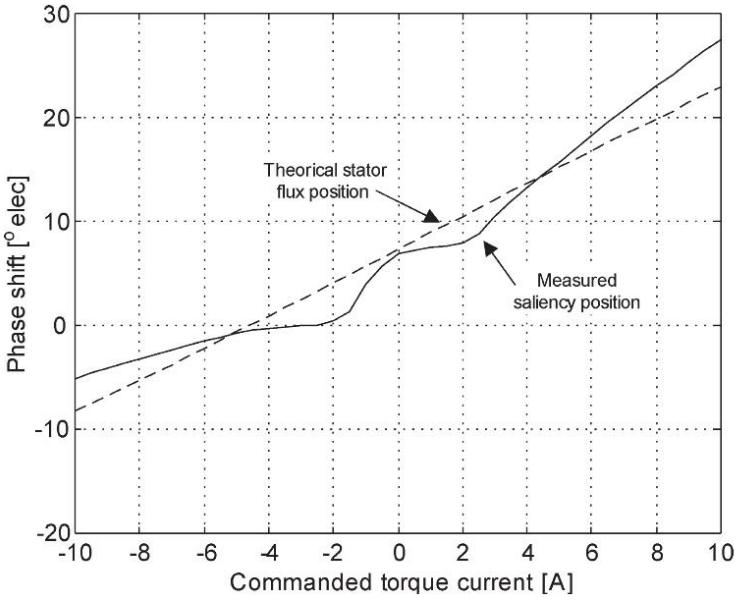

Figure 1.14: Phase shift between rotor and estimated salience position as a function of torque current [2]

Another method used to create a salience in a nonsalient machine under specific condition has been developed by researchers of the University of Padua. This method consist in a particular design of the SPMSM that install around each pole of the machine a short circuit ring as it is shown in figure 1.15 (and for this reason the method is called "ringed pole").

Figure 1.15: SPM rotor with ringed-poles [9]

The ring location is selected so that it interferes only with the d-axis of the machine which is very important as the MTPA algorithm control for an SPMSM set the d-axis current to zero and modify only the q-axis one to produce torque. So from the point of view of the machine control nothing change. But the interesting aspect is that this ring produces a frequency dependent impedance in the d-axis. In conclusion the q-axis d-axis impedance ratio increase with the frequency producing an anisotropy in the SPMSM from the point of view of HFI signals.

1.5. Hybrid Techniques

The HFIST is effective for position and speed estimation in ultra-low speed region including zero stator frequency. However, due to torque ripple and acoustic noise, the method has shortcoming in the practical use in industrial applications. On the contrary, the back-emf based method is able to estimate position and speed without acoustic noise due to additional torque ripple, but the decreasing signal-to-noise ratio and the increasing effect of the parameter-estimation errors and inverter nonlinearities in the model at low speed impede its use in the whole speed range. To perform a smooth transition between both strategies, a hybrid system is needed.
In the following it will be reported six possible hybrid system strategies which cover the overall state of the art

1.5.1. Hybrid Method Employing Speed-Dependent Functions [2]

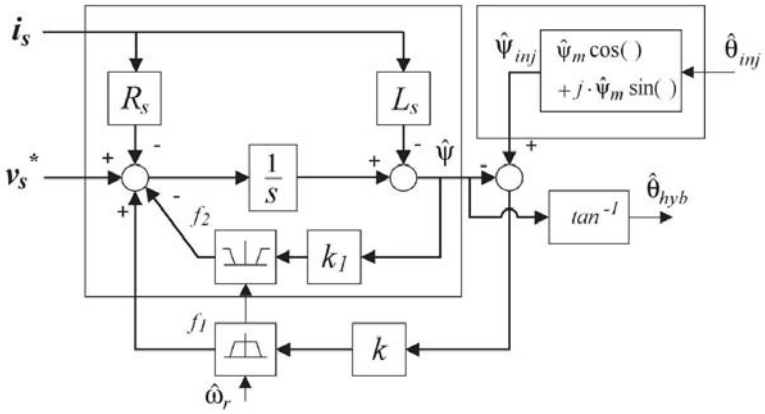

Figure 1.16: Hybrid structure for coupling of injection and voltage-model estimates [2]

The first hybrid strategy that has been considered is showed in figure 1.16. In this scheme, the injection position estimated $\hat{\vartheta_{inj}}$ is used to construct a flux estimation $\hat{\psi_{inj}}$, which serves as a reference for the model at low frequencies. At higher speeds, this flux estimation ceases to have a significant influence and is finally disconnected via the speed-dependent functions $f_1(\hat{\omega_r})$ and $f_2(\hat{\omega_r})$.
As for the MBMST during high-speed operation, a very simple model is used to obtain the rotor position information which consist in calculating the flux induced by the rotor magnets into the stator winding. The model can be considered as voltage model and, because the motor used is SPMSM, it is given by:

$$\psi_r^v = \frac{1}{s}(v_s - i_s R_s) - L_s i_s \tag{1.44}$$

In the practical implementation of the flux observer, the commanded voltages v_s^* are used instead of the actual measured values, and a low-gain k_1 negative

feedback path is provided to avoid drifting of the pure integrator of 1.44. This gives:

$$\psi_r = \frac{1}{s+k_1}(v_s^* - i_s R_s) - \frac{s}{s+k_1} i_s L_s \approx \frac{s}{s+k_1}\psi_r^v \tag{1.45}$$

Considering low-speed operation the function f_1 and f_2 are equal to one and zero respectively, so equation 1.46 can be obtained from figure 1.16.

$$\psi_r = \frac{1}{s}[(v_s^* - i_s R_s) + k(\psi_r^{inj} - \psi_r)] \tag{1.46}$$

which reorganized yields:

$$\psi_r = \frac{s}{s+k}\psi_r^v - \frac{k}{s+k}\psi_r^{inj} \tag{1.47}$$

From this equation it can be seen that the estimated flux, from which the position information is taken by mean of the $\tan^{-1}$ function, is composed of two components: one coming from to the MBMST which consist in the voltage-model estimate and the other resulting from the injection estimate. In particular, at very low speed, as can be seen from the transfer function of that component, the injection based estimation is dominant, and any noise on it is filtered by the low-pass filter action of the close loop, while during the transient, to improve the results of using the HFIST alone, the MBMST provide a path for the estimation of the high-frequency components of the flux.
As the speed increases and the MBMST provides better estimations, the injection estimation can be gradually neglected making the voltage-model estimate assuming the leader role in the estimation of the rotor flux ψ_r. In particular, this transition starts at frequencies higher than the crossover frequency f_c. The disconnection of the injection is performed gradually, reducing the controller gain by means of a multiplying function $f_1(\hat{\omega}_r)$. This function decreases linearly above the lower transition speed, reaching zero at the upper transition speed. At the same time, the feedback gain k_1 is connected to avoid drifting of the flux estimator, multiplying the feedback by $f_2(\hat{\omega}_r)$, which is complementary to $f_1(\hat{\omega}_r)$. At speeds above the upper transition speed the functions $f_1(\hat{\omega}_r)$ and $f_2(\hat{\omega}_r)$ have the values of zero and one, respectively, reducing the hybrid system to the simple voltage model of equation 1.45.
Finally, to avoid torque ripple and acoustic noise due to the high frequency current in the motor, the voltage injection is disconnected at a speed slightly higher then the upper transition speed.

1.5.2. Hybrid Method Employing the HFIST Only as Correction of the MBST [3]

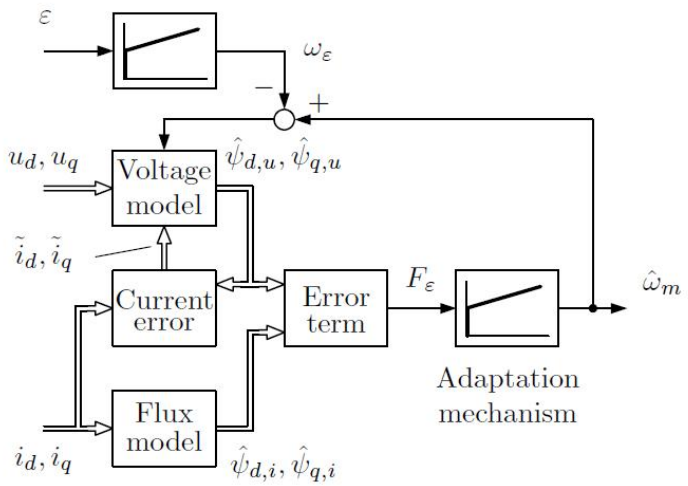

Figure 1.17: Block diagram of the combined observer: adaptive observer is augmented with error signal ϵ from HF signal injection [3]

This method makes use of the HFIST to correct the estimated rotor position by influencing the direction of the stator flux estimate provided by the MBMST. The principle on which this method relies is the use the error signal ϵ of the signal injection method to adjust the adaptive model of the MBMST. In fact, a model reference adaptive system (MRAS) is used as MBMST where the reference model is given by (estimated quantities are denoted by $\wedge$):

$$\begin{aligned} \hat{\psi_{d,i}} &= L_d i_d + \hat{\psi_{pm}} \\ \hat{\psi_{q,i}} &= L_q i_q \end{aligned} \tag{1.48}$$

which it is referred to as a flux model in the reference frame fixed to the rotor, and the adaptive model is given by the following voltage model:

$$\begin{aligned} \frac{d\hat{\psi_{d,u}}}{dt} &= u_d - R_s i_d + \hat{\omega_m}\hat{\psi_{q,u}} + \lambda\tilde{i_d} \\ \frac{d\hat{\psi_{q,u}}}{dt} &= u_q - R_s i_q - \hat{\omega_m}\hat{\psi_{d,u}} + \lambda\tilde{i_q} \end{aligned} \tag{1.49}$$

where

$$\begin{aligned} \hat{i_d} &= \frac{\hat{\psi_{d,u}} - \hat{\psi_{pm}}}{L_d} \\ \hat{i_q} &= \frac{\hat{\psi_{q,u}}}{L_q} \end{aligned} \tag{1.50}$$

are the estimates for the stator current components and

$$\begin{aligned} \tilde{i_d} &= i_d - \hat{i_d} \\ \tilde{i_q} &= i_q - \hat{i_q} \end{aligned} \tag{1.51}$$

are the components of the current error. The following error term is defined:

$$F_\epsilon = \hat{\psi_{q,i}} - \hat{\psi_{q,u}} \tag{1.52}$$

As for the HFIST, an alternating voltage injection is used and, the error signal extract after the demodulation of the current signal is given by:

$$\epsilon = \frac{u_c}{\omega_c} \cdot \frac{L_q - L_d}{4 L_q L_d} \sin(2\hat{\vartheta}_m). \tag{1.53}$$

Coming back to the analysis of the block diagram of the combined observer in figure 1.17 it can be seen that a correction ω_ϵ is subtracted from the estimated speed $\hat{\omega_m}$ and a PI mechanism is used for driving the error signal ϵ to zero. The algorithm of the adaptive system is given by equation 1.54.

$$\begin{aligned} \frac{d\hat{\psi_{d,u}}}{dt} &= u_d - R_s i_d + (\hat{\omega_m} - \omega_\epsilon)\hat{\psi_{q,u}} + \lambda \tilde{i_d} \\ \frac{d\hat{\psi_{q,u}}}{dt} &= u_q - R_s i_q - (\hat{\omega_m} - \omega_\epsilon)\hat{\psi_{d,u}} + \lambda \tilde{i_q} \end{aligned} \tag{1.54}$$

where the output of the PI mechanism ω_ϵ is given by equation 1.55.

$$\omega_\epsilon = \gamma_p \epsilon + \gamma_i \int \epsilon dt \tag{1.55}$$

where γ_p and γ_i are the gains of the PI.
At low speeds, the combined observer relies both on the signal injection method and on the adaptive observer: the signal injection method dominates in steady state whereas the adaptive observer commands at transients. When the rotor speed increases above a certain value, the estimation is based only on the adaptive observer.

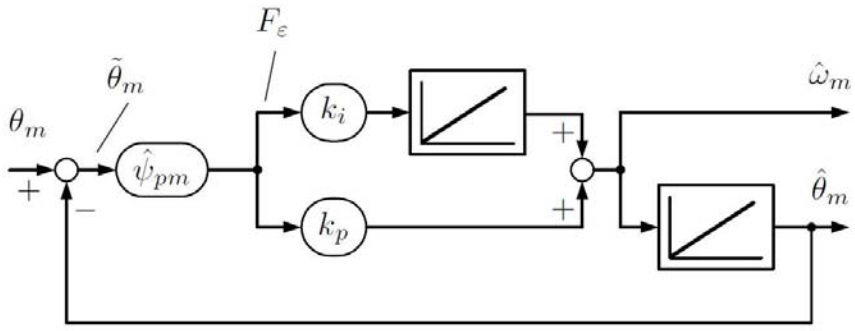

Figure 1.18: Block diagram of the phase-locked loop corresponding to the adaptive observer [3]

The selection of the gains k_p and k_i of the adaptation mechanism shown in figure 1.18 follows the law:

$$\begin{aligned} k_p &= \frac{2\alpha_{f0}}{\Psi_{mg}} \\ k_i &= \frac{\alpha_{f0}^2}{\Psi_{mg}} \end{aligned} \tag{1.56}$$

where the only design parameter α_{f0} corresponds to the approximate bandwidth of the adaptive system.
On the other hand the gains γ_p and γ_i of the PI mechanism are selected as:

$$\begin{aligned} \gamma_p &= \frac{\alpha_i}{2K_\epsilon} \\ \gamma_i &= \frac{\alpha_i^2}{6K_\epsilon} \end{aligned} \tag{1.57}$$

where α_i is the only required design parameter and it corresponds to the approximate bandwidth of the PI mechanism while K_ϵ is the signal injection gain:

$$K_\epsilon = \frac{u_c}{\omega_c} \cdot \frac{L_q - L_d}{4L_qL_d} \tag{1.58}$$

In order to obtain a smooth transition between the low-speed and high-speed regions, the amplitude of the signal injection voltage u_c and the bandwidth α_i are decreased linearly with increasing speed, and the signal injection is disabled above transition speed ω_Δ as it is shown by the following equations:

$$\begin{aligned} u_c &= f(\hat{\omega}_r)u_{c0} \\ \alpha_i &= f(\hat{\omega}_r)\alpha_{c0} \end{aligned} \tag{1.59}$$

where u_{c0} and α_{c0} are the values corresponding to zero-speed operation and the function $f(\hat{\omega}_r)$ is shown in figure 1.19.

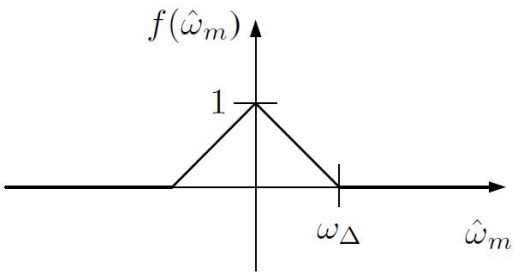

Figure 1.19: Definition of the speed-dependent function $f(\hat{\omega}_r)$ [3]

1.5.3. Hybrid Method Employing Weighting Factors [7]

This methods has some similarities with the previous one as the rotor position estimation is always provided by the MBST estimation while the result of the HFIST estimation is only used to correct the machine model of the MBST under low and zero operating speed condition.

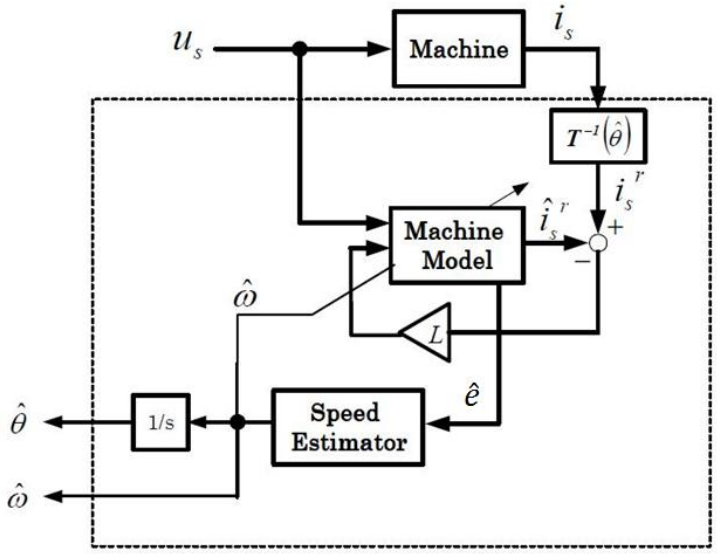

Figure 1.20: Position and speed estimator with back-EMF based method [7]

Figure 1.20 shows the block diagram of the MBST used, where the machine model is defined as follows:

$$\begin{aligned} \tfrac{d}{dt}\hat{x} &= A(\hat{\omega}\hat{x} + \nu \\ i_s^r &= \begin{vmatrix} I \\ 0 \end{vmatrix} \hat{x} \\ \nu &= Bu_s + L(i_s^r - \hat{i}_s^r) \end{aligned} \tag{1.60}$$

where

$$\hat{x} = \begin{vmatrix} i_s^r \\ \hat{e} \end{vmatrix}$$

i_s^r is the stator current in the syncrhonous reference frame, u_s is stator voltage in the stationary reference frame, e is the back-EMF and the symbol $\wedge$ denotes estimated values. Then $A(\hat{\omega})$ is the system matrix consisting of machine parameter, B is a matrix composed by the inverse of the stator inductance, L is the feedback gain and I is the unit matrix.
It can be noticed that it consists in a MRAS where the rotor position estimate is

used to transform the measured current from stationary to synchronous reference frame. The output of the MRAS MBST is the back-EMF which, as it can be seen from figure 1.20, becomes the input of the speed estimator block which provide the estimated speed:

$$\hat{\omega} = \hat{\omega_0} + K\frac{\hat{e_d}\hat{e_q}}{\hat{e_d^2} + \hat{e_q^2}} \tag{1.61}$$

where K is the controller involving an integration and $\hat{\omega_0}$ is the speed calculated directly using the back-EMF e.

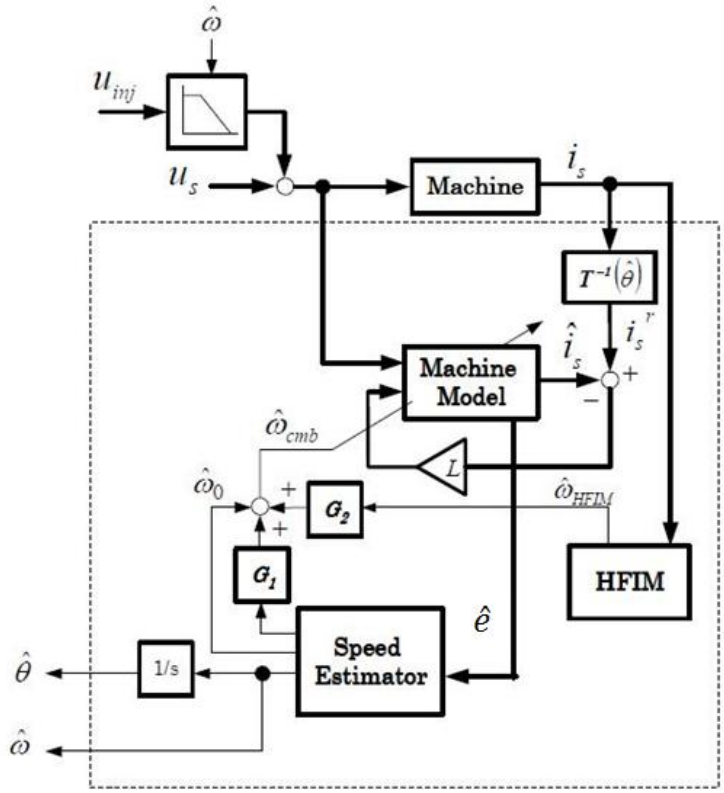

Figure 1.21: Position and speed estimator with proposed hybrid method [7]

Figure 1.22 shows the proposed combination between MBST and HFIST. The key technique is the changeover which is done only in the internal speed ω_{cmb}. It consists, in fact, in the estimated speed of both the HFIST and the MBST and it is set as follows:

$$\hat{\omega_{cmb}} = \hat{\omega_0} + G_1\hat{\omega} + G_2\hat{\omega_{HFIST}}$$

where G_1 and G_2 are weighting factors which are regulated along with the commanded and/or the estimated speed. As it has been said before, the rotor position estimation is only provided by the MBST. In fact the internal speed ω_{cmb} is only employed in the machine model of the MBST and not employed to

estimate the position of the polar axis. The estimated speed $\hat{\omega}$ is then calculated by equation 1.61 while the position is estimated by its integration.
A great advantage of this method is that the addition torque ripple and the acoustic noise due to the injected high-frequency signal are reduced because of the filtering effect of the MBST. Figure 1.22 shows the result of a experimental application of this technique, the improvement with respect to the use of only HFIST is readily visible. In fact, it can be seen from figure 1.22a, which represent the experimental result using the HFIST, that the torque ripple and consequently the speed ripple is much bigger (at least three times) than the torque and speed ripple in figure 1.22b using the method describe in this subsection.

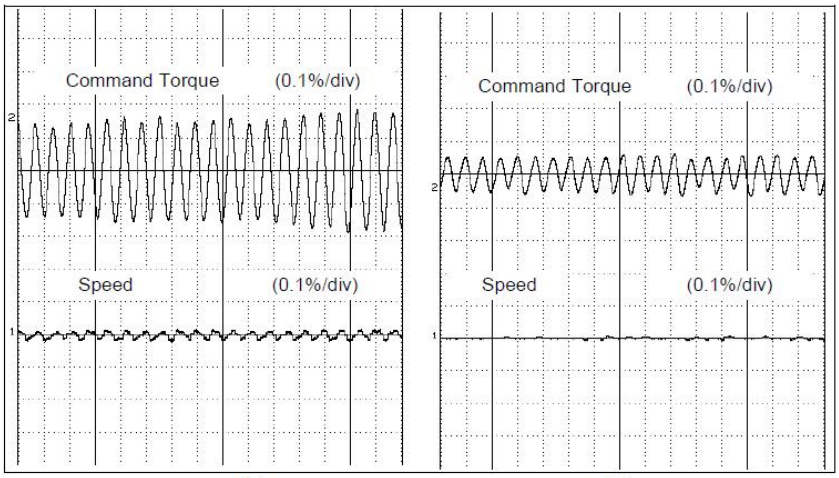

Figure 1.22: Waveform of the command torque and the measured speed at zero speed: (a)HFIST, (b)Hybrid method [7]

1.5.4. Hybrid Method Employing a Weighted Average of the Estimated Quantities [8]

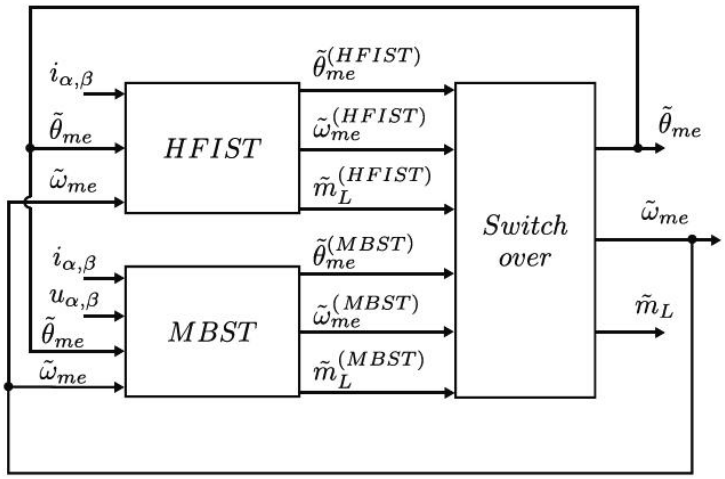

Figure 1.23: Block diagram of estimation scheme [8]

The scheme shown in figure 1.23 includes the two estimators, HFIST and MBST, that deliver respectively the estimated speeds $\omega^{H\hat{F}IST}$ and $\omega^{M\hat{B}ST}$, positions $\vartheta^{M\hat{B}ST}$ and $\vartheta^{H\hat{F}IST}$ and load torques $m_L^{H\hat{F}IST}$ and $m_L^{M\hat{B}ST}$.
The block called switch over receives these estimated quantities as input and determines the output: $\hat{\vartheta}$,$\hat{\omega}$ and $\hat{m_L}$ that are needed for the algorithm of the motor control. The strategy used to switch between the MBM to the HFIM, or viceversa, defines transition region with a weighted average of the estimated quantities by the two methods. Being N_1 and N_1 the lower and the higher limits of the transition region respectively, the strategy adopted can be briefly re-assumed in this way:

- for $|n| \leq N_1$

$$\tilde{\omega} = \omega^{H\hat{F}IST}$$
$$\tilde{\vartheta} = \vartheta^{H\hat{F}IST}$$

- for $N_1 < |n| < N_2$

$$\tilde{\omega} = \frac{N_2-|n|}{N_2-N_1}\omega^{H\hat{F}IST} + \frac{|n|-N_2}{N_2-N_1}\omega^{M\hat{B}ST}$$
$$\tilde{\vartheta} = \frac{N_2-|n|}{N_2-N_1}\vartheta^{H\hat{F}IST} + \frac{|n|-N_2}{N_2-N_1}\vartheta^{M\hat{B}ST}$$

- for $|n| \geq N_2$

$$\tilde{\omega} = \omega^{\hat{MBST}}$$
$$\tilde{\vartheta} = \vartheta^{\hat{MBST}}$$

1.5.5. Hybrid Method Employing a Linear Combination between Position Error Signals [10]

This method has been primarily developed to integrate the sensorless techniques in Hybrid Electric Vehicles (HEV) which nowadays are assuming an important role as alternative to conventional ICE vehicles and for this reason they are increasingly focusing the attention of researchers.
The main idea of the proposed transition is to use a linear combination between position error signals, not velocity or position, from both HFIST and MBST. The proposed transition differs from previous schemes, in several aspects:

- it requires a single tracking observer;
- it does not requires the use of weighting functions/transition parameters or adjust dual observer frequency characteristics;
- mode switchover occurs during a prescribed transition period;
- there is no need to reset or adjust the integrator of the tracking observer.

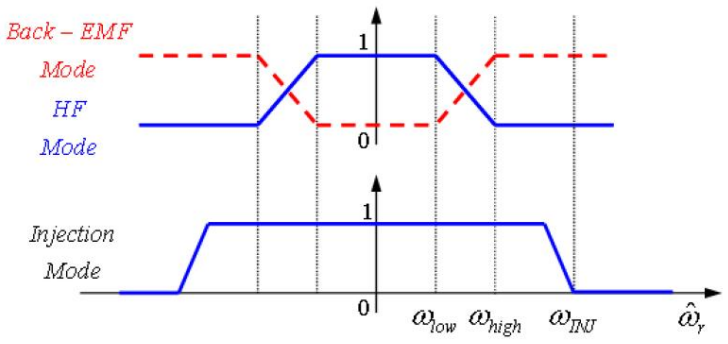

Figure 1.24: Schematic diagram of sensorless mode switching [10]

Figure 1.24 shows the mode switching graph, where the mode switching occurs the frequency range between ω_{low} and ω_{high}, and the HF signal injection ends (motoring operation) at the speed command of ω_{inj} to reduce additional losses. During mode switching, the error signal is calculated by multiplying the mode value of figure 1.24 by each error signal estimated from both the MBST and HFIST. Then, the summation of two signals becomes the input to a tracking observer.

1.5.6. Hybrid Method Employing Hall Sensors Combined with EKF [5]

This method differs from the methods previously described in the fact that it uses hall sensors instead of using HFIST to estimate the rotor position at zero and low-speed. The machine considered has a Halbach (self shielding) megetized permanent magnet rotor which is designed to present a sinusoidal airgap field distribution and a sinusoidal back-emf waveform. Two low-cost linear Hall sensors figure 1.25, whose output signals are proportional to the airgap flux density and vary sinusoidally and co sinusoidally with the rotor position are used to measure the instantaneous rotor position down to standstill.

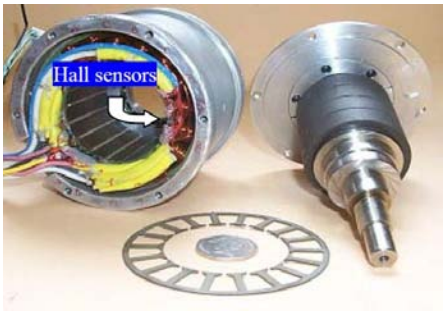

Figure 1.25: Halbach magnetised PM BLAC motor with linear Hall sensors [5]

The control of the machine is shown in figure 1.26 and it also includes the hybrid controller block. The hybrid strategy is implemented withih this block. A EKF is used to estimate the rotor position either from linear Hall sensors, from the MBST which calculates the flux due to the permanent magnet and from the hybrid controller system.

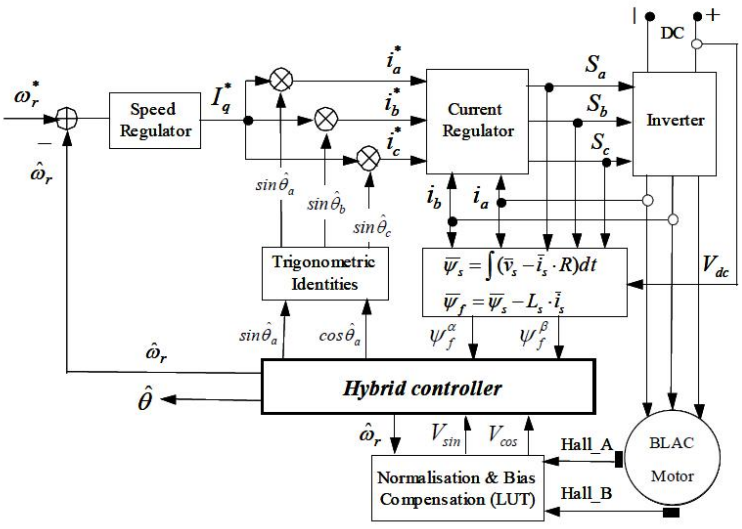

Figure 1.26: Schematic of vector-controlled BLAC drive system with a hybrid controller [5]

The complete hybrid controller is shown in figure 1.27 where a hysteresis switch is implemented to select the input to the EKF. Of course, switching from one set of input signals to the other may still result in a sudden change in the EKF inputs, S_A and S_B. However, this is be modeled as noise or a disturbance, and the output signals ($\hat{\vartheta}$ and $\hat{\omega_r}$) will be smoothed by means of the EKF.

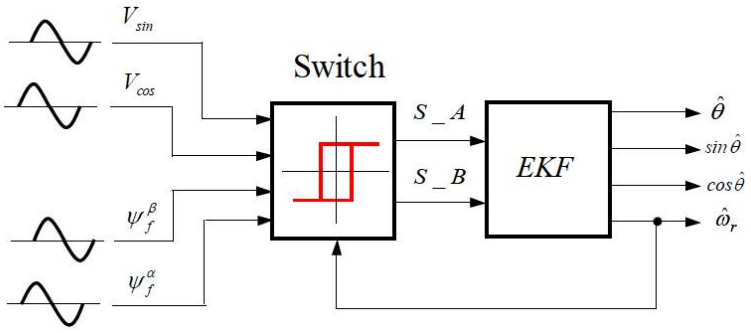

Figure 1.27: Hybrid controller with one EKF [5]

CHAPTER 2

MODEL BASED SENSORLESS TECHNIQUE

2.1. Introduction

Before developing the Hybrid strategy which combines low and zero speed operation (using HFIST) with medium-high speed operation (using MBST), it is necessary to develop and tune these two methods.
This chapter deals with MBST while HFIST will be presented in Chapter 3. Finally in Chapter 4 these two sensorless strategies will be combined into a single estimation scheme, the hybrid model, which enables the motor operation in the whole speed range.
The simulation software that has been are Simulink and Matlab 2010. For all the simulations a time step size of $T_s = 1e-6$ has been used. Due to memory constraints, the duration of the simulation was set to 0.5s. Though in some instances it would have been convenient to have larger simulation times, 0.5s was found to be sufficient for the analysis of the most important aspects of the methods.
The motor used for the project is an interior permanent magnet synchronous machine (IPMSM) with a quite strong anisotropy which, as it has been said in Chapter 1 and it will resumed in the next chapter, helps in the detection of the rotor position at low or zero operation speeds. This motor is located at the Electrical Engineering Department facilities, at the University of Oviedo. The IPMSM is coupled with a vector controlled induction machine. The main parameters of the IPMSM are shown in the following table:

Parameters	**Values**
Power	8650 W
Rated Torque	55 Nm
Rated Speed	1500 rpm
Rated Phase Voltage	300 V (peak value)
Rated Phase Current	14 A (rms value)
Pole pairs (P)	3
Stator resistant (R_s)	1.7 Ω
d-axis inductance (L_d)	0.00205 H
q-axis inductance (L_q)	0.00391 H
Magnet flux Ψ_{pm}	0.64 Vs

For the IPMSM and drive Simulink model, a model kindly provided by Ph.D. student Mario López was initially used. This model implemented the vector control of a IPMSM machine, including the speed control loop and a MTPA control strategy for the IPMSM (see Appendix A). The parameters of this model were adapted to the parameters of the machine used in the experimental set up. The controllers gains selection process is as follows:

- k_{Pi}, k_{Ii} have been calculated from the bandwidth f_{bw} of the PI regulator (set at 400 Hz), and the inductances of the d-q axes with the following equations:

$$k_{Pi} = 2\pi f_{bw} L$$
$$k_{Ii} = 2\pi f_{bw} L \frac{1}{\tau_{Ii}}$$

  with L assuming the value L_d or L_q respectively for the d-axis current PI current regulator and the q-axis current PI regulator and $\tau_{Ii} = \frac{L}{R_s}$ time constant of the current PI regulators.

- $k_{P\omega}$, $k_{I\omega}$ have been chosen in order to provide to the PI speed regulator a slower dynamic than the PI current control and a good behavior in both MBST and HFIST operations. These parameters assume respectively the values of 0.8 and 8.

2.2. Implementation of the MBST

A open loop estimator of the type discussed in Chapter 1 was used for the MBST (see figure 1.3). The rotor position and speed are obtained from the commanded stator voltages and the measured stator currents. As already mentioned in Chapter 1, while for SPMSM only one term of the voltage equation is function of the rotor position (see equation 1.13), in the IPMSM (see equation 1.14) there are two terms which depend on the rotor position. Introducing the extended back-EMF concept using either equation 1.15 or 1.17 its is possible to obtain an equivalent equation in which only one term is function of the rotor position. Equation 1.15 will be used in this thesis, the resulting equations being:

$$\begin{vmatrix} e_d^s \\ e_q^s \end{vmatrix} = \begin{vmatrix} v_d^s \\ v_q^s \end{vmatrix} - \begin{vmatrix} R & 0 \\ 0 & R \end{vmatrix} \begin{vmatrix} i_d^s \\ i_q^s \end{vmatrix} - \frac{d}{dt} \cdot \begin{vmatrix} L_q & 0 \\ 0 & L_q \end{vmatrix} \begin{vmatrix} i_d^s \\ i_q^s \end{vmatrix} \tag{2.1}$$

where e_{dq}^s is given in magnitude and phase by equation 1.18.
Starting from 1.18 it is possible to get the two components of e_{dq}^s:

$$\begin{vmatrix} e_d^s \\ e_q^s \end{vmatrix} = \omega\psi_{ext} \begin{vmatrix} -\sin(\vartheta_r) \\ \cos(\vartheta_r) \end{vmatrix} + (L_d - L_q)\frac{d}{dt} \cdot i_d^r \begin{vmatrix} \cos(\vartheta_r) \\ \sin(\vartheta_r) \end{vmatrix} \tag{2.2}$$

Equation 2.2 shows that the rotor position information is present in two terms and for this reason is still difficult to estimate it. However, in some specific applications if $(Ld - Lq)\frac{d}{dt}(i_d^r) << \omega_r\psi_{ext}$is satisfied or in steady state operations when the $\frac{d}{dt}(i_d^r) = 0$, the last term in equation 2.2 can be ignored and the position estimation will be notably simplified.
On the contrary, considering also the second component of 2.2 it is possible to write the extended back-EMF e_{dq}^s as a complex vector with magnitude A and phase φ in the following way:

$$\begin{aligned} &e_{dq}^s = \omega_r\psi_{ext}(-\sin(\vartheta_r) + j\cos(\vartheta_r)) + \tfrac{d}{dt}(\psi_{ext})(\cos(\vartheta_r) + j\sin(\vartheta_r)) = \\ &= j\omega_r\psi_{ext}e^{j(\vartheta_r)} + \tfrac{d}{dt}(\psi_{ext})e^{j(\vartheta_r)} = Ae^{j(\vartheta_r+\varphi)} \end{aligned} \tag{2.3}$$

where:

$$\begin{aligned} A &= \sqrt{(\tfrac{d}{dt}(\psi_{ext}))^2 + (\omega_r\psi_{ext})^2} \\ \varphi &= tan^{-1}(\tfrac{\omega_r\psi_{ext}}{\frac{d}{dt}(\psi_{ext})}) \end{aligned} \tag{2.4}$$

As it can be seen from equation 2.3, e_{dq}^s contains the rotor position information but with a certain error equal to φ which has to be compensated. In this particular application it has been neglected the second component of e_{dq}^s since the derivate of i_d^r is equal to zero in steady state operation and also during transients it can be

safely neglected. Therefore, equation 2.1 has been used to obtain the extended back-EMF e^s_{dq} from which the flux ψ^s_{dq} is obtained by integration. The flux ψ^s_{dq} is the input of the Phase-Lock Loop (PLL), from which the rotor position and speed are obtained.
Hence, the target of this estimator is to obtain the extended back-EMF e^s_{dq} and then the flux ψ^s_{dq} using the measured phase currents and commanded voltage. Transformation g^s_{dq} is used to obtain the voltage an current vectors from the corresponding three-phase quantities:

$$g^s_{dq} = \frac{2}{3}(g_a + g_b e^{j(\frac{2\pi}{3})} + g_c e^{j(\frac{4\pi}{3})}) \tag{2.5}$$

from which the two components g^s_d and g^s_q are derived:

$$\begin{aligned} g^s_d &= g_a \\ g^s_q &= \tfrac{1}{\sqrt{3}}(g_b - g_c) \end{aligned} \tag{2.6}$$

Figure 2.1 shows the block diagram used to estimate the stator flux components ψ^s_{dq}.

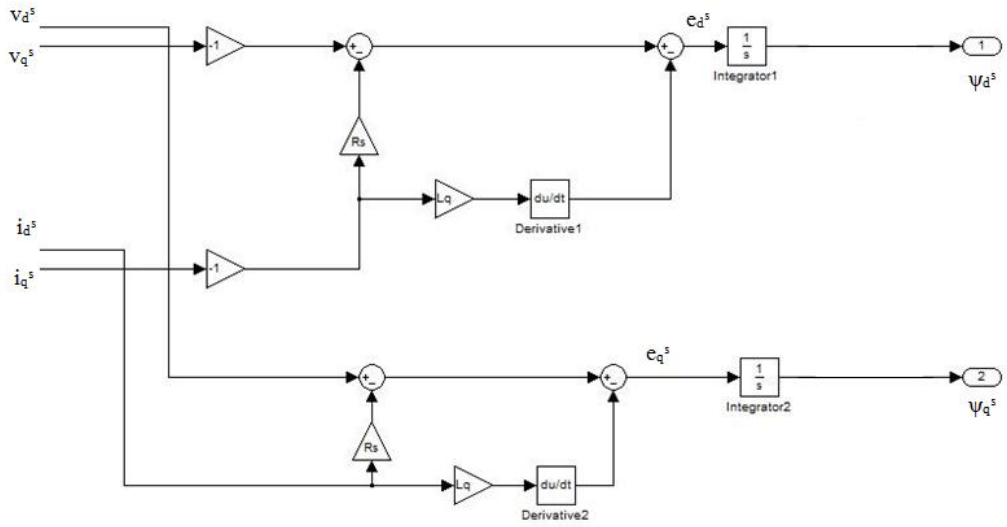

Figure 2.1: Block diagram of the flux estimator

In a real implementation, the pure integrator needs to be replaced by a first order low pass filter LPF with a cut off frequency f_{cut} lower than the smallest speed ω_{min} at which the MBST operates. The transfer function of this filter is:

$$\frac{Output}{Input} = \frac{\tau}{1+\tau s} \tag{2.7}$$

with $\tau = 1/(2\pi f_{cut})$.
Equation 2.7 has the same frequency response as the pure integrator $1/s$ for the frequencies of interest assuming that the following relationship holds:

$$\omega_{min} > \frac{1}{\tau} \tag{2.8}$$

where ω_{min} is the angular frequency at which the extended back-EMF will occur.
Finally, the output of the observer is the input of a Phase-Lock Loop (PLL) which is used to track the rotor position. PLLs are widely used in the electric and electronic fields to obtain the frequency an phase of a signal. As shown by figure 2.2, a PLL consists of a PI regulator followed by an integrator where the output of the PI regulator is the angular speed of the rotor which integrated by the integration block provides the rotor position. The flux ψ^s_{dq} which consists in a space vector is normalized to p.u., by dividing it by its magnitude. Then, as figure 2.2 shows, a vector cross product is implemented between ψ^s_{dq} and the signal used for the feedback of the PLL. The error ϵ, will be the input to the PI regulator, being given by the following equation:

$$\epsilon = \sin(\vartheta_r - \tilde{\vartheta}_r) = \psi^s_{q(p.u.)}\cos(\tilde{\vartheta}_r) - \psi^s_{d(p.u.)}\sin(\tilde{\vartheta}_r) \tag{2.9}$$

The error ϵ can be approximated by the following expression, provided that the difference $\vartheta_r - \tilde{\vartheta}_r$ is small:

$$\epsilon = \vartheta_r - \tilde{\vartheta}_r \tag{2.10}$$

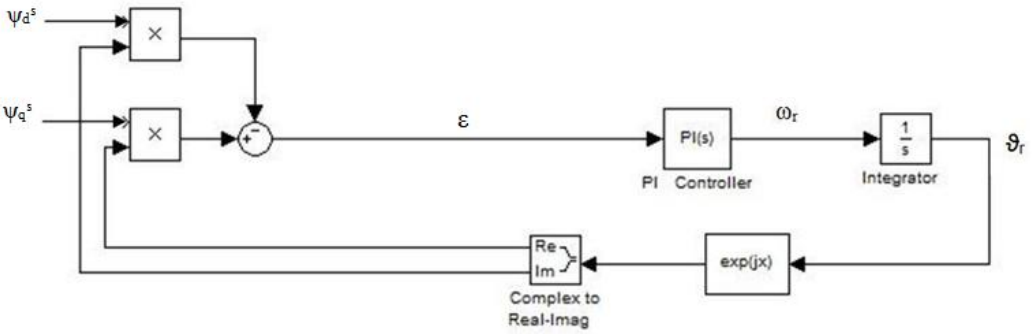

Figure 2.2: Block diagram of the implemented PLL

The gains selected for k_p and k_i for the PLL PI regulator are 500 and 2000 respectively. This gains were found to provide fast dynamics and guarantee stable operation.

2.3. Simulation Results for the MBST

Simulation results shown the performance of the MBST are provided in this section, three different operating speeds being used for this propose:

- $\omega_{ref} = 10Hz$, which is the minimum speed at which the control operates using the MBST. In this simulation the motor is operating with no load;
- $\omega_{ref} = 30Hz$, which is a medium-range operating speed. For this simulation the load was set to $T = 30Nm$, which corresponds to approximately half of the nominal load. To demonstrate that the control using MBST is perfectly symmetric, the same test was repeated with a negative reference speed of $\omega_{ref} = -30Hz$ and with a negative load of $T = -30Nm$;
- $\omega_{ref} = 75Hz$ which is to the nominal speed of the machine. In this simulation the motor is operating with no load;

Finally, the dynamic response of the MBST will be evaluated by commanding a sudden change in the speed.

2.3.1. 10 Hz Operating Speed

This section shows the simulation results obtained commanding a reference speed ω_{ref} of 10 Hz with no load.
The relationship between electrical and mechanical speeds is given by:

$$\omega_e = P \cdot \omega_m \tag{2.11}$$

All the speeds are given in [rpm], hence:

$$\omega_{m[rpm]} = 60 \cdot \omega_m = 60 \cdot \frac{\omega_e}{P} \tag{2.12}$$

which in this case yields

$$\omega_{m[rpm]} = 60 \cdot \omega_m = 60 \cdot \frac{\omega_e}{P} = 60 \cdot \frac{10}{3} = 200rpm \tag{2.13}$$

The results shown are:

- Figure 2.3 shows the mechanical reference speed, the estimated speed and the speed measured by the encoder. As figure 2.3 shows, the behavior of the motor at the minimum speed at which it has to operate with the MBST is very good.

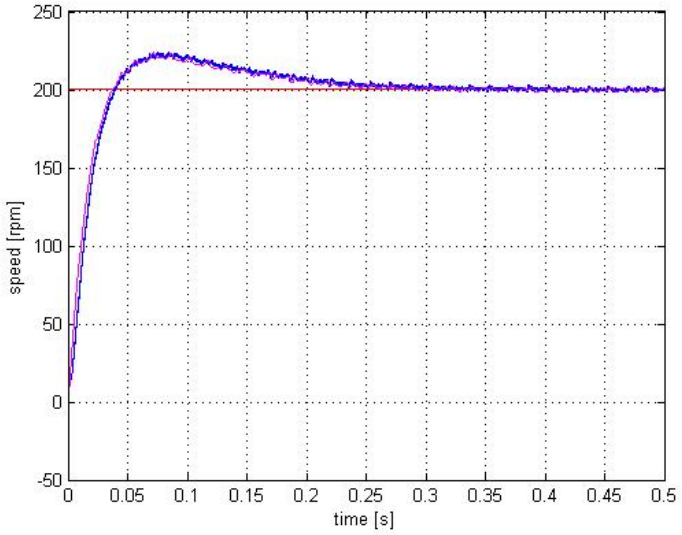

Figure 2.3: Reference speed (red), measured speed (blue), estimated speed (magenta) [rpm]

- Figure 2.4 shows the estimated mechanical angle and the mechanical angle measured by the encoder. It is interesting to notice that at the very beginning a very small error exists between the measured angle and the estimated angle and that it gradually decreases until it disappears at the end of the simulation time. This is due to the dynamic of the PLL that takes a certain time to reach steady state operating conditions.

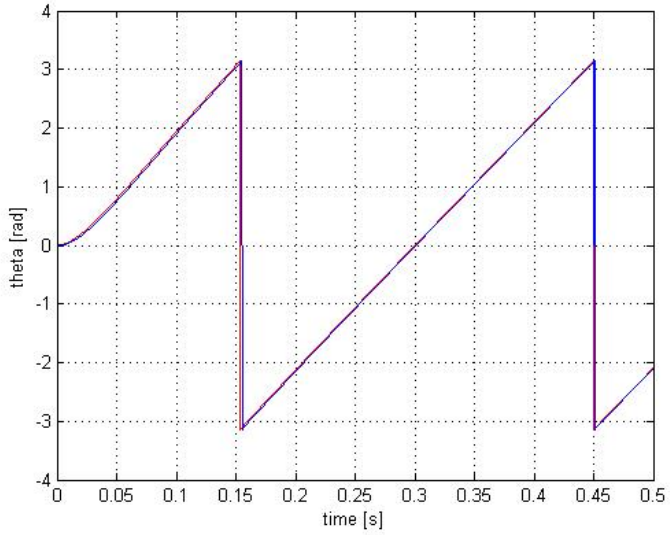

Figure 2.4: Measured angle (red) and estimated angle (blue) [rad]

- Figure 2.5 shows the d-axis (red line) and q-axis (blue line) components of the estimated flux ψ^s_{dq}. The ψ^s_d and ψ^s_q components are two perfect sinusoidal waves oscillating at a frequency of 10 Hz (electrical frequency).

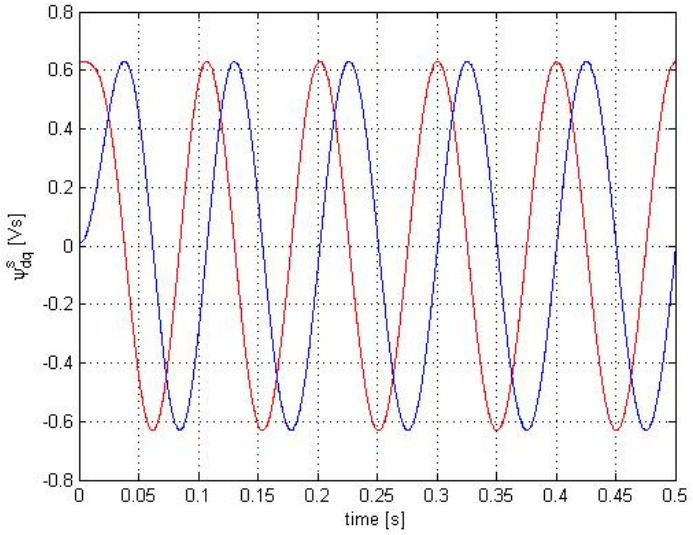

Figure 2.5: d (red) and q (blue) components of the estimated flux [Vs]

2.3.2. 30 Hz Operating Speed with 30 Nm Load

In this simulation a 30 Nm load was applied to the machine. It is noted that due to the simulation time limit (0.5s), with larger loads the motor cannot reach steady state in the simulation time.

- Figure 2.6 shows the mechanical reference speed, the estimated speed and the speed measured by the encoder. At the very beginning (less than 0.05 s) the speed of the motor is negative due to the big load applied as a step from the beginning. After a very short period of time the dynamic of motor is able to contrast the load and to speed up reaching the steady state operating condition in less than 0.5 s.

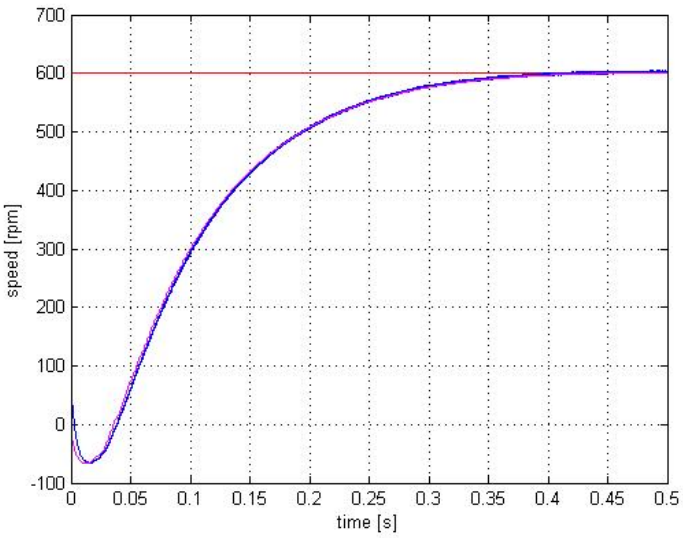

Figure 2.6: Reference speed (red), measured speed (blue), estimated speed (magenta) [rpm]

- Figure 2.7 shows the estimated mechanical angle and the mechanical angle measured by the encoder. The same comments of the previous simulation can be made here.

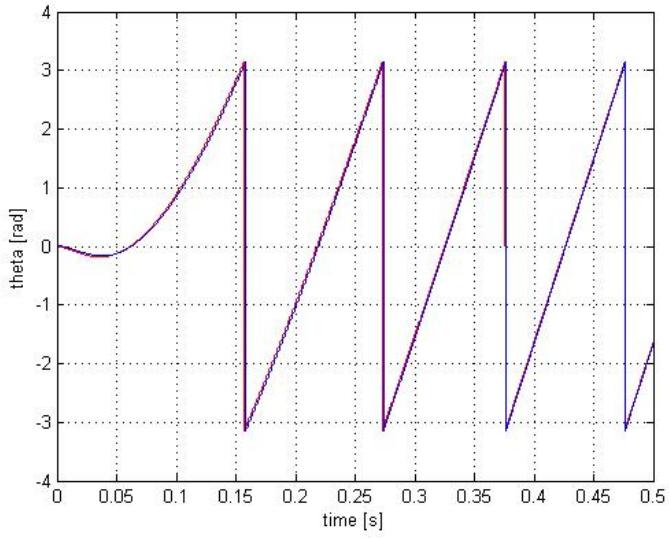

Figure 2.7: Measured angle (red) and estimated angle (blue) [rad]

- Figure 2.8 shows the commanded torque, which is the output of the speed regulator. After an initial peak needed to speed up the machine, the torque reaches the reference values plus the friction in the simulation time.

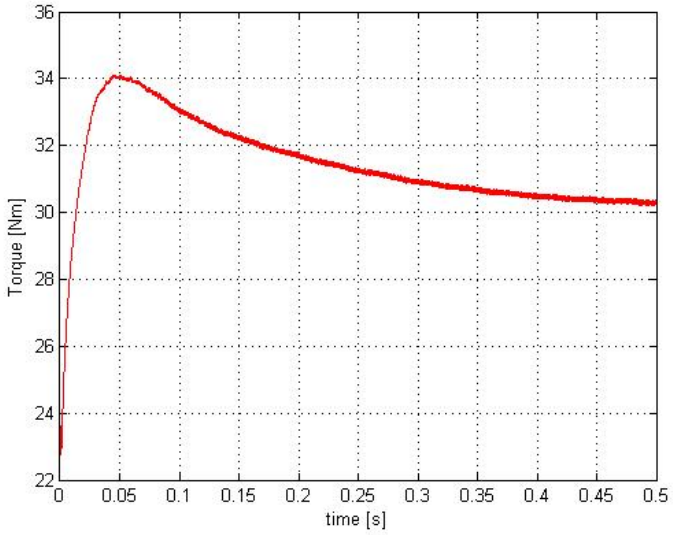

Figure 2.8: Torque output of the speed regulator [Nm]

- Figure 2.9 shows the three-phase current applied to the motor.

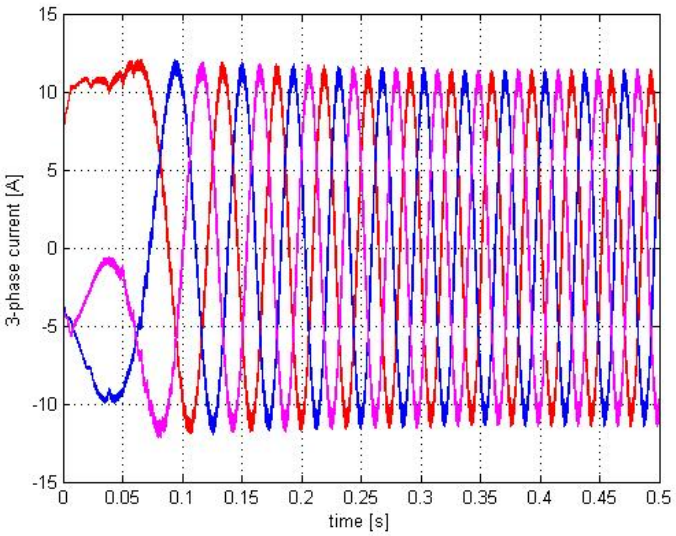

Figure 2.9: Phase currents [A]

2.3.3. -30 Hz Operating Speed with -30 Nm Load

The target of this simulation is to verify the symmetric operation between negative and positive operating speeds. The simulation results are organized similar to the previous simulation:

- Figure 2.10 shows the mechanical reference speed, the estimated speed and the speed measured by the encoder.

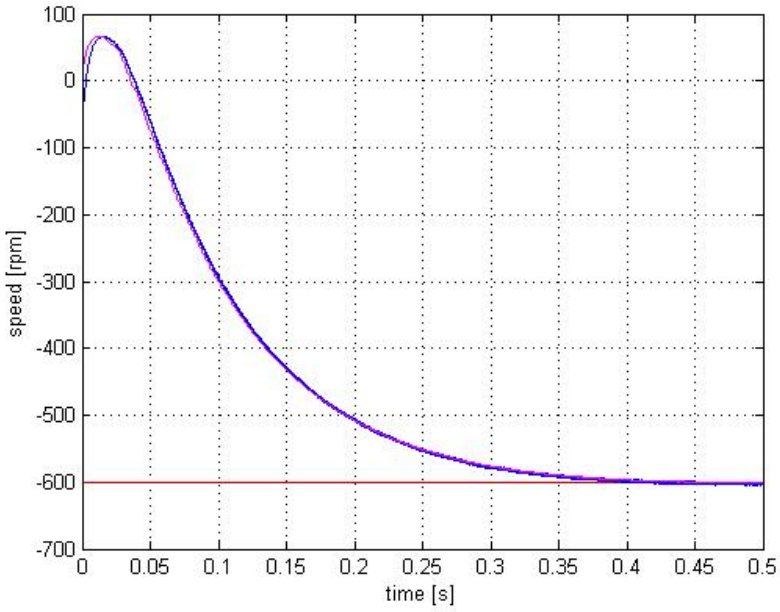

Figure 2.10: Reference speed (red), measured speed (blue), estimated speed (magenta) [rpm]

- Figure 2.11 shows the estimated mechanical angle and the mechanical angle measured by the encoder.

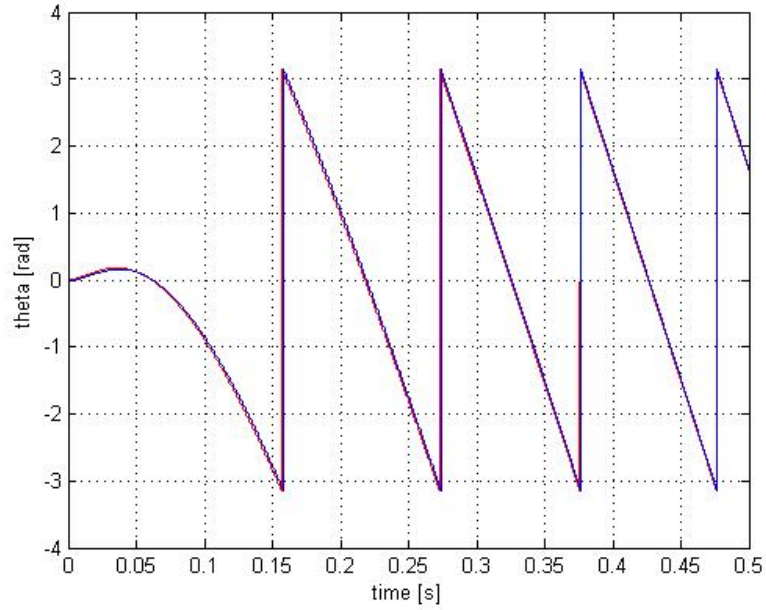

Figure 2.11: Measured angle (red) and estimated angle (blue) [rad]

- Figure 2.12 shows the commanded torque, which is the output of the speed regulator.

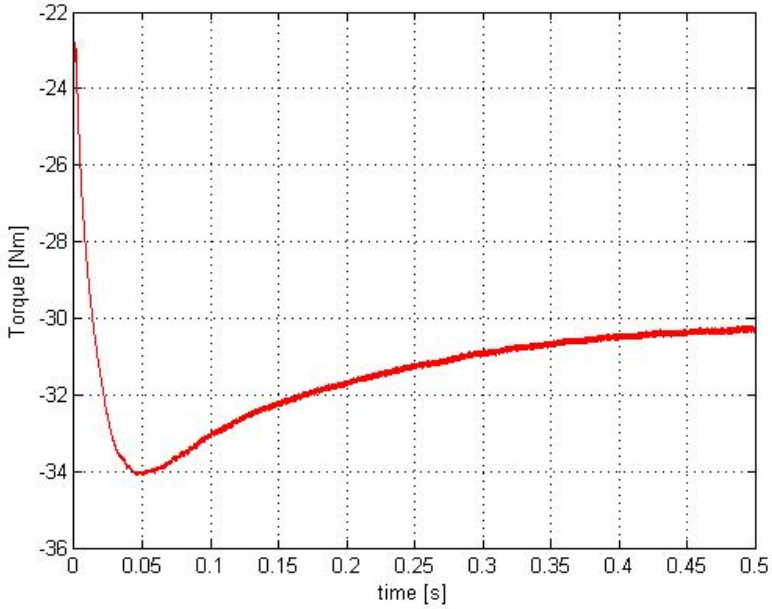

Figure 2.12: Torque output of the speed regulator [Nm]

- Figure 2.13 shows the three-phase current applied to the motor.

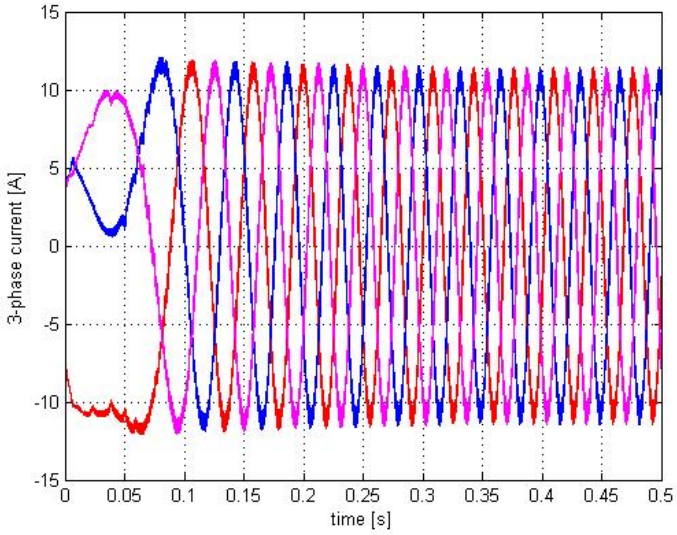

Figure 2.13: Phase currents [A]

2.3.4. 75 Hz Operating Speed

This operating condition corresponds to the nominal speed of the motor. In particular the results shown are:

- Figure 2.14 shows the mechanical reference speed, the estimated speed and the speed measured by the encoder.

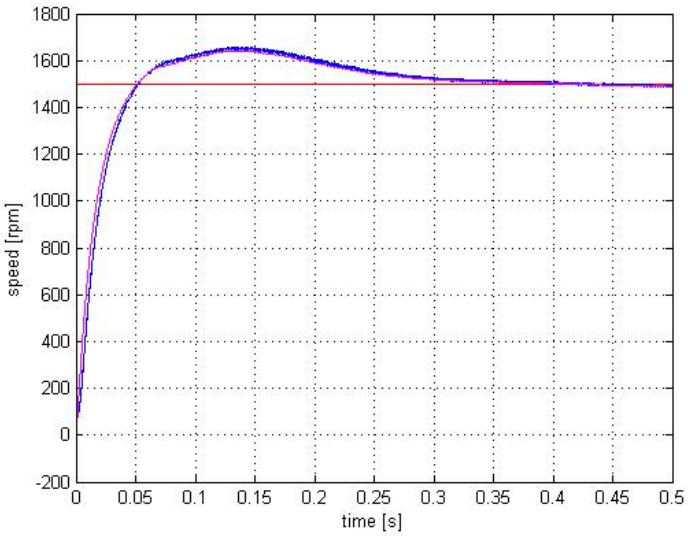

Figure 2.14: Reference speed (red), measured speed (blue), estimated speed (magenta) [rpm]

- Figure 2.15 shows the estimated mechanical angle and the mechanical angle measured by the encoder.

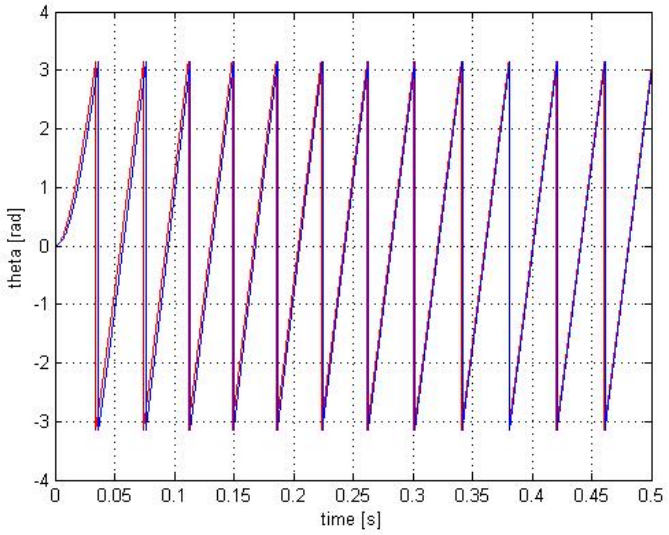

Figure 2.15: Measured angle (red) and estimated angle (blue) [rad]

- Figure 2.16 shows the d-axis (red line) and q-axis (blue line) components of the estimated flux ψ^s_{dq}.

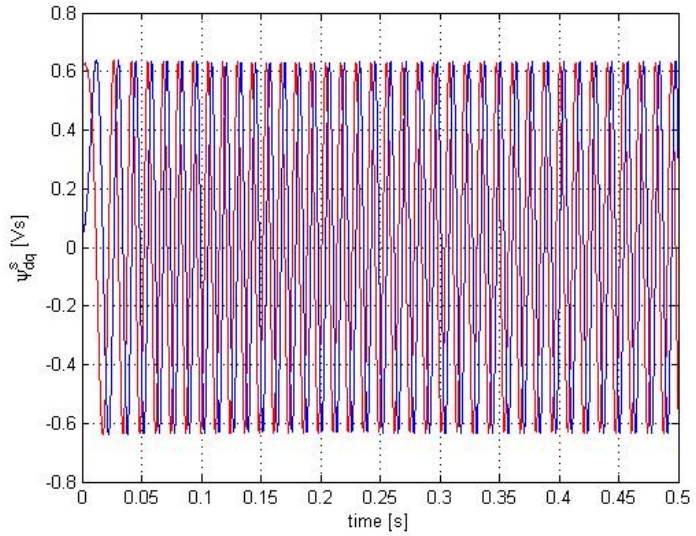

Figure 2.16: d (red) and q (blue) components of the estimated flux [Vs]

2.3.5. Multiple Operating Speeds

This simulation illustrates the dynamic of the MBST. The reference speed changes among five different values: 0 Hz, 55 Hz, 30 Hz, 15 Hz and finally 25 Hz. The simulation results are the following:

- Figure 2.17 shows the mechanical reference speed, the estimated speed and the speed measured by the encoder. The dynamic of the machine considered is very as fast it can follow the reference speed with a delay of few ms even with sudden changes in the speed commands.

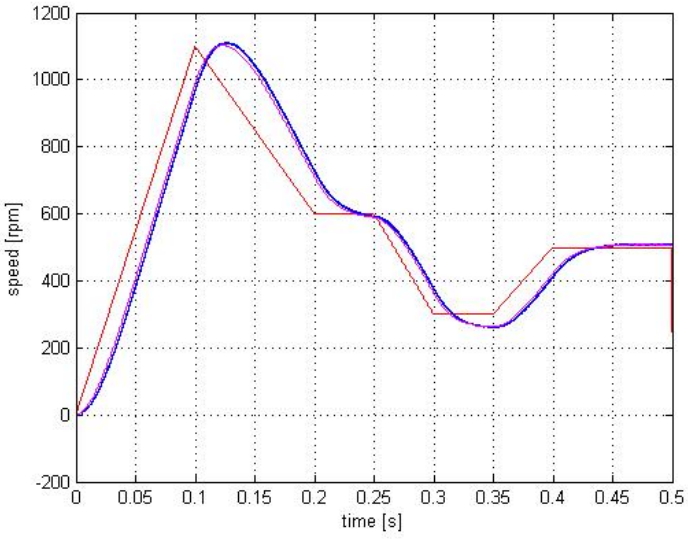

Figure 2.17: Reference speed (red), measured speed (blue), estimated speed (magenta) [rpm]

- Figure 2.18 shows the estimated mechanical angle and the mechanical angle measured by the encoder.

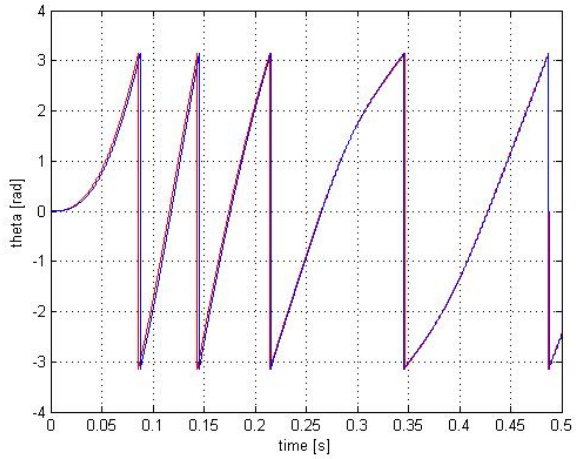

Figure 2.18: Measured angle (red) and estimated angle (blue) [rad]

- Figure 2.19 shows the d-axis (red line) and q-axis (blue line) components of the estimated flux ψ^s_{dq}. The frequency of the estimated flux ψ^s_{dq} is changing with the speed of the machine.

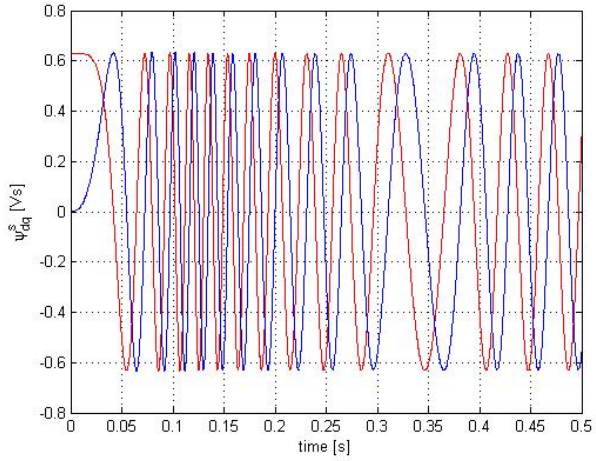

Figure 2.19: d (red) and q (blue) components of the estimated flux [Vs]

2.4. Conclusions

In this chapter, the MBST have been implemented employing an open-loop estimator.
As it is observed from the simulation results, the sensorless control of the IPMSM employing the MBST is very reliable, being possible to speed up the machine from zero speed. This is only possible due to the ideal behavior of the electronics and machine used in the simulation but would not be possible in a real implementation, due to the errors in the measurements and in the parameters of the machine and the non-ideal behavior of the system machine, inverter, sensors, etc.

CHAPTER 3

HIGH FREQUENCY INJECTION SENSORLESS TECHNIQUE

3.1. Introduction

This chapter deals with the HFIST used in the low and zero operative speeds. While Chapter 1 presents a panoramic view of the different HFIST which have been proposed, now the attention will be focused only in the method that has been chosen for this project, which injects a high frequency rotating carrier voltage vector.
The chapter is divided in two parts: the first one deals with all the theoretical aspects of this specific HFIST while the second presents the results of the simulation carried out with Simulink. In the latter the results of the simulation regarding the position control of the motor will be also shown.
The motor parameters, the gains of the speed and current PI regulators and all the aspects related to the algorithm control of the electric drive were presented in Chapter 2.

3.2. Implementation of the HFIST

The method that has been chosen injects a high frequency rotating carrier voltage vector. In this section all the theoretical aspects that are behind this technique will be developed in detail.

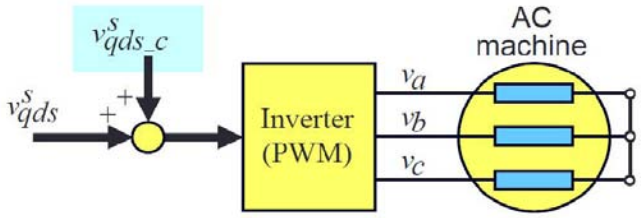

Figure 3.1: Block diagram representing the injected voltage signal superimposed with the fundamental voltage [12]

This method consists in the injection in the motor of an high frequency rotating carrier voltage superimposed to the fundamental voltage which feeds the machine. This voltage component has a magnitude V_c of the order of some percent of the DC voltage to which the inverter is connected and it presents a pulsation ω_c in the range of a several hundred Hz to a few kHz. The values of 30 V and 1000 Hz have been chosen respectively for the magnitude V_c and the frequency f_c of the rotating carrier voltage. As the DC voltage is set at 300 V the magnitude V_c of the rotating carrier voltage is its 10 %.
Figure 3.1 shows the block diagram of the high frequency voltage injection while figure 3.2 represents, in the complex plane, the signal injected which is given analytically by equation 3.1.

$$v^s_{qd_c} = V_c e^{j(\omega_c t)} \tag{3.1}$$

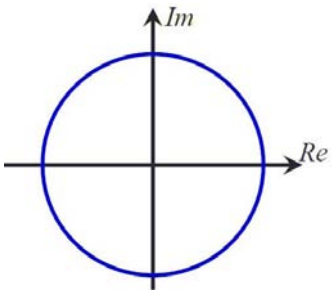

Figure 3.2: Representation of the voltage signal injected in the complex plane [12]

The signal injected corresponds to a set of balanced 3-phase voltages represented in figure 3.3 which can be written in the following way:

$$\begin{aligned} v_a &= V_c \cos(\omega_c t) \\ v_b &= V_c \cos(\omega_c t - \tfrac{2\pi}{3}) \\ v_c &= V_c \cos(\omega_c t - \tfrac{4\pi}{3}) \end{aligned} \tag{3.2}$$

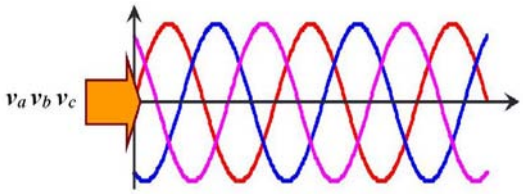

Figure 3.3: 3-phase representation of the voltage signal injected

which yields, after transforming it in a complex vector in the stationary reference (see figure 3.4), to equation 3.3.

$$\begin{aligned} v_d^s &= V_c \cos(\omega_c t) \\ v_q^s &= V_c \sin(\omega_c t) \end{aligned} \tag{3.3}$$

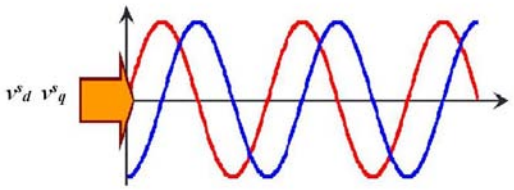

Figure 3.4: Representation in the stationary reference frame of the voltage signal injected

The injected voltage interacts with the saliencies of the machine due to the different inductances in the d and q axes.The resulting current is modulated by the rotor anisotropy as follows:

- If the rotor machine is perfectly isotropy, the resulting current can be represented in the complex plane by a circle as shown in figure 3.5, while the d and q components in the stationary reference frame are shown in figure 3.6. It can also be noticed that the phase delay between the injected voltage and the resulting current is almost 90 deg, which is in good agreement with the inductive behavior of the high-frequency model presented in Chapter 2.

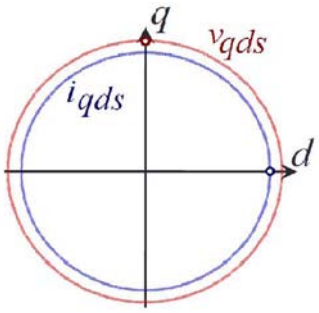

Figure 3.5: Representation of the voltage signal injected and of the resulting current in the complex plane in an isotropy machine [12]

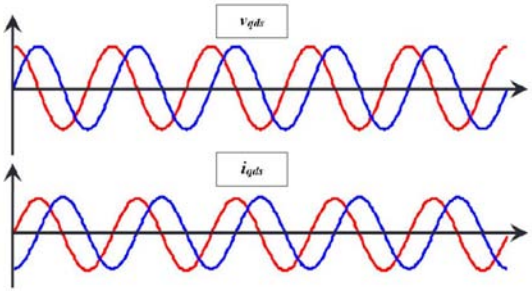

Figure 3.6: Representation of the voltage signal injected and of the resulting current in the stationary reference frame in an isotropy machine

- For the case of an anisotropy between the d and q axes exists, the resulting current presents different values respectively in the d and q components (see figure 3.8). In particular, being the inductance of the d axis lower than the one in the q axis, the d component results bigger than the q one. Now the representation in the complex plane of the current is not anymore a circle but an ellipsis with the main axis oriented in the direction of the rotor magnet d-axis (see figure 3.7).

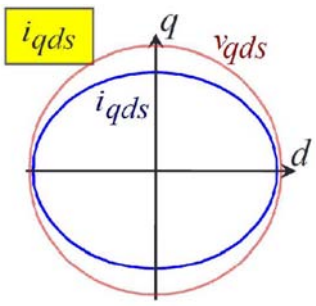

Figure 3.7: Representation in the complex plane of the voltage signal injected and of the resulting current in an anisotropy machine [12]

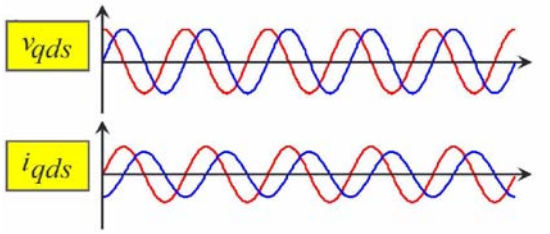

Figure 3.8: Representation in the stationary reference frame of the voltage signal injected and of the resulting current in an anisotropy machine [12]

- Finally figure 3.9 and 3.10 show respectively the rotating vector in the complex plane and the wave form of the current with a great rotor anisotropy.

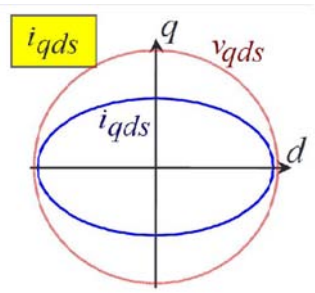

Figure 3.9: Representation in the complex plane of the voltage signal injected and of the resulting current in a strongly anisotropy machine [12]

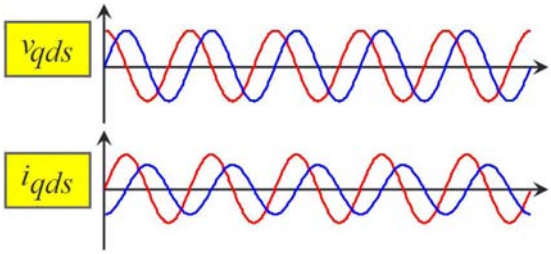

Figure 3.10: Representation in the stationary reference frame of the voltage signal injected and of the resulting current in a strongly anisotropy machine [12]

The current produced by the injection of the high frequency rotating carrier voltage, as it has already been said in Chapter 1, consists of two components: the positive and the negative sequence current, but only the latter is modulated by the rotor position. During the normal operation of the drive, the measured current will consist of three components: the fundamental component, and the positive and negative sequence components. The expression of the current can be given, as space vector, by:

$$i^s_{qd} = i^s_{qd_{cn}} + i^s_{qd_{pn}} + i^s_{qd_f} = -jI_{cn}e^{j(h_r\vartheta_r - \omega_c t)} - jI_{cp}e^{j\omega_c t} + I_f e^{j\omega_e t} \tag{3.4}$$

where the magnitude of the positive sequence current I_{pn} and of the negative sequence current I_{cn} are given by equation 1.34.
All the components of the measured current can be represented in a complex plane as it is shown in figure 3.11 and the frequency spectrum can be calculated using the Fast Fourier Transform (FFT) (see figure 3.12).

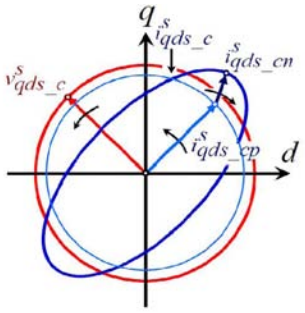

Figure 3.11: Representation in the complex plane of the voltage signal injected and of the positive and negative sequence resulting currents for the case of a salient machine [12]

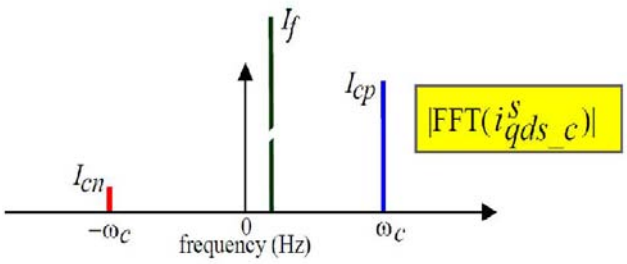

Figure 3.12: FFT of the resulting measured current for the case of a salient machine [12]

During the normal operation of the motor, the fundamental current can be easily in the range of three-full orders of magnitude larger than the negative sequence carrier signal current, so the measurement must be very precise for a good rotor position estimation.

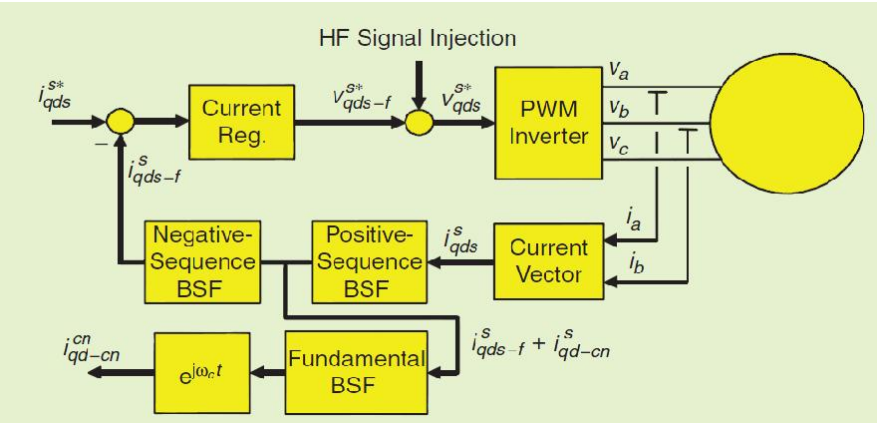

Figure 3.13: Schematic representation of the signal processing used to isolate the negative-sequence carrier-signal current [13]

Figure 3.13 shows the block diagram of the signal processing that will be used to isolate the negative-sequence carrier-signal current. First of all it is important to underline that, as it is shown in figure 3.13, the feedback of the current in the current regulator is filtered to separate the fundamental component of the current. To achieve this, band-stop filters (BSFs) can be used to eliminate the carrier-signal current to prevent the reaction of the fundamental current controller against this current. A BSF tuned for a frequency of $\pm\omega_c$ and a bandwidth of 100 Hz has been used to get rid of the positive sequence current. The elimination of the negative sequence current requires and adaptive BSF as the frequency of this signal changes with the operating speed. However, as the difference of frequency (in absolute value) between positive and negative sequence current is in the range few percent of the carrier frequency ω_c, the negative sequence current can be partially filtered by the BSF implemented. The Bode diagram of the transfer function of the considered BSF is shown in figure 3.14.

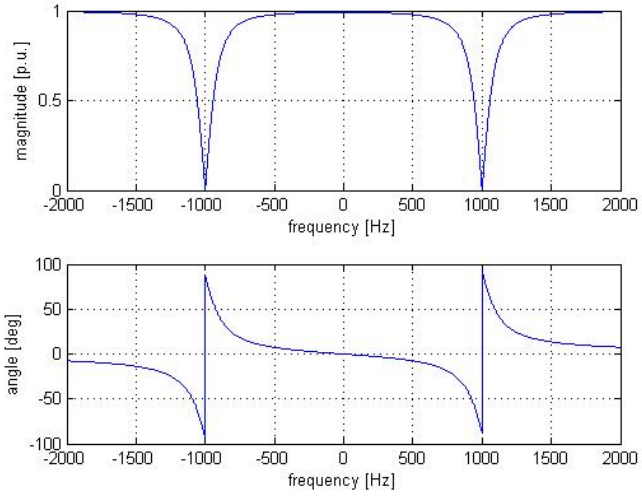

Figure 3.14: Bode diagram of the second order BSF

To obtain the negative sequence current the following two steps are needed:

- After rotating the measured current vector to a reference frame synchronous with the rotor, a HPF is used to eliminate the fundamental component of the current. Then the resulting current, is transformed again to the stationary reference frame. The output of this process is given by equation 3.5.

$$i^s_{qd_c} = i^s_{qd_{cn}} + i^s_{qd_{pn}} = -jI_{cn}e^{j(h_r\vartheta_r - \omega_c t)} - jI_{cp}e^{j\omega_c t} \tag{3.5}$$

This first step is schematically represented by the block diagram of figure 3.15, also the corresponding inputs and outputs (both wave shapes and FFT) are shown.

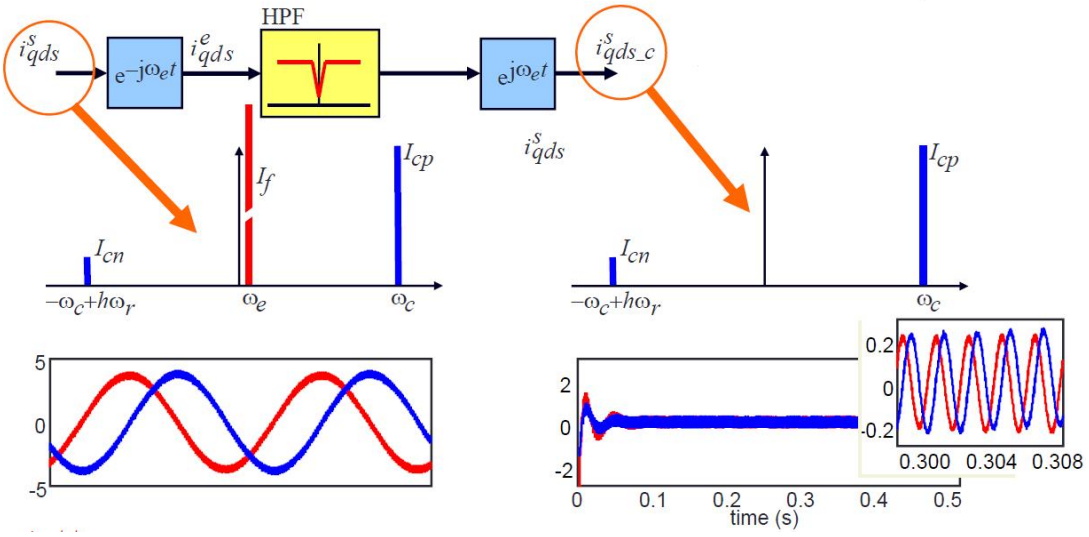

Figure 3.15: Block diagram of the first step of the signal processing and, including FFT and wave shapes of the input and output [12]

A second order HPF with a cut off frequency $f_{cut} = 5Hz$ has been used. The value of f_{cut} is very small as the signal to get rid off is at 0 Hz shows the Bode diagram of the transfer function of the second order HPF.

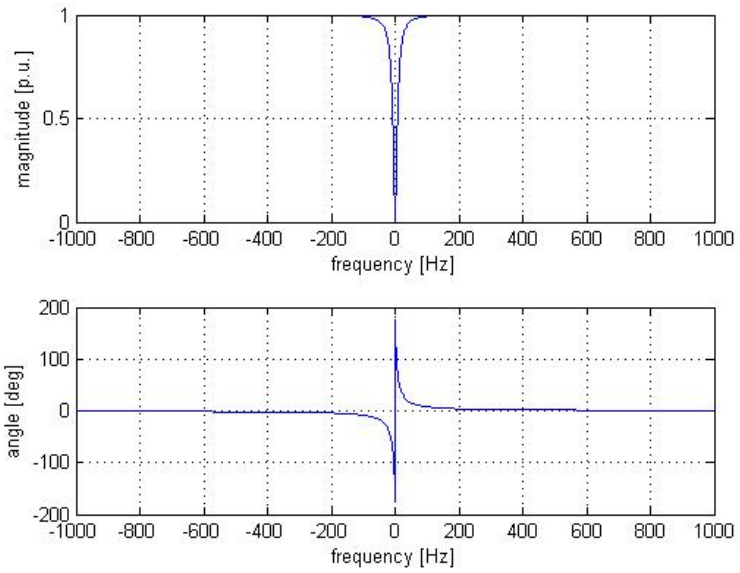

Figure 3.16: Bode diagram of the second order HPF

- The target of the second step is the elimination of the positive sequence current. This is achieved by moving first the input signal, which is given by equation 3.5, to the carrier negative reference frame. The output of this transformation is given by equation 3.6 where it can be seen that the positive sequence current presents now a pulsation of $2\omega_c$ while the negative sequence current has a pulsation of $h_r\vartheta_r$.

$$i_{qd_c}^{cn} = -jI_{cn}e^{j(h_r\vartheta_r)} - jI_{cp}e^{j2\omega_c t} \tag{3.6}$$

The signal given by equation 3.6 can be effectively filtered by a low pass filter LPF, its output being the negative sequence current containing the rotor position information. The negative sequence current in the carrier negative reference frame is given by equation 3.7.

$$i_{qd_{cn}}^{cn} = -jI_{cn}e^{jh_r\vartheta_r} \tag{3.7}$$

The second step is represented in the block diagram of figure 3.17, the corresponding FFTs also being shown in the figure.

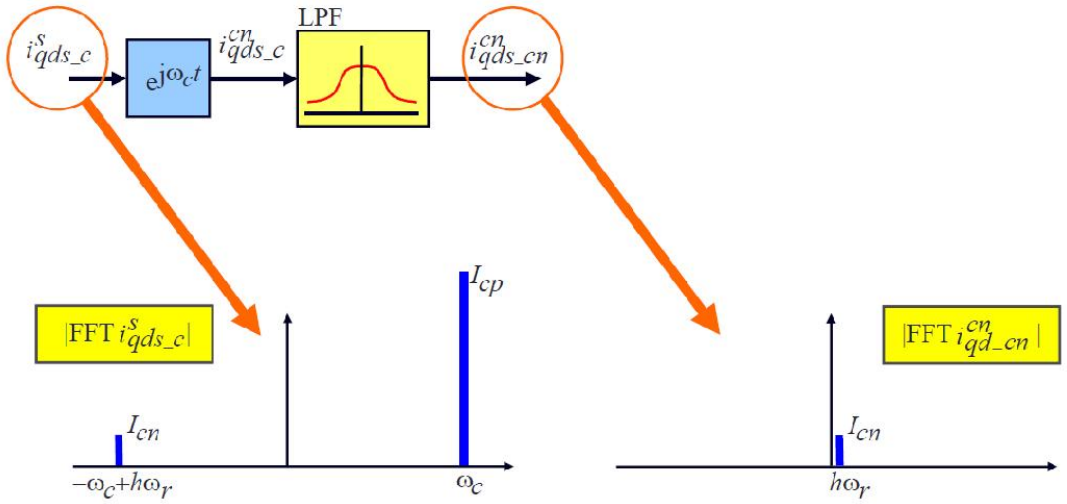

Figure 3.17: Block diagram of the second step of the signal processing [12]

For the simulation, a second order LPF with a cut off frequency f_{cut} of 500 Hz followed by a second order BSF at $2\omega_c$ and with a bandwidth of 100 Hz have been used. The BSF is particularly effective as it completely eliminates the positive sequence current while the LPF filters get rid of the remaining harmonics that could pass through the BSF. It is noted that the LPF produces a delay in the output signals which increase with the operating speed. For a rotor speed of 10 Hz (maximum speed at which the HFIST has to operate) the phase lag is around 10 deg.
Figures 3.18 and 3.19 show the Bode diagrams of the second order LPF and BSF respectively.

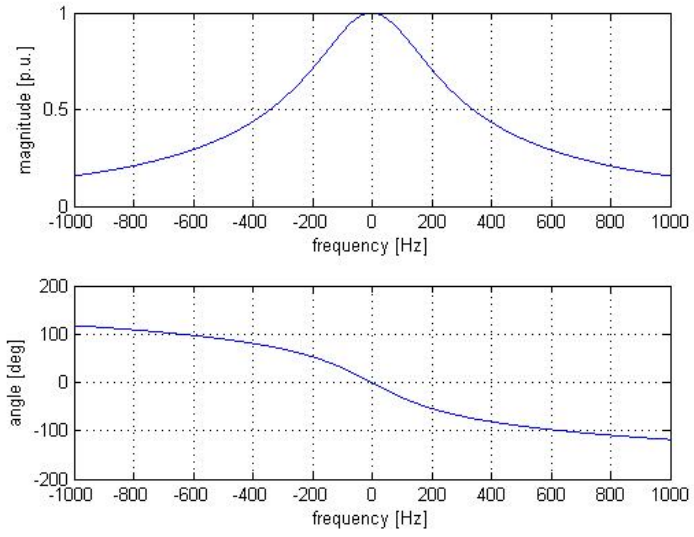

Figure 3.18: Bode diagram of the second order LPF

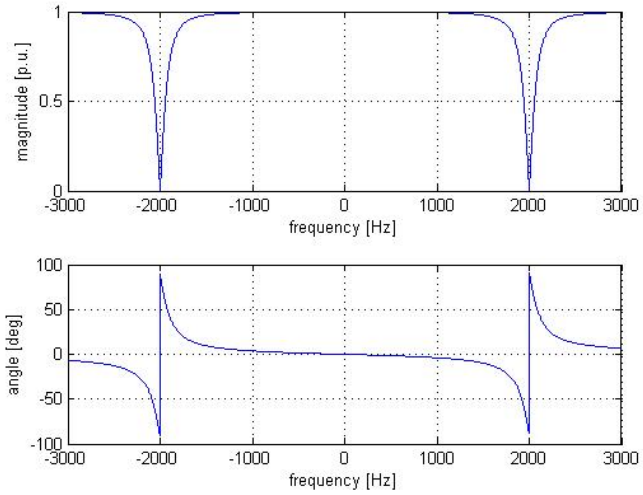

Figure 3.19: Bode diagram of the second order BSF

It is also useful to see the input and the output represented in a 3D chart, with the x and y axes consist in the complex plane while the third is time. In particular figure 3.20 represents $i^{s}_{qd_c}$, figure 3.21 represents $i^{cn}_{qd_c}$ and figure 3.22 represents $i^{cn}_{qd_{cn}}$.

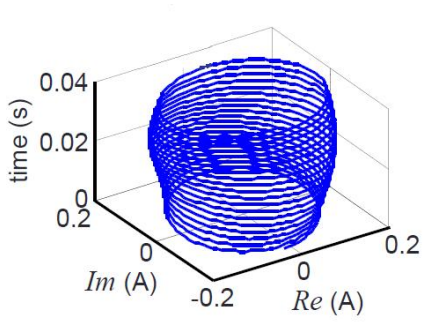

Figure 3.20: 3D representation of the input to the second step of the signal processing ($i^{s}_{qd_c}$) [12]

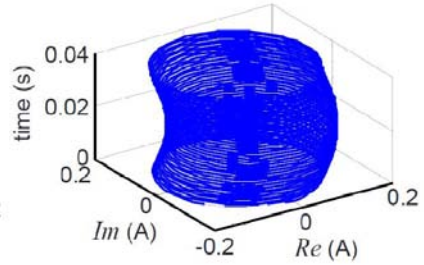

Figure 3.21: 3D representation of the input to the second step of the signal processing transformed in a -ω_c rotating reference frame ($i^{cn}_{qd_c}$) [12]

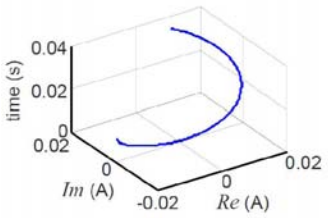

Figure 3.22: 3D representation of the output of the second step of the signal processing that represent the negative sequence current in the carrier negative reference frame ($i^{cn}_{qd_{cn}}$) [12]

An important aspect that has to be underline is that the pulsation of the negative sequence current in the carrier negative reference frame is not the fundamental pulsation as can be seen from equation 3.4 but it is the fundamental pulsation multiplied by h_r which is the harmonic order of the salience. In a IPMSM h_r is equal to 2 as the salience is given by the magnet which has a north and a south pole.
As mentioned in the introduction, the HFIST just provide the d-axis direction but not the orientation, hence an uncertain of 180 deg is present in the rotor position estimation. Several methods have been developed to detect the magnet polarity in a real drive, while at level of simulation the problem does not exist as the motor always starts with the d-axis at zero deg.
Finally the output of all this filtering processing becomes the input to a phase-lock loop (PLL) similar to the one used for the MBST presented in Chapter 2. In this case the output speed and rotor position has to be divided by two to account for the salience order. The speed provided by the PLL is then filtered to eliminate any ripple due to the not perfect wave form of the negative sequence current $i^{cn}_{qd_{cn}}$, before being feedback to the speed regulator. A second order LPF with a cut of frequency f_{cut} of 80 Hz was used for this purpose. Figure 3.23 shows the Bode diagram of the second order LPF.

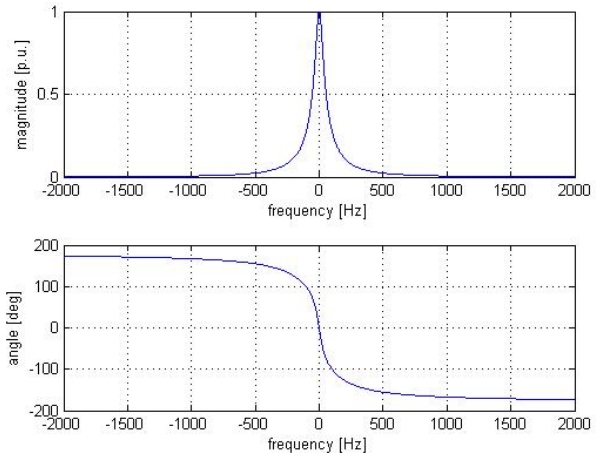

Figure 3.23: Bode diagram of the second order LPF used to filter the output of the PLL

3.3. Simulation Results for the HFIST

Simulation results shown the performance of the HFIST are provided in this section, two different operating speeds being used for this purpose:

- $\omega_{ref} = 5Hz$, which corresponds to half of the speed at which the control operates using the HFIST. In this simulation the motor is operating with no load;

- $\omega_{ref} = 10Hz$, which is the maximum speed at which the HFIST has to operate. For this simulation the load was set to $T = 10Nm$, which corresponds to approximately 1/5 of the nominal load. The same test was repeated with a negative reference speed of $\omega_{ref} = -10Hz$ and with a negative load of $T = -10Nm$;

Finally, the dynamic response of the HFIST will be evaluated by commanding a sudden change in the speed.

3.3.1. 5 Hz Operating Speed

This section shows the simulation results obtained commanding a reference speed ω_{ref} of 5 Hz with no load.

- Figure 3.24 shows the mechanical reference speed, the estimated speed and the speed measured by the encoder. The estimated speed presents, for a very short period of time, a negative peak which does not compromise the control of the motor. In fact, after a few ms, it becomes positive and it starts following the measured speed. It can also be observed that the estimated speed presents noise coming from the negative sequence current $i_{qd_{cn}}^{cn}$ (see figure 3.26), that affects the actual speed of the motor.

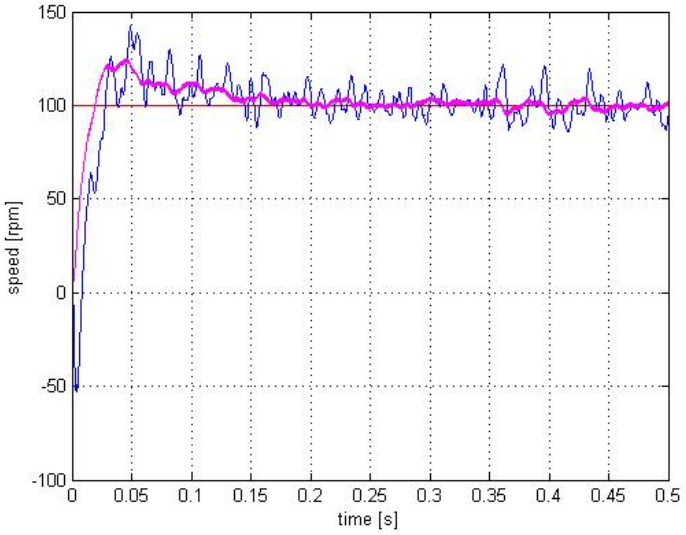

Figure 3.24: Reference speed (red), measured speed (blue), estimated speed (magenta) [rpm]

- Figure 3.25 shows the estimated mechanical angle and the mechanical angle measured by the encoder. A few radians delay between the estimated angle and the measured angle is observed, mainly due to the second order LPF.

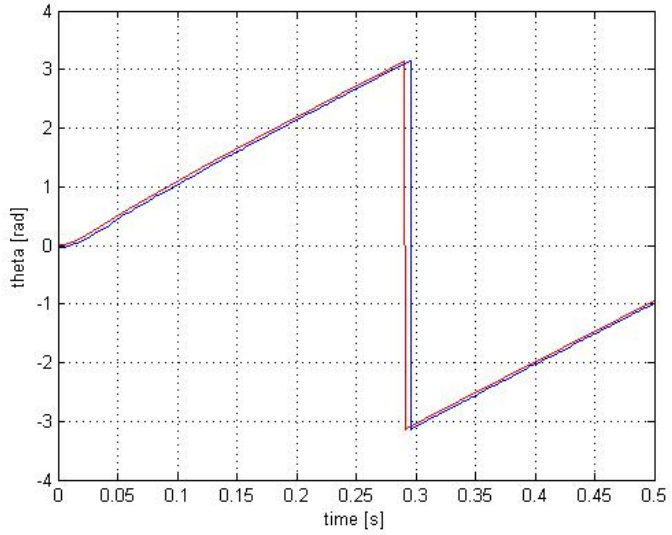

Figure 3.25: Measured angle (red) and estimated angle (blue) [rad]

- Figure 3.26 shows the d-axis and q-axis components of the negative sequence current $i^{cn}_{qd_{cn}}$. After a short period of time needed by the BSF to reach the steady state, the wave form of the two components $i^{cn}_{d_{cn}}$ and $i^{cn}_{q_{cn}}$ is quite clean and it presents a frequency of $2 \cdot 5Hz$ where 2 is the harmonic order

of the saliency for the IPMSM. The waves shapes present a ripple due to the non-perfect filtering of the fundamental current.

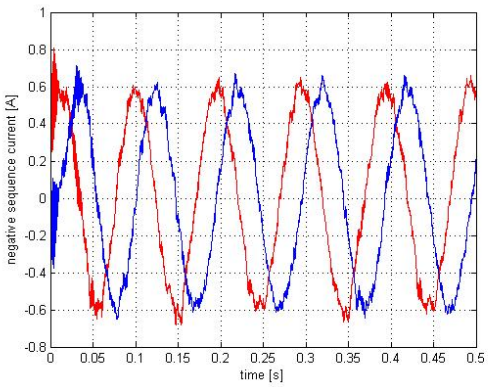

Figure 3.26: d (red) and q (blue) components of the negative sequence current $i_{qd_{cn}}^{cn}$

- Figure 3.27 shows the 3D chart with trajectory of the negative sequence current $i_{qd_{cn}}^{cn}$ showing only the last 0.2 s of the simulation. The trajectory of the negative sequence current $i_{qd_{cn}}^{cn}$ is better appreciated in the 3D chart.

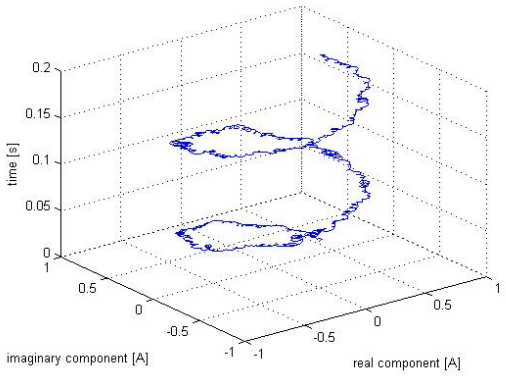

Figure 3.27: 3D chart with the trajectory of the negative sequence current $i_{qd_{cn}}^{cn}$

- Figure 3.28 shows the FFT of the measured current in the stationary reference frame (i_{qd}^{s}), of the output of the first step of the signal processing ($i_{qd_c}^{s}$) and of the final output of the signal processing ($i_{qd_{cn}}^{cn}$) considering only the last 0.2 s of the simulation. Figure 3.28 shows the FFT of the signals at the different steps of the signal processing used to isolate the negative sequence current $i_{qd_{cn}}^{cn}$.

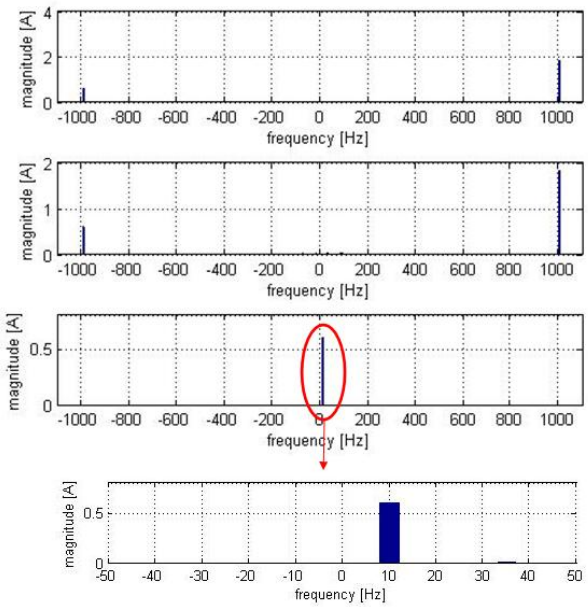

Figure 3.28: Top chart: FFT of the measured current in the stationary reference frame (i^s_{qd}), cetral chart FFT of the output of the first step of the signal processing ($i^s_{qd_c}$). Bottom chart: FFT of the final output of the signal processing ($i^{cn}_{qd_{cn}}$) with zoom at low frequency

- Figure 3.29 shows the 3-phase inverter reference voltage with a zoom for the high frequency injected voltage superimposed to the fundamental one. It can be clearly seen the fundamental voltage to which is superimposed the high frequency voltage, showed in a zoom representation in the lower part of figure 3.29.

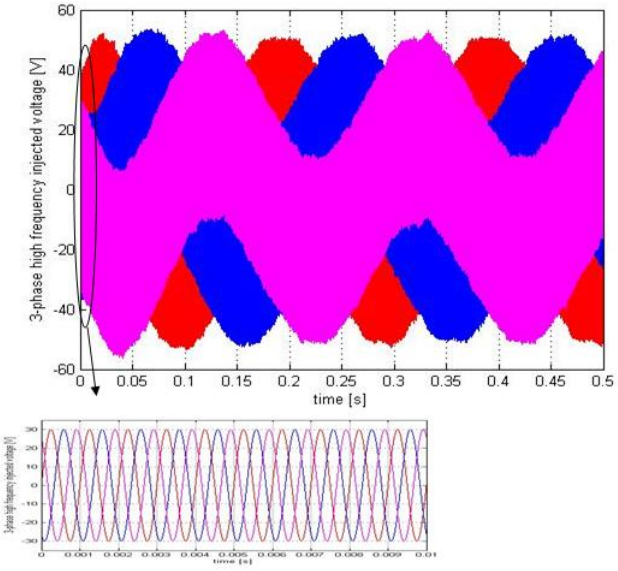

Figure 3.29: 3-phase inverter reference voltage with zoom for the high frequency injected voltage superimposed to the fundamental one

3.3.2. 10 Hz operating speed with 10 Nm Load

In this simulation a 10 Nm load was applied to the machine. It is noted that due to the simulation time limit (0.5s), with larger loads the motor cannot reach steady state in the simulation time.
The results that has been shown are the followings:

- Figure 3.30 shows the mechanical reference speed, the estimated speed and the speed measured by the encoder.

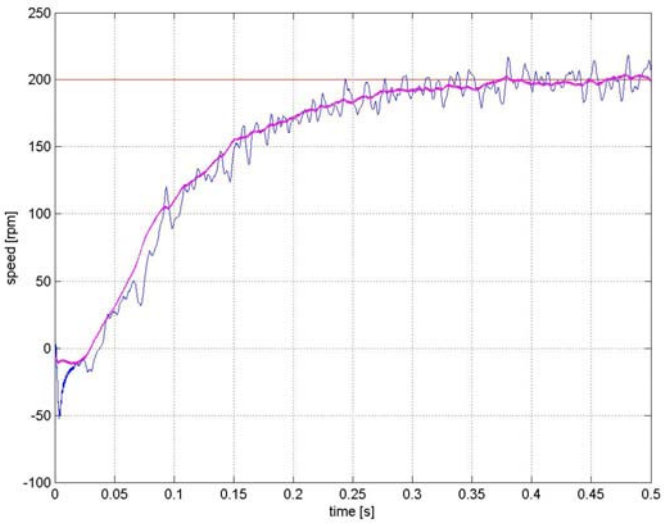

Figure 3.30: Reference speed (red), measured speed (blue), estimated speed (magenta) [rpm]

- Figure 3.31 shows the estimated mechanical angle and the mechanical angle measured by the encoder.

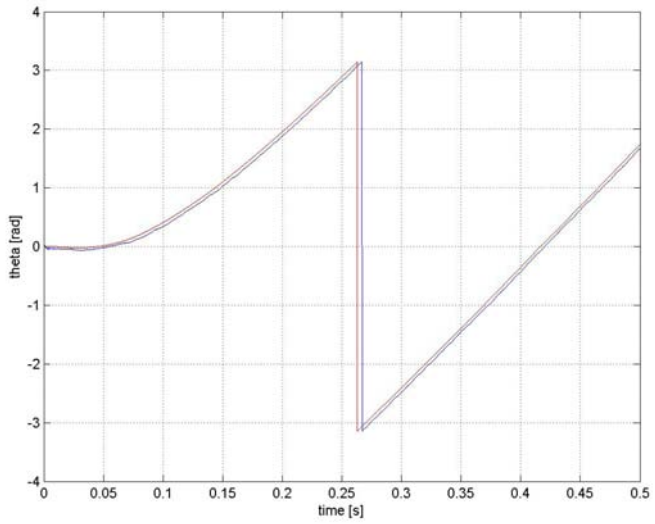

Figure 3.31: Measured angle (red) and estimated angle (blue) [rad]

- Figure 3.32 shows the d-axis and q-axis components of the negative sequence current $i_{qd_{cn}}^{cn}$. The delay between measured and estimated angle is greater than for the previous simulation due to the speed increase from 5 Hz to 10Hz.

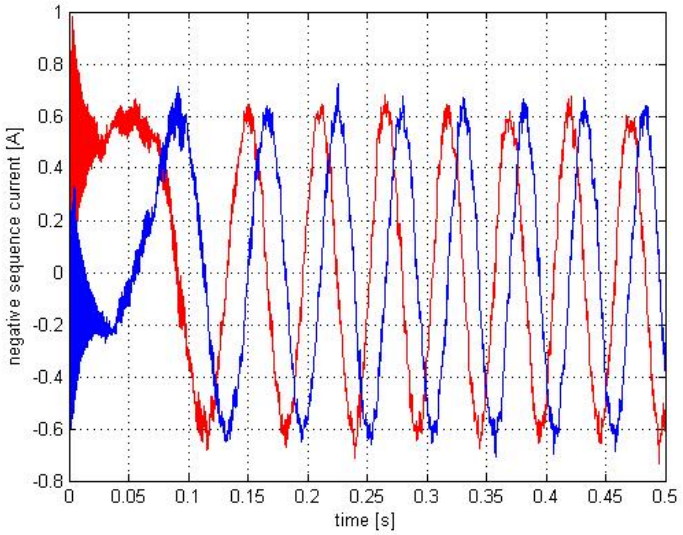

Figure 3.32: d (red) and q (blue) components of the negative sequence current $i_{qd_{cn}}^{cn}$

- Figure 3.33 shows the 3D chart with trajectory of the negative sequence current $i_{qd_{cn}}^{cn}$ considering only the last 0.2 s of the simulation.

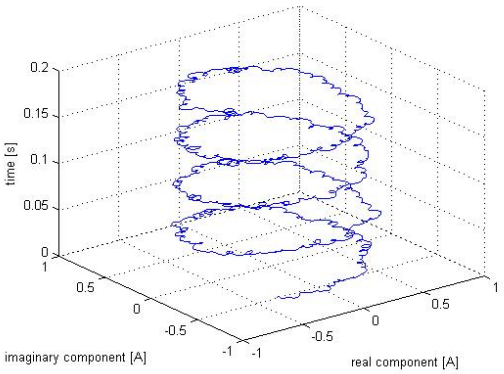

Figure 3.33: 3D chart with the trajectory of the negative sequence current $i^{cn}_{qd_{cn}}$

- Figure 3.34 shows the FFT of the current in the stationary reference frame (i^{s}_{qd}) at the output of the first step of the signal processing ($i^{s}_{qd_c}$) and of the final output of the signal processing ($i^{cn}_{qd_{cn}}$) considering only the last 0.2 s of the simulation.

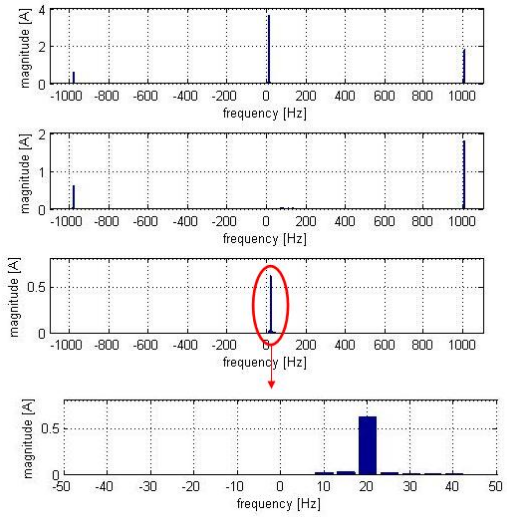

Figure 3.34: Top chart FFT of the measured current in the stationary reference frame (i^{s}_{qd}), cetral chart FFT of the output of the first step of the signal processing ($i^{s}_{qd_c}$) and bottom chart FFT of the final output of the signal processing ($i^{cn}_{qd_{cn}}$) with zoom at low frequency

- Figure 3.35 shows the 3-phase inverter reference voltage.

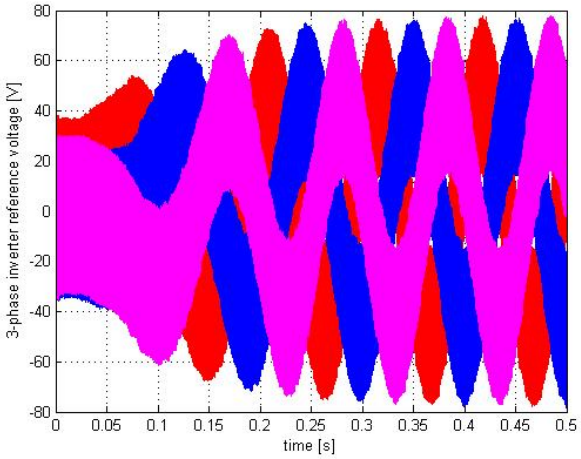

Figure 3.35: 3-phase inverter reference voltage

- Figure 3.36 shows the torque output of the speed regulator. The torque presents noise due to the estimated speed feedback and it is then responsible for the smother noise in the actual speed.

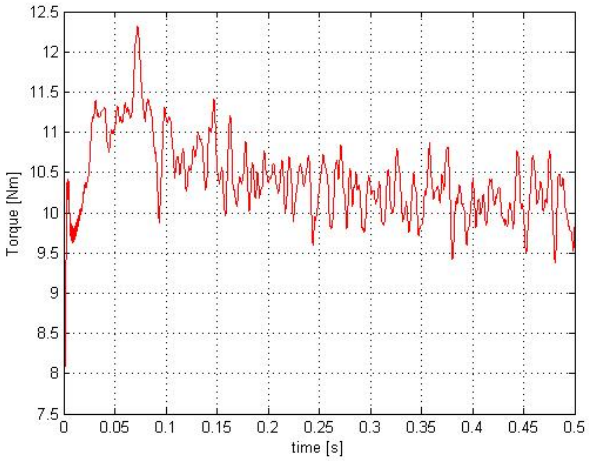

Figure 3.36: torque output of the speed regulator [Nm]

3.3.3. -10 Hz Operating Speed with -10 Nm Load

The target of this simulation is to verify the symmetric operation between negative and positive operating speeds. While for the MBST the symmetry between positive and negative speed is perfect, for the HFIST there is a little asymmetry as the spectra separation between the negative sequence current and the fundamental currents is different for positive speeds and for negative speeds. The simulation results are organized similar to the previous sections:

- Figure 3.37 shows the mechanical reference speed, the estimated speed and the speed measured by the encoder.

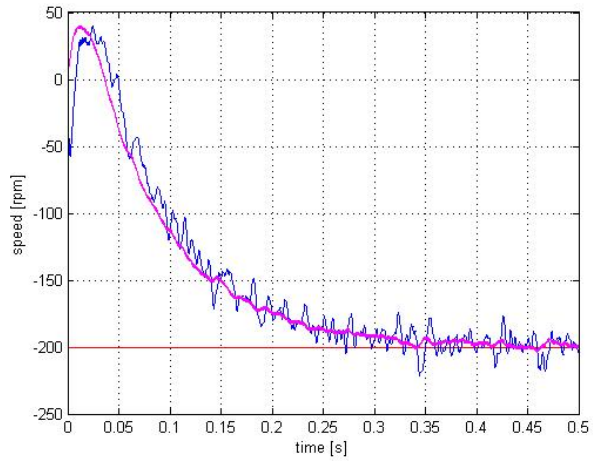

Figure 3.37: Reference speed (red), measured speed (blue), estimated speed (magenta) [rpm]

- Figure 3.38 shows the estimated mechanical angle and the mechanical angle measured by the encoder. The delay between the measured angle and the estimated angle for negative speed is smaller than the delay for positive speed as the negative sequence current superimposed to the fundamental current presents a different frequency for the two operating speed, i.e. -1020 and -980 respectively for a reference speed of -10 Hz and +10 Hz. The fundamental current controller behaves slightly different in both cases therefore. Hence the voltage output of the current controller presents, for negative speed, a smaller unwanted component that can interferes with the high frequency injected voltage slightly effecting the estimated angle. As for the positive sequence current, it is perfectly filtered by the BSF placed in the feedback of the current controller.

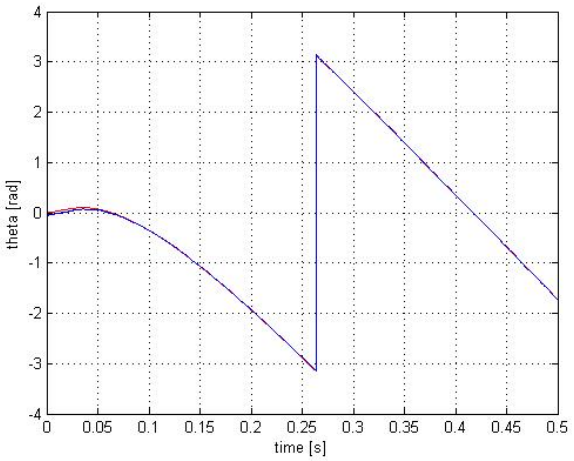

Figure 3.38: Measured angle (red) and estimated angle (blue) [rad]

- Figure 3.39 shows the d-axis and q-axis components of the negative sequence

current $i^{cn}_{qd_{cn}}$.

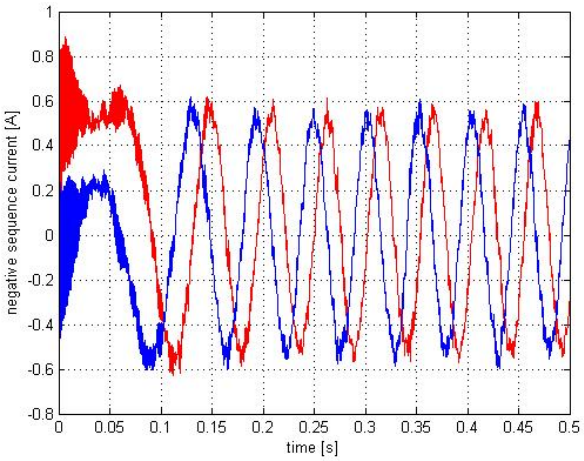

Figure 3.39: d (red) and q (blue) components of the negative sequence current $i^{cn}_{qd_{cn}}$

- Figure 3.40 shows the 3D chart with trajectory of the negative sequence current $i^{cn}_{qd_{cn}}$ considering only the last 0.2 s of the simulation.

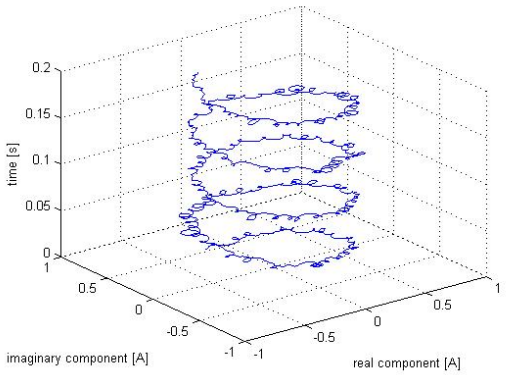

Figure 3.40: 3D chart with the trajectory of the negative sequence current $i^{cn}_{qd_{cn}}$

- Figure 3.41 shows the FFT of the measured current in the stationary reference frame (i^{s}_{qd}), at the output of the first step of the signal processing ($i^{s}_{qd_c}$) and of the final stage of the signal processing ($i^{cn}_{qd_{cn}}$), considering only the last 0.2 s of the simulation.

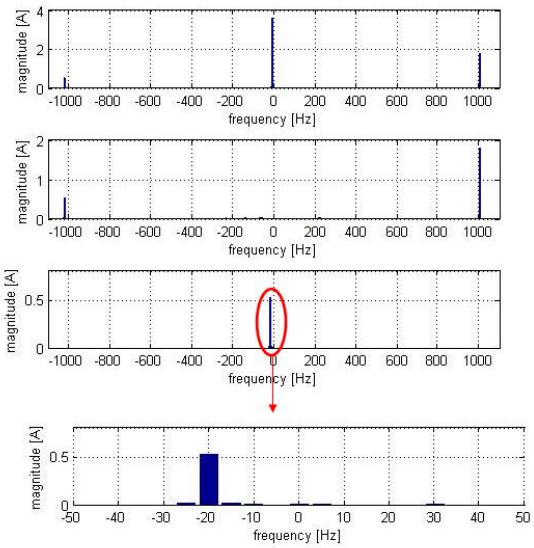

Figure 3.41: top chart FFT of the measured current in the stationary reference frame (i^s_{qd}), cetral chart FFT of the output of the first step of the signal processing ($i^s_{qd_c}$) and bottom chart FFT of the final output of the signal processing ($i^{cn}_{qd_{cn}}$) with zoom at low frequency

- Figure 3.42 shows the 3-phase inverter reference voltage.

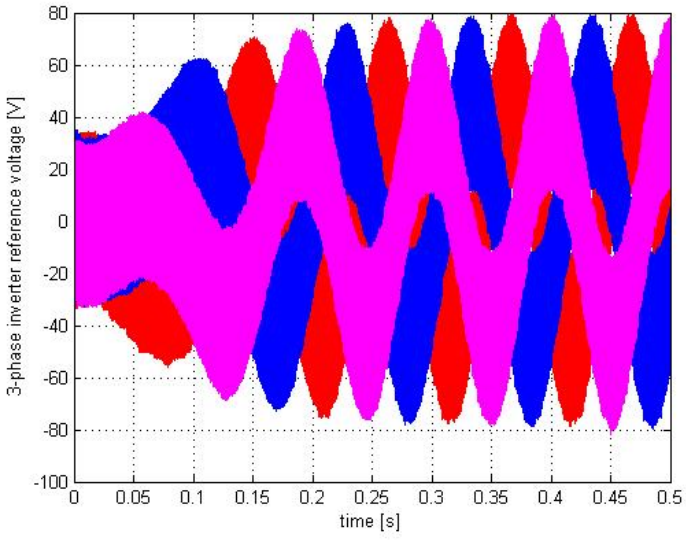

Figure 3.42: 3-phase inverter reference voltage

- Figure 3.43 shows the torque commanded by the speed regulator.

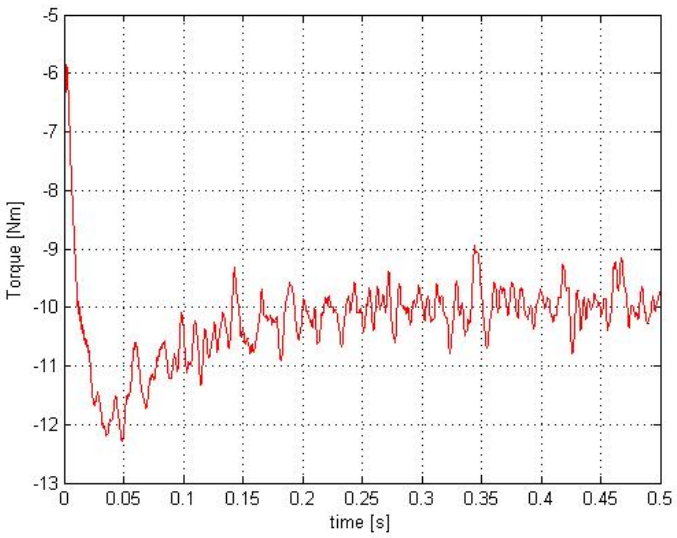

Figure 3.43: Torque commanded by the speed regulator [Nm]

3.3.4. Multiple Operating Speeds

This simulation illustrates the dynamic response of the HFIST. The reference speed takes four different values: 0, 10 Hz, -10 Hz and -5 Hz.
The results presented are the following:

- Figure 3.44 shows the mechanical reference speed, the estimated speed and the speed measured by the encoder. The speed controller employing the HFIST also present a quite fast dynamic as the delay between reference speed and estimated speed does not exceed 20 ms.

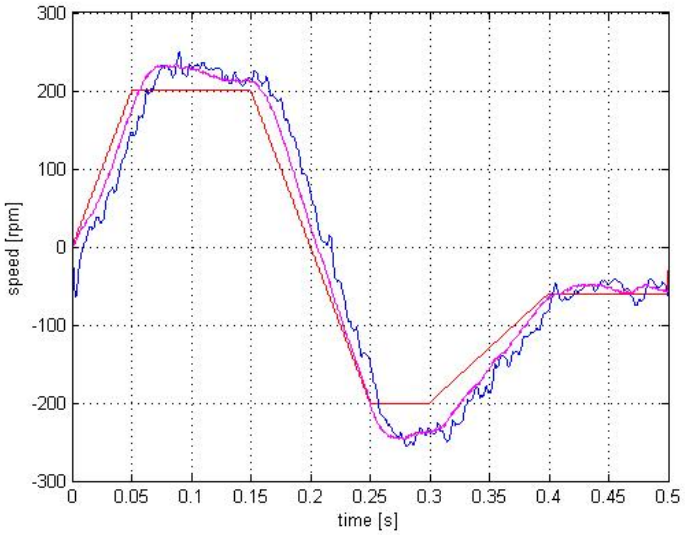

Figure 3.44: Reference speed (red), measured speed (blue), estimated speed (magenta) [rpm]

- Figure 3.45 shows the estimated mechanical angle and the mechanical angle measured by the encoder.

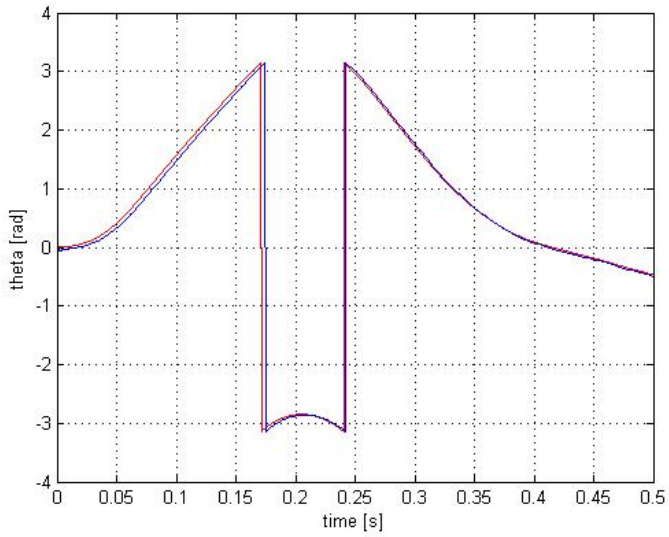

Figure 3.45: Measured angle (red) and estimated angle (blue) [rad]

- Figure 3.46 shows the d-axis and q-axis components of the negative sequence current $i_{qd_{cn}}^{cn}$.

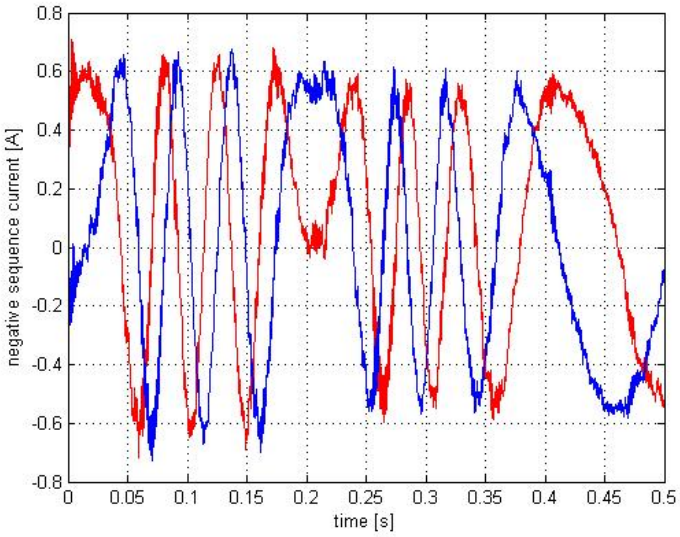

Figure 3.46: d (red) and q (blue) components of the negative sequence current $i_{qd_{cn}}^{cn}$

- Figure 3.47 shows the 3-phase inverter reference voltage.

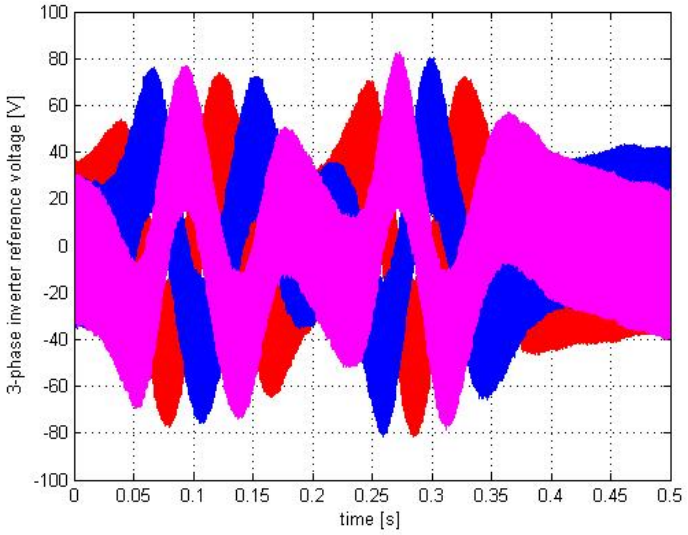

Figure 3.47: 3-phase inverter reference voltage

3.3.5. Position Control

Once the speed control, employing the HFIST, is working correctly, it is very easy to implement also the sensorless position control of the motor. Hence a position control P regulator has been placed in series with the speed control PI regulator with 4 being the value of the proportional gain $k_{p\vartheta}$.
The following simulations are shown, where the reference angle are in mechanical units:

- $\vartheta_{ref} = 45deg$. In this simulation the motor is operating with no load;
- $\vartheta_{ref} = 120deg$. In this simulation the motor is operating with no load;
- $\vartheta_{ref} = 180deg$. In this simulation the motor is operating with a load of 20 Nm.

Finally, the dynamic response of the sensorless position control will be evaluated by commanding sudden changes in the reference angle ϑ_{ref}.

45 deg Reference Angle

This subsection shows the simulation results obtained commanding a reference angle ϑ_{ref} of 45 deg with no load. In particular it is shown:

- Figure 3.48 shows the mechanical reference speed (output of the position regulator), the estimated speed and the speed measured by the encoder.

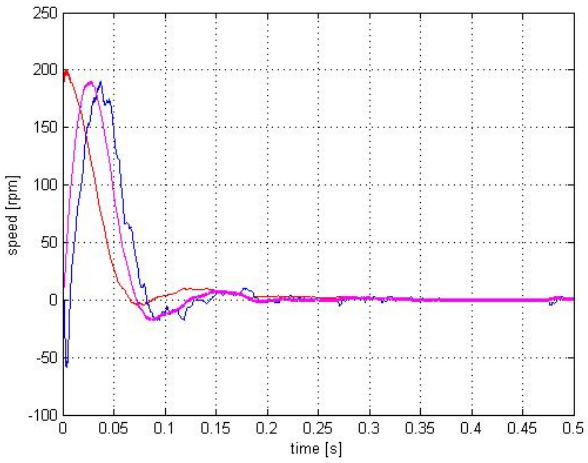

Figure 3.48: Reference speed (red), measured speed (blue), estimated speed (magenta) [rpm]

- Figure 3.49 shows the reference angle, the estimated mechanical angle and the mechanical angle measured by the encoder. At zero speed, when the position angle reaches its steady state value, a little error still exist between measured and estimated angle. It is due only to the dead time of the inverter and not to the filters as the frequency of the negative sequence current $i_{qd_{cn}}^{cn}$ is equal to zero (see figure 3.50).

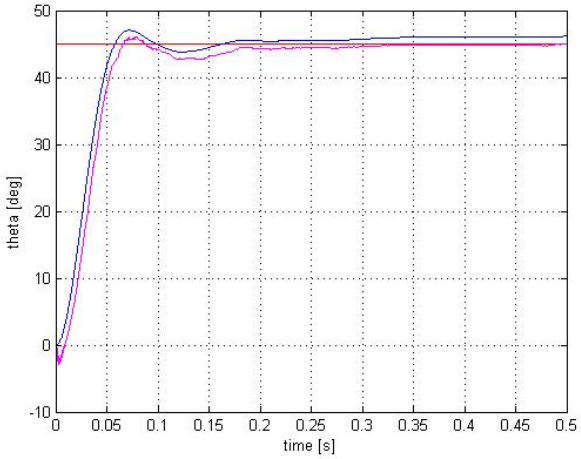

Figure 3.49: Reference angle (red), measured angle (blue) and estimated angle (magenta) [deg]

- Figure 3.50 shows the d-axis and q-axis components of the negative sequence current $i^{cn}_{qd_{cn}}$.

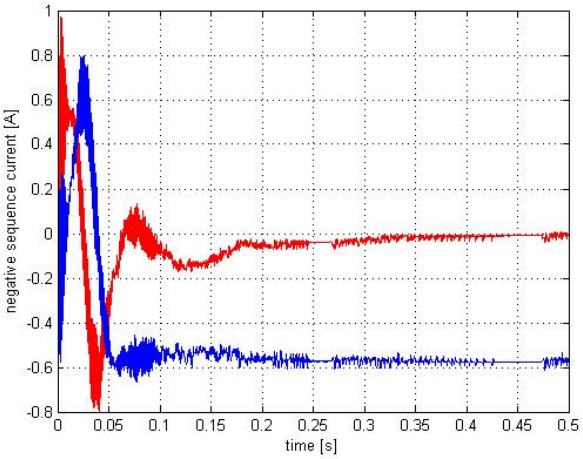

Figure 3.50: d (red) and q (blue) components of the negative sequence current $i^{cn}_{qd_{cn}}$

120 deg Reference Angle

This section shows the simulation results obtained commanding a reference angle ϑ_{ref} of 120 deg with no load. In particular it is shown:

- Figure 3.51 shows the mechanical reference speed, the estimated speed and the speed measured by the encoder.

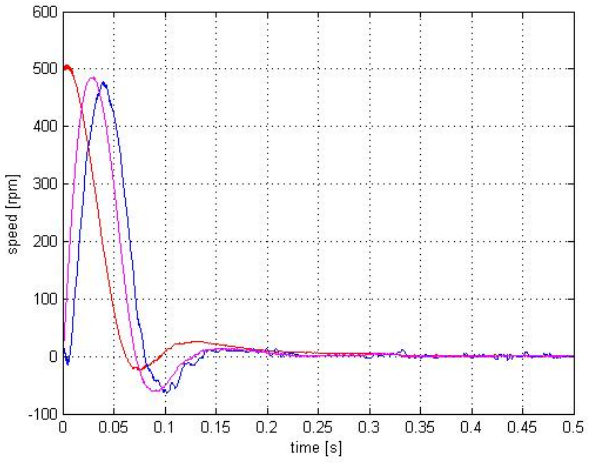

Figure 3.51: Reference speed (red), measured speed (blue), estimated speed (magenta) [rpm]

- Figure 3.52 shows the estimated mechanical angle and the mechanical angle measured by the encoder.

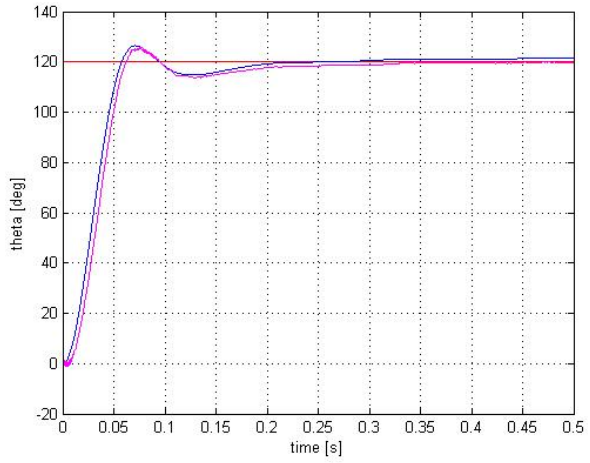

Figure 3.52: Reference angle (red), measured angle (blue) and estimated angle (magenta) [deg]

- Figure 3.53 shows the d-axis and q-axis components of the negative sequence current $i_{qd_{cn}}^{cn}$.

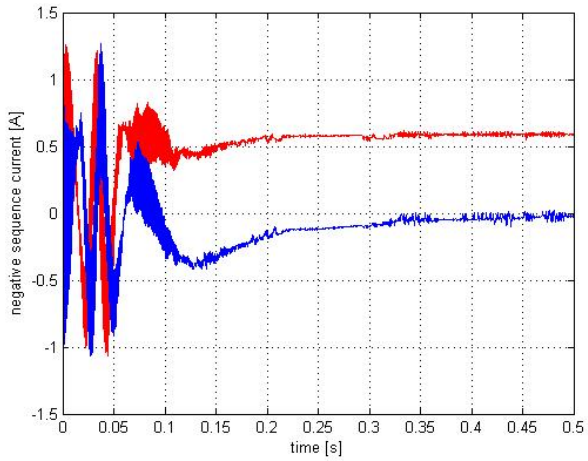

Figure 3.53: d (red) and q (blue) components of the negative sequence current $i_{qd_{cn}}^{cn}$

180 deg Reference Angle with 20 Nm Load

This section shows the simulation results obtained commanding a reference angle ϑ_{ref} of 180 deg with a load of 20 Nm. In particular it is shown:

- Figure 3.54 shows the mechanical reference speed, the estimated speed and the speed measured by the encoder.

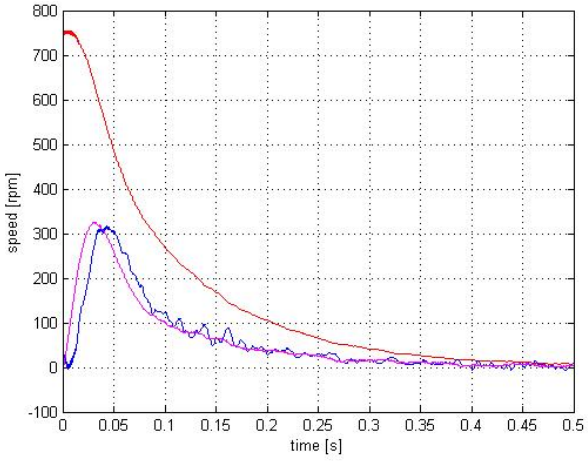

Figure 3.54: Reference speed (red), measured speed (blue), estimated speed (magenta) [rpm]

- Figure 3.55 shows the estimated mechanical angle and the mechanical angle measured by the encoder.

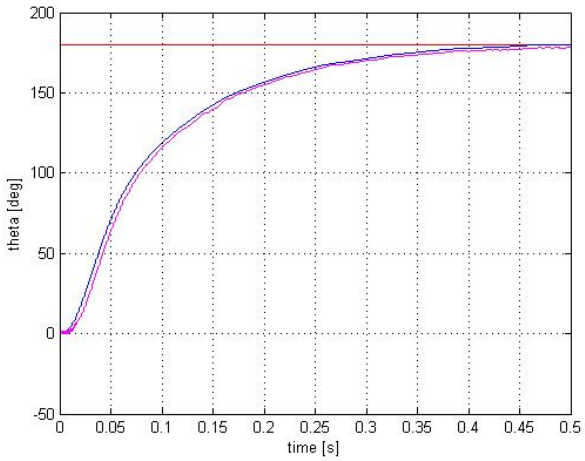

Figure 3.55: Reference angle (red), measured angle (blue) and estimated angle (magenta) [deg]

- Figure 3.56 shows the d-axis and q-axis components of the negative sequence current $i_{qd_{cn}}^{cn}$.

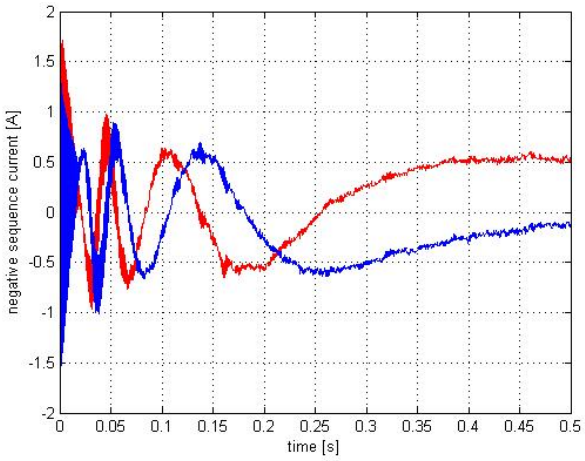

Figure 3.56: d (red) and q (blue) components of the negative sequence current $i_{qd_{cn}}^{cn}$

- Figure 3.57 shows the torque output of the speed regulator.

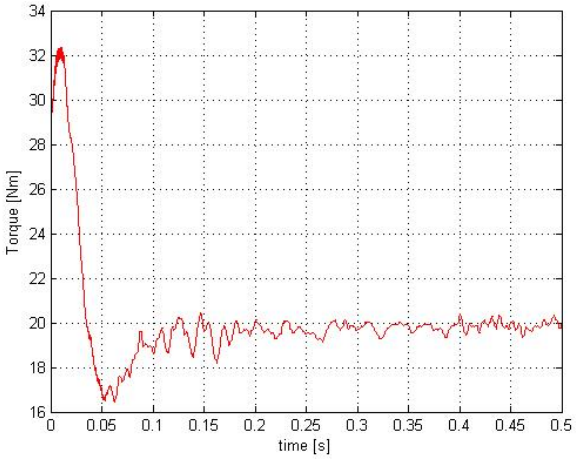

Figure 3.57: torque output of the speed regulator [Nm]

Position Control with Successive Changes in the Reference Position

This simulation illustrates the dynamics of the position control using the HFIST. The reference angle ω_{ref} changes among four different values: 0 deg, 30 deg, 90 deg and 45 deg. The simulation results are the following:

- Figure 3.58 shows the mechanical reference speed, the estimated speed and the speed measured by the encoder.

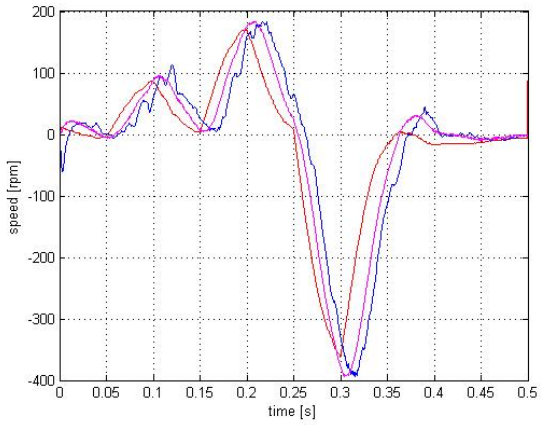

Figure 3.58: Reference speed (red), measured speed (blue), estimated speed (magenta) [rpm]

- Figure 3.59 shows the estimated mechanical angle and the mechanical angle measured by the encoder.

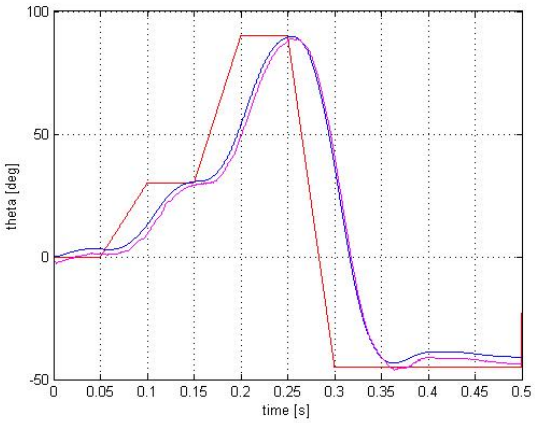

Figure 3.59: Reference angle (red), measured angle (blue) and estimated angle (magenta) [deg]

- Figure 3.60 shows the d-axis and q-axis components of the negative sequence current $i_{qd_{cn}}^{cn}$.

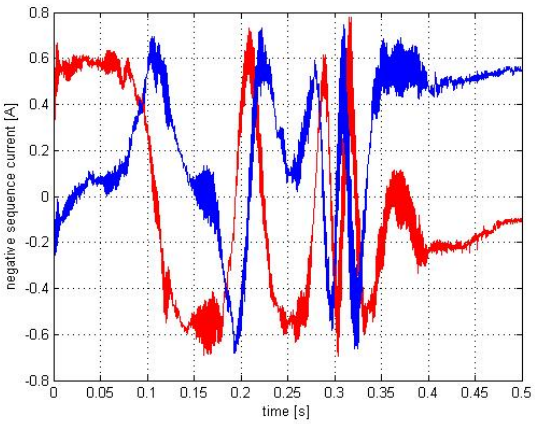

Figure 3.60: d (red) and q (blue) components of the negative sequence current $i_{qd_{cn}}^{cn}$

3.4. Conclusions

In this chapter, the HFSIT have been implemented employing a high frequency rotating carrier voltage vector.
As the results of the simulation show, the sensorless control of the IPMSM employing the MBST behaves definitely better compared to the HFIST. This is due to the completely different signal processing that the methods use to obtain the quantity that provides the rotor position and speed information. In fact as regards the MBST, it is sufficient to solve an equation to estimate the extended flux while for the HFIST the signal processing involves coordinate transformations and filters which at the end strongly effects the output signal.

However MBST can not operate at very low speed and consequently does not allow position control of the motor, hence the HFIST is essential for this purposes.

CHAPTER 4

HYBRID SENSORLESS TECHNIQUE

4.1. Introduction

This chapter presents and discusses the simulations of the hybrid technique combining the MBST with the HFIST. MBST and HFIST alone cannot be used in the whole speed range due to several reasons. Considering first the MBST employed for medium and high operating speeds the main reasons that make it fail at low speed are the followings:

- The back-EMF which is the estimated quantity on which this methods relay linearly depends on the rotor angular speed, hence intrinsically fails at zero speed as the value of the back-EMF is zero. Also, it cannot be used for position control;
- The measurements and the parameter estimation have to be very precise, nevertheless even small errors are always present and this involves that MBST also fail at low speed since the signal-to-noise ratio decreases and the parameter errors and the inverter nonlinearities increase their effects;
- Another reason that impedes to employ MBST for very low speed is that to get the flux of the magnets an integral operation is always needed. But in a practical implementation a pure integrator cannot be used, hence it is replaced by a low pass filter. The condition for which the pure integrator and low pass filter have the same frequency response is that the pulsation of the input signal as to be greater than the cut off frequency. For this reason the motor cannot operate below a certain speed given by the cut off frequency of the filter.

As far as the HFIST is regard the reasons that impede its use at high speed can be summarized as follows:

- The voltage signal injection introduce extra losses, torque ripple and acoustic noise because of the non-perfect sinusoidal wave form of the negative sequence current $i_{qd_{cn}}^{cn}$ at the end of the signal processing, of the coupling effects of the fundamental current transients, of inverter nonlinearity so it is used when it is strictly necessary;

- At high speed, when the voltage is already high, it could occur that the injected signal-voltage overcomes the limit given by the DC bus;

- Furthermore the difficulty in extracting the high frequency current component from the ac phase current increases with the speed.

It is now clear why the two sensorless methods have to be used in the respective operative conditions whereby the hybrid methods have been introduced.
In the last section of Chapter 1 a bibliographic research has been presented where the state of art of this innovative technology has been introduced. In this regards six different solutions proposed by researchers from different universities to operate in the whole speed range have been analyzed. A hybrid technique using a linear combination of the position error signals from both HFIST and MBST, instead of velocity or the position, has been chosen as starting point.
The motor parameters, the gains of the speed and current PI regulators and all the aspects related to the algorithm control of the electric drive were presented in the introduction of Chapter 2.

4.2. Implementation of the Hybrid Method

The selected hybrid method uses a weighted average of the position error signals coming from the MBST and HFIST. This linear combination results in a transition zone bounded by a lower ω_{min} and an upper ω_{max} transition speeds. Hence, the control of the motor for zero and low speed relays only on the HFIST until the estimated speed $\tilde{\omega}$ reaches the lower limit speed ω_{min}. Then the position error signal ϵ input of the PLL is obtained as the weighted average between the position error signals from both the MBST and the HFIST. When the estimated speed $\tilde{\omega}$ reaches the value of the upper limit speed ω_{max} the position error signal ϵ input of the PLL coincides with the one coming from the MBST. This technique can be summarized in the following scheme:

- for $|\tilde{\omega}| \leq \omega_{min}$

$$\epsilon = \epsilon^{HFIST}$$

- for $\omega_{min} < |\tilde{\omega}| < \omega_{max}$

$$\epsilon = \frac{\omega_{max} - |\tilde{\omega}|}{\omega_{max} - \omega_{min}} \epsilon^{HFIST} + \frac{|\tilde{\omega}| - \omega_{min}}{\omega_{max} - \omega_{min}} \epsilon^{MBST}$$

- for $|\tilde{\omega}| \geq \omega_{max}$

$$\epsilon = \epsilon^{MBST}$$

Figure 4.1 shows the Simulink block diagram used for the implementation of this hybrid strategy.

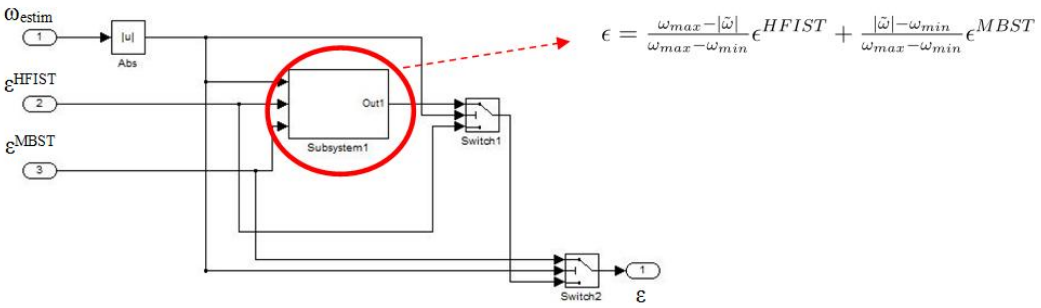

Figure 4.1: Block diagram of the implemented hybrid technique

In figure 4.1 it can be observed that the absolute value of the estimated speed $\tilde{\omega}$ is used as input of the system and compared with ω_{min} and ω_{max} in the blocks 'Switch1' and 'Switch2' respectively. If $\tilde{\omega} \leq \omega_{min}$ the output of block 'Switch1' is ϵ^{HFIST} while on the contrary if $\tilde{\omega} \geq \omega_{min}$ the output of block 'Switch1' is the output of 'Subsystem1' which correspond to the combination of position error signals from both HFIST and MBST. Then, the output of 'Switch1' becomes one of the input of 'Switch2' while the others are $|\tilde{\omega}|$ and ϵ^{MBST}. Hence, in this block, $|\tilde{\omega}|$ is compared with ω_{max} determining the switch from MBST operating mode and, depending on the output of 'Switch1', HFIST or Hybrid operating mode.

The high frequency injection of the signal-voltage contribute to extra losses and to torque ripple and acoustic noise in the normal operating conditions. Therefore it is important to disconnect it whenever it is not needed. Hence the high frequency injection of the signal-voltage is disconnected at a speed $\omega_{inj_{min}}$ slightly higher than the upper limit speed ω_{max} while it is reconnected at a speed $\omega_{inj_{max}}$ much higher than ω_{max} in order to give the necessary time to the HFIST to provide a stable estimation before reaching the transition zone. The derivative of the reference speed ω_{ref} has been used for this purpose. If the derivative of ω_{ref} is greater than zero (positive acceleration) the injection is switched off when the estimated speed $\tilde{\omega}$ reaches $\omega_{inj_{min}}$ while if the derivative of the reference speed ω_{ref} is equal or lower than zero (negative acceleration or constant speed) the injection is switched on at $\omega_{inj_{max}}$.
The presented strategy has to work also for negative operating speeds. Hence, if the estimated speed $\tilde{\omega}$ is greater then zero the high frequency signal-voltage injection is regulated with the strategy that has just been described, while if $\tilde{\omega}$ is negative the control strategy is specular. In fact, the injection is switched off

when the magnitude of the estimated speed $|\tilde{\omega}|$ reaches $\omega_{inj_{min}}$ if the derivate of ω_{ref} is lower than zero while it is switched on when $|\tilde{\omega}|$ reaches the value $\omega_{inj_{max}}$ if the derivative of ω_{ref} is equal or greater than zero.
The presented strategy has been implemented in Simulink using the block diagrams shown in figure 4.2, it can be summarized by the following scheme:

- for $|\tilde{\omega}| > 0$
  - when $|\tilde{\omega}| < \omega_{inj_{min}}$;

$$v^s_{qd_c} = V_c e^{j(\omega_c t)}$$

  - when $\omega_{inj_{max}} > |\tilde{\omega}| > \omega_{inj_{min}}$ and $\frac{d\omega_{ref}}{dt} > 0$;

$$v^s_{qd_c} = 0$$

  - when $\omega_{inj_{max}} > |\tilde{\omega}| > \omega_{inj_{min}}$ and $\frac{d\omega_{ref}}{dt} \leq 0$;

$$v^s_{qd_c} = V_c e^{j(\omega_c t)}$$

  - when $|\tilde{\omega}| > \omega_{inj_{max}}$;

$$v^s_{qd_c} = 0$$

- for $|\tilde{\omega}| < 0$
  - when $|\tilde{\omega}| < \omega_{inj_{min}}$;

$$v^s_{qd_c} = V_c e^{j(\omega_c t)}$$

  - when $\omega_{inj_{max}} > |\tilde{\omega}| > \omega_{inj_{min}}$ and $\frac{d\omega_{ref}}{dt} < 0$;

$$v^s_{qd_c} = 0$$

  - when $\omega_{inj_{max}} > |\tilde{\omega}| > \omega_{inj_{min}}$ and $\frac{d\omega_{ref}}{dt} \geq 0$;

$$v^s_{qd_c} = V_c e^{j(\omega_c t)}$$

  - when $|\tilde{\omega}| > \omega_{inj_{max}}$;

$$v^s_{qd_c} = 0$$

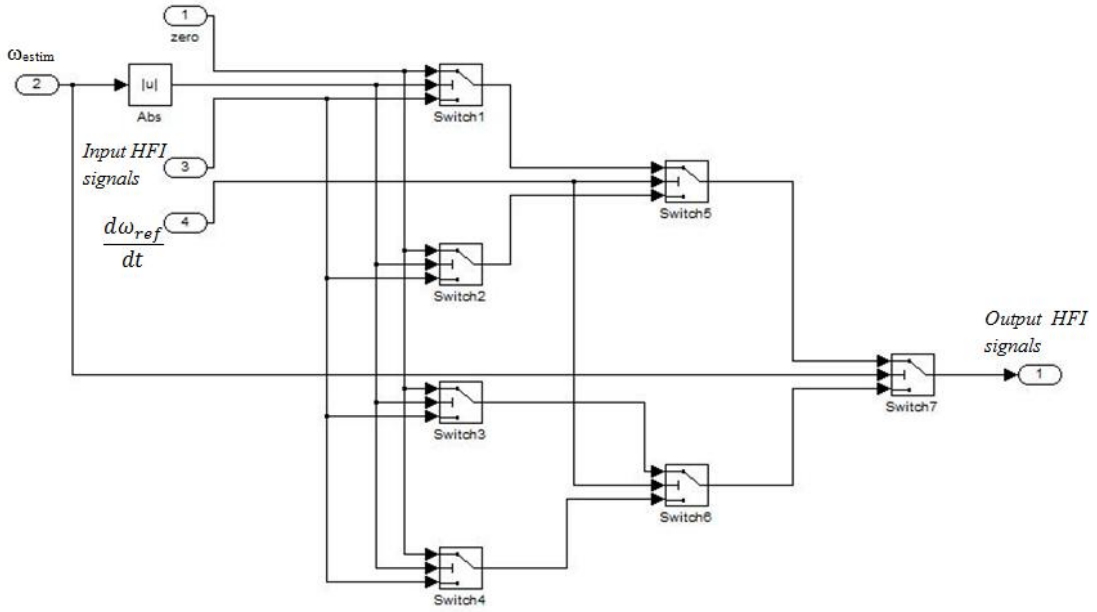

Figure 4.2: Block diagram of the implementation of the injection strategy

As it is showed in figure 4.2, the system presents four inputs: a 'zero-constant signal', the absolute value of the estimated speed $|\tilde{\omega}|$, the 'Input HFI-signals' which is the set of high frequency three-phase voltages in equation 3.2 and the derivative of the reference speed ω_{ref}. The output of the block diagram is the high frequency excitation that will be eventually superimposed to the fundamental excitation that has to feed the motor as showed in figure 3.1. In blocks 'Switch1' and 'Switch2' $|\tilde{\omega}|$ is compared with $\omega_{inj_{min}}$ and $\omega_{inj_{max}}$ respectively, the result of this comparison determines the switching between the injection of the 'zero-constant signal' and the injection of 'Input HFI-signals' and viceversa. Then, 'Switch5' is employed to select the output of 'Switch1' rather then 'Switch2', its output depending on the sign of the derivative of ω_{ref}. Finally, block 'Switch7', depending on the sign of $\tilde{\omega}$, has the task of switching from the upper part of the block diagram (used for positive speed) to the lower part (used for negative speed) where blocks 'Switch3', 'Switch4' and 'Switch6' are employed and which are specular image of each the other.
In the following table the values of the parameters mentioned so far are reported.

Parameter	**Values [Hz]**
ω_{min}	8
ω_{max}	10
$\omega_{inj_{min}}$	11
$\omega_{inj_{max}}$	20

4.3. Simulation Results for the Hybrid Technique

Simulation results of the hybrid technique are provided in this section, three different configurations of reference speeds being used for this purpose:

- ω_{ref} taking the following values: 0 Hz, 50 Hz, 5 Hz. In this simulation the motor is operating with a load of 10 Nm;
- ω_{ref} taking the following values: 0 Hz, 30 Hz, -30 Hz. In this simulation the motor is operating with zero load;
- ω_{ref} taking the following values: 0 Hz, 70 Hz, 9 Hz. In this simulation the motor is operating with zero load;

4.3.1. 0 Hz, 50 Hz and 5 Hz Operating Speed with 10 Nm Load

The simulation results shown in the figures are briefly described followings:

- Figure 4.3 shows the mechanical reference speed, the estimated speed and the speed measured by the encoder. During speed up the transition zone is crossed almost without any perturbation in both estimated and actual speed, while, when it is crossed again during the deceleration the motor, a small perturbation appears in the estimated speed but thanks to the inertia of the machine it does not affect to the actual speed.

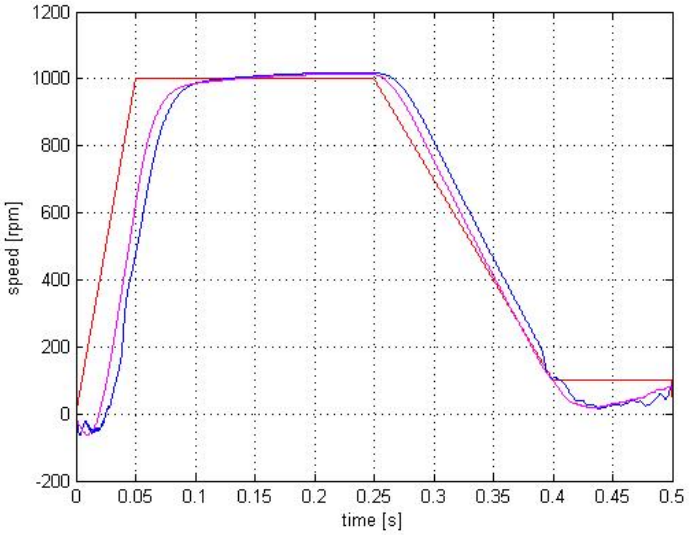

Figure 4.3: Reference speed (red), measured speed (blue), estimated speed (magenta) [rpm]

- Figure 4.4 shows the estimated mechanical angle and the mechanical angle measured by the encoder.

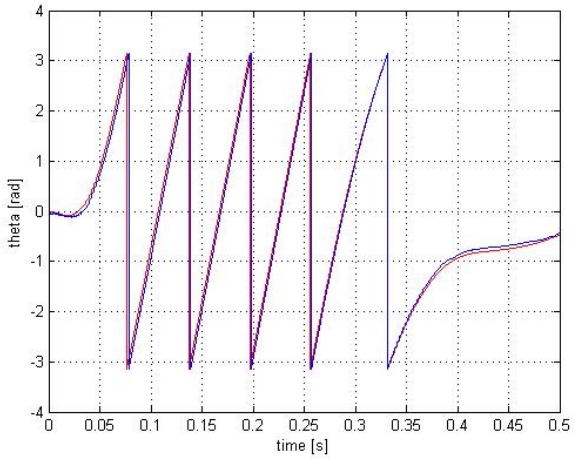

Figure 4.4: Measured angle (red) and estimated angle (blue) [rad]

- Figure 4.5 shows the d-axis and q-axis components of the negative sequence current $i^{cn}_{qd_{cn}}$ (assuming the high frequency voltage injection is not discontinued) and of the estimated flux ψ^{s}_{dq} after moving it in a reference frame moving at twice the rotor speed. It can be seen that the two estimated quantities in p.u. are very similar. The main differences consist in the fact that the negative sequence current $i^{cn}_{qd_{cn}}$ has more noise and a larger delay compared to the estimated flux ψ^{s}_{dq}. This delay increases with the increasing of the speed, however it is not a big deal as at high speed the control relies only on the MBST.

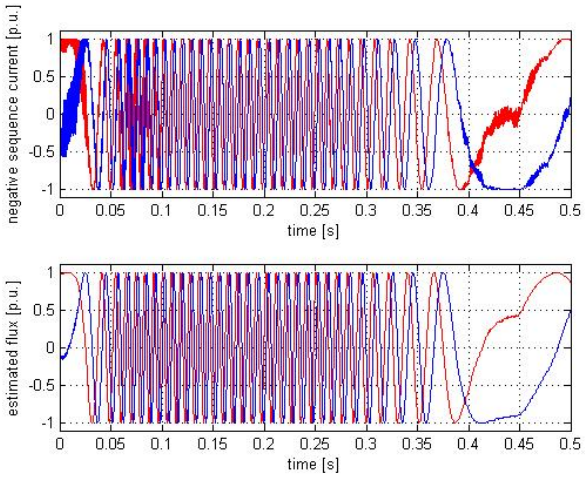

Figure 4.5: On the top d (red) and q (blue) components of the negative sequence current $i^{cn}_{qd_{cn}}$ (assuming not to disconnect the high frequency voltage injection), on bottom d (red) and q (blue) components the estimated flux ψ^{s}_{dq} after moving it in a reference frame moving at twice the rotor speed

- Figure 4.6 shows the 3-phase high frequency injected voltage. In the strategy presented in figure 4.2, high frequency voltage injection is switched off

and on the once the absolute value of the estimated speed $|\tilde{\omega}|$ crosses $\omega_{inj_{min}}$ and $\omega_{inj_{max}}$ respectively.

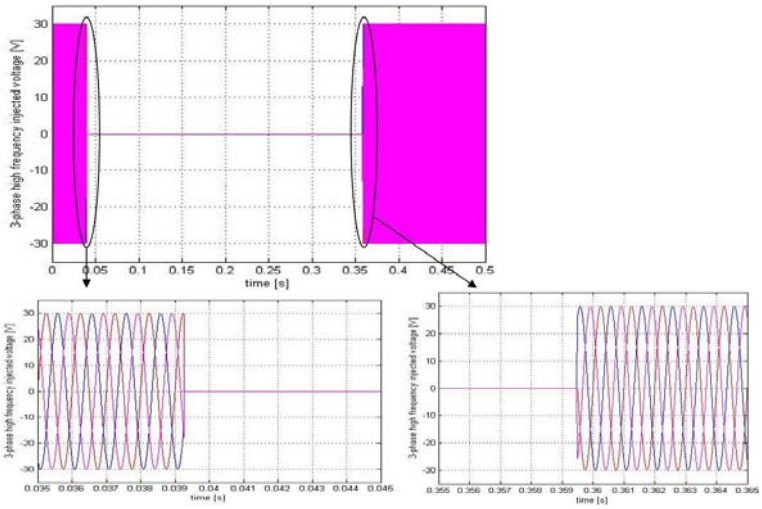

Figure 4.6: 3-phase high frequency injected voltage

- Figure 4.7 shows the position error signal of the MBST ϵ^{MBST}, the position error signal of the HFIST ϵ^{HFIST}, assuming that the high frequency voltage injection is not discontinued, and the position error signal ϵ combination of the two methods. As can be expected by observing the speed of both the MBST and HFIST, the position error signal of the MBST ϵ^{MBST} present less noise than the one of the HFIST. Furthermore, in the transition zone, they are not perfectly equal to each other and this can cause perturbation in the speed during the transition form one estimation method to the other.

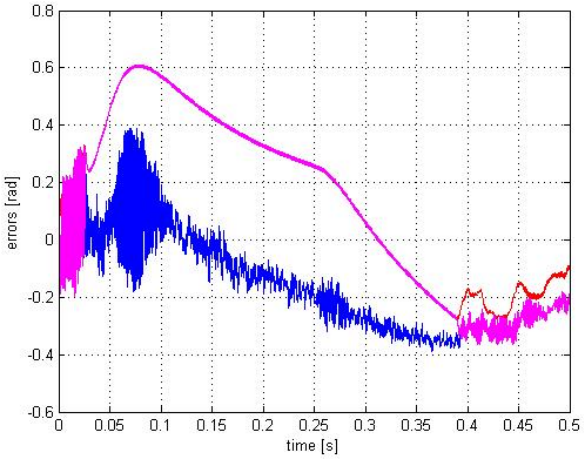

Figure 4.7: position error signal of the MBST ϵ^{MBST} (red), the position error signal of the HFIST ϵ^{HFIST} (blue), assuming that the high frequency voltage injection is not discontinued, and the position error signal ϵ (magenta) combination of the two methods

- Figure 4.8 shows the torque output of the speed regulator. The torque presents a very clean shape during MBST operation while a more noisy behavior during the HFIST operation is observed.

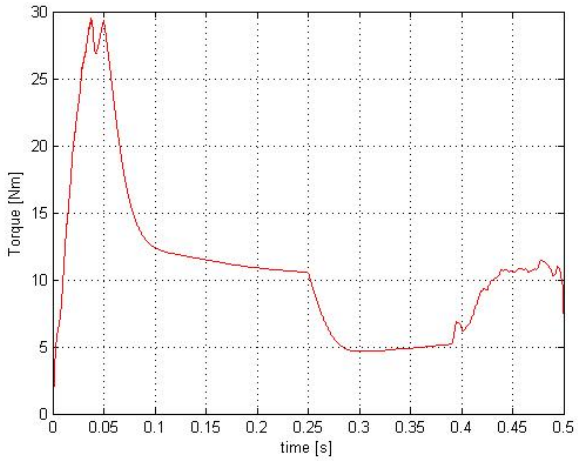

Figure 4.8: torque output of the speed regulator [Nm]

4.3.2. 0 Hz, 30 Hz and -30 Hz Operating Speed with Zero Load

The presented results are the followings:

- Figure 4.9 shows the mechanical reference speed, the estimated speed and the speed measured by the encoder.

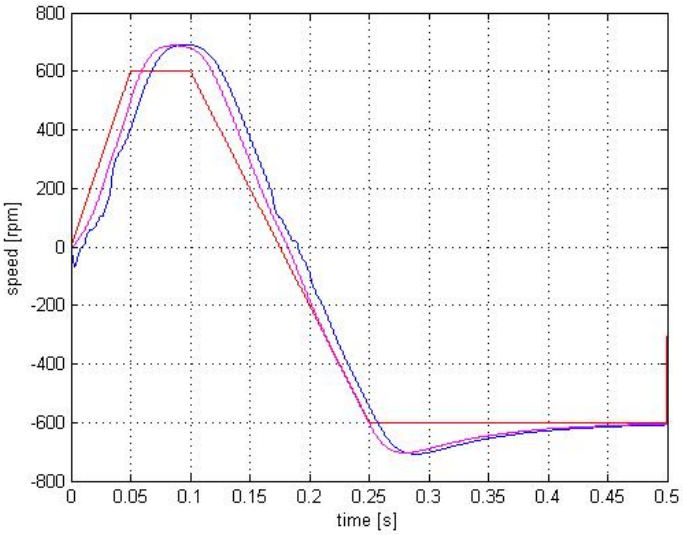

Figure 4.9: Reference speed (red), measured speed (blue), estimated speed (magenta) [rpm]

- Figure 4.10 shows the estimated mechanical angle and the mechanical angle measured by the encoder.

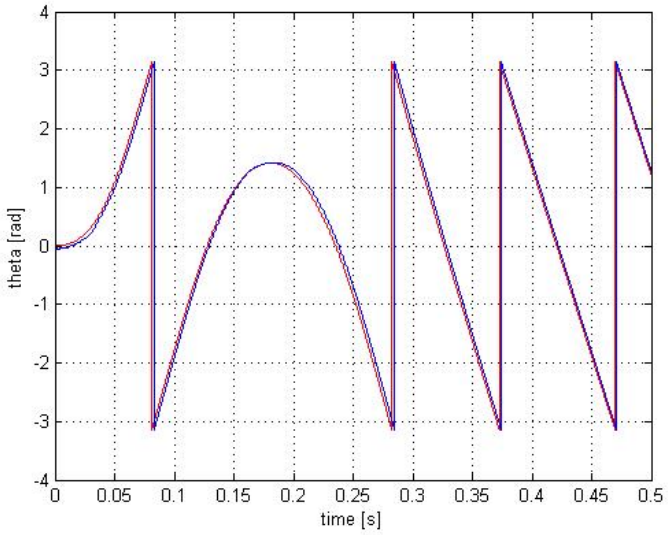

Figure 4.10: Measured angle (red) and estimated angle (blue) [rad]

- Figure 4.11 shows the d-axis and q-axis components of the negative sequence current $i^{cn}_{qd_{cn}}$ (assuming that the high frequency voltage injection is not discontinued) and of the estimated flux ψ^{s}_{dq} after moving it in a reference frame moving at twice the rotor speed.

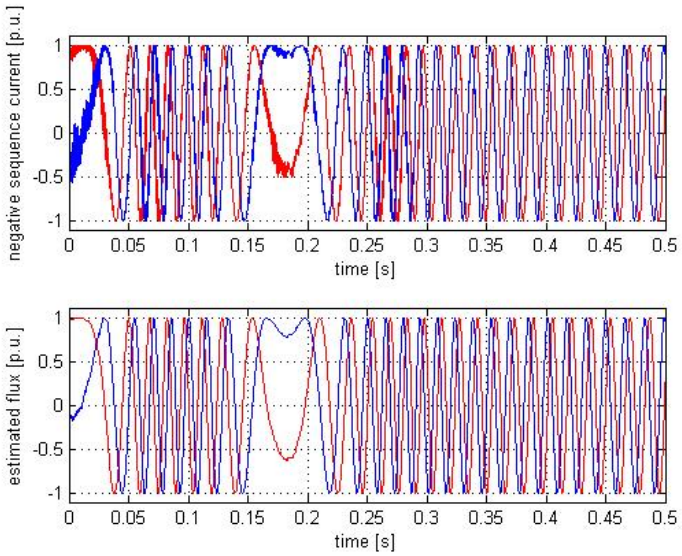

Figure 4.11: On the top d (red) and q (blue) components of the negative sequence current $i^{cn}_{qd_{cn}}$ (assuming that the high frequency voltage injection is not discontinued), on bottom d (red) and q (blue) components the estimated flux ψ^{s}_{dq} after moving it to a reference frame rotating at twice the rotor speed

- Figure 4.12 shows the 3-phase high frequency injected voltage.

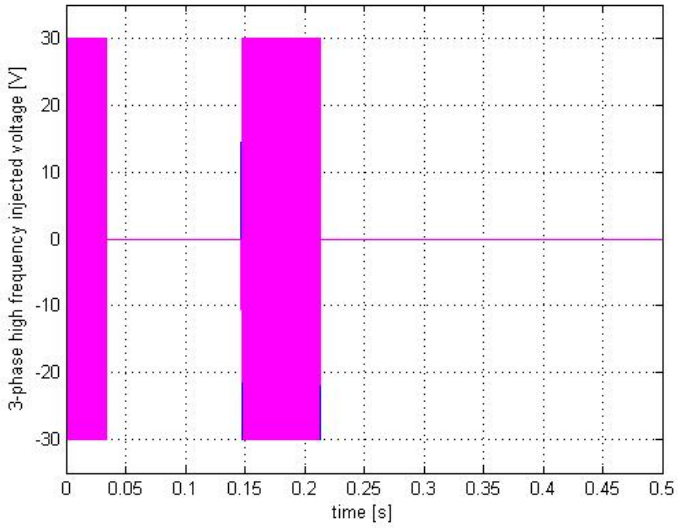

Figure 4.12: 3-phase high frequency injected voltage

- Figure 4.13 shows the position error signal of the MBST ϵ^{MBST}, the position error signal of the HFIST ϵ^{HFIST}, assuming that the high frequency voltage injection is not discontinued, and the position error signal ϵ combination of the two methods.

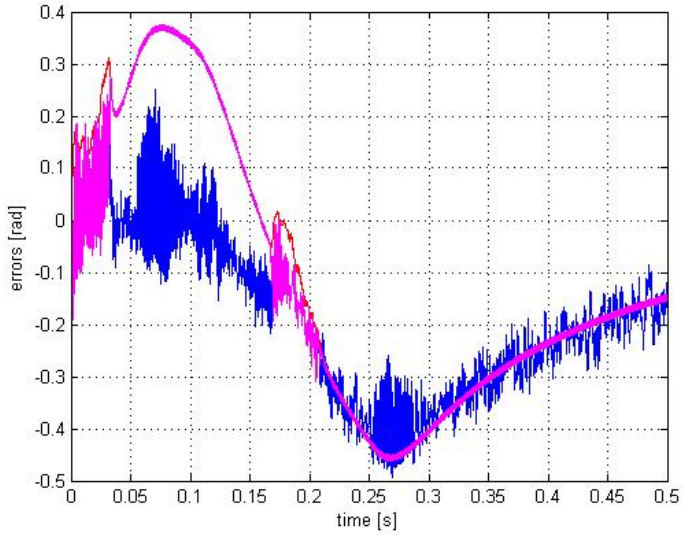

Figure 4.13: position error signal of the MBST ϵ^{MBST} (red), the position error signal of the HFIST ϵ^{HFIST} (blue), assuming that the high frequency voltage injection is not discontinued, and the position error signal ϵ (magenta) combination of the two methods

4.3.3. 0 Hz, 70 Hz and 9 Hz Operating Speed with Zero Load

The presented results are the followings:

- Figure 4.14 shows the mechanical reference speed, the estimated speed and the speed measured by the encoder.

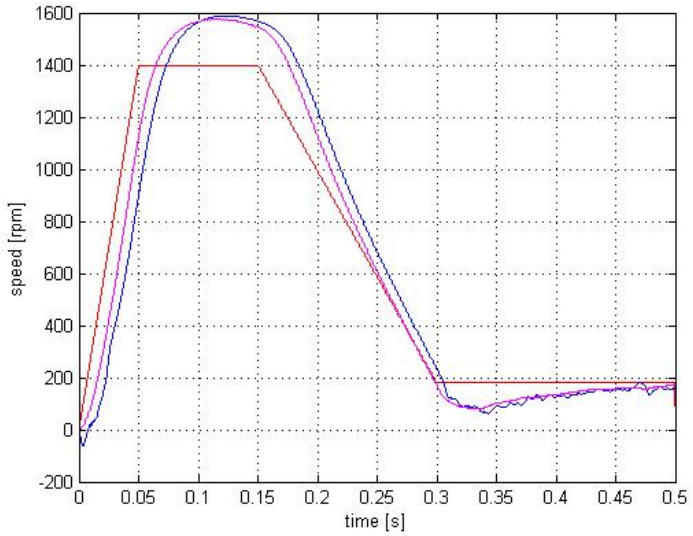

Figure 4.14: Reference speed (red), measured speed (blue), estimated speed (magenta) [rpm]

- Figure 4.15 shows the estimated mechanical angle and the mechanical angle measured by the encoder.

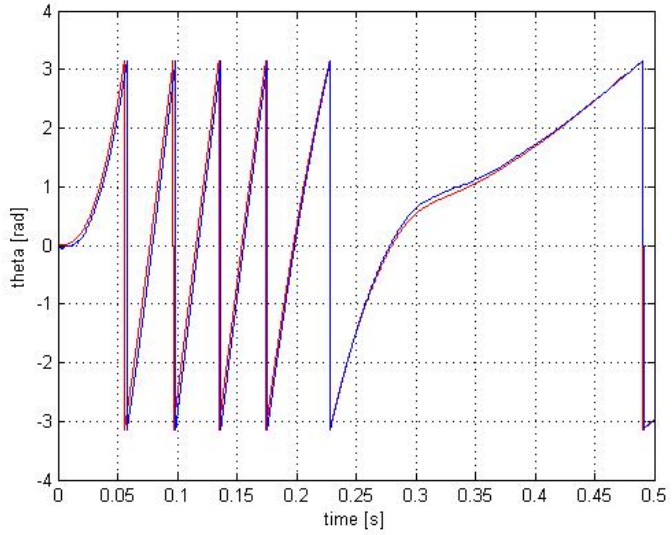

Figure 4.15: Measured angle (red) and estimated angle (blue) [rad]

- Figure 4.16 shows the d-axis and q-axis components of the negative sequence current $i^{cn}_{qd_{cn}}$ (assuming that the high frequency voltage injection is not discontinued) and of the estimated flux ψ^s_{dq} after moving it in a reference frame moving at twice the rotor speed.

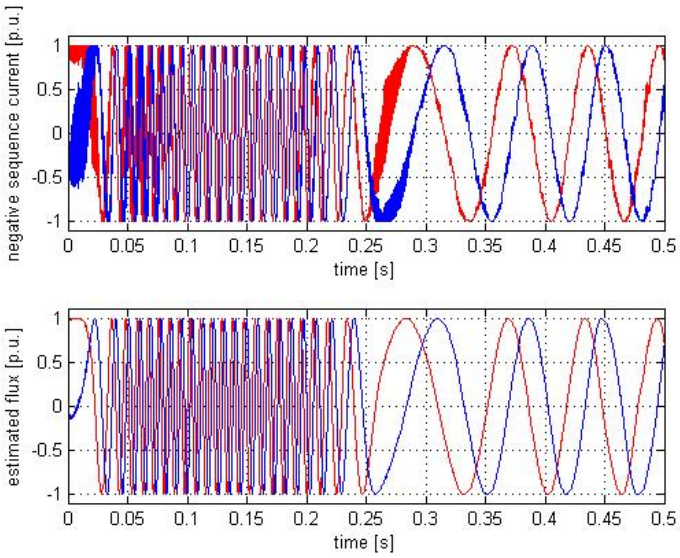

Figure 4.16: On the top d (red) and q (blue) components of the negative sequence current $i^{cn}_{qd_{cn}}$ (assuming that the high frequency voltage injection is not discontinued), on bottom d (red) and q (blue) components the estimated flux ψ^s_{dq} after moving it to a reference frame rotating at twice the rotor speed

- Figure 4.17 shows the 3-phase high frequency injected voltage.

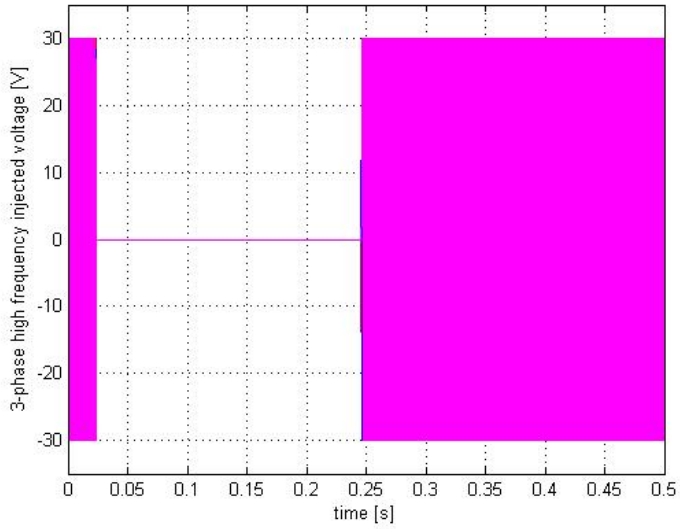

Figure 4.17: 3-phase high frequency injected voltage

- Figure 4.18 shows the position error signal of the MBST ϵ^{MBST}, the position

error signal of the HFIST ϵ^{HFIST}, assuming that the high frequency voltage injection is not discontinued, and the position error signal ϵ combination of the two methods.

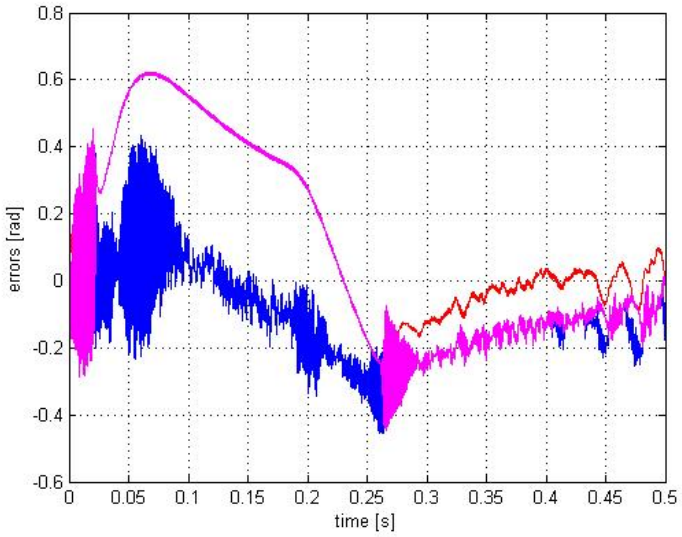

Figure 4.18: position error signal of the MBST ϵ^{MBST} (red), the position error signal of the HFIST ϵ^{HFIST} (blue), assuming not to disconnect the high frequency voltage injection, and the position error signal ϵ (magenta) combination of the two methods

4.4. Conclusion

In this chapter, the MBSM and HFSIT have been combined to allow sensorless operation over the whole speed range. In the propose method, the complex vectors coming from the MBMS and the HFSIT containing the desired position information are weighted and combined into a single complex vector, which is the input to the PLL used to estimate the rotor position and speed.
The simulation results show that the implemented hybrid technique works in a satisfactory way in all the speed range. It is also possible to operate with a reference speed ω_{ref} within the upper and lower transition speeds ω_{max} and ω_{min} without big perturbation in the actual speed of the machine.
Preliminary simulation tests have been done combining speed and rotor position sensorless estimation of the two methods instead of position error signals. For this purpose two PLLs have been employed (one for each sensorless method) and a transition zone, where the speed and the rotor position estimation was the weighted average of the quantities output of the two methods, has been defined. The problem with this hybrid configuration was the random estimation of the orientation of the magnet polarity once the high frequency voltage injection was turned on again (passing from MBST to HFIST) after been previously disconnected (passing from HFIST to MBST). In fact, the disconnection of the high frequency voltage causes the HFIST ceasing to estimate the d-axis position while,

after a subsequent reconnection, the direction of the d-axis is correctly estimated but a 180 deg uncertainty is present in magnet polarity estimation.
This problem is avoided combining the position error signals as the MBST guarantees the correct magnet polarity estimation at the beginning of the transition zone.

CHAPTER 5

PRACTICAL IMPLEMENTATION

5.1. Introduction

This chapter discusses the experimental implementation of both the MBST and the HFIST. While the MBST has been completely implemented and is fully operational, for the HFIST only preliminary experimental results are shown, as the implementation of all the signal processing needed for full sensorless control could not be completed due to time limits.

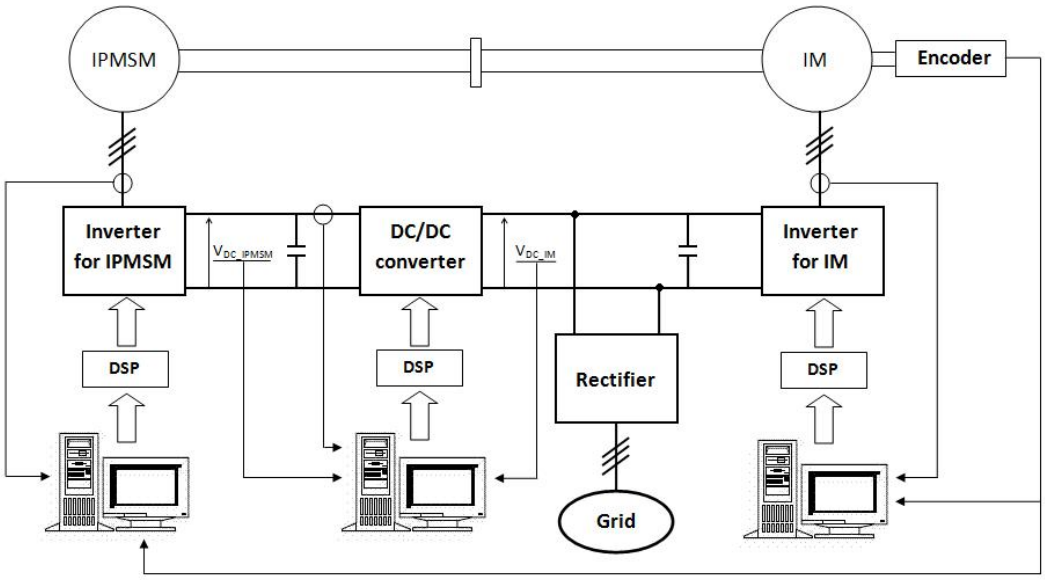

Figure 5.1: electric scheme of the experimental setup

The experimental setup used (see figure 5.1) consists off two coupled machines,

an IPMSM and an IM. Each machine is fed from an inverter, each being controlled bu the corresponding DSP. The parameters for the IPMSM already were provided in the introduction of Chapter 2. The parameters for the IM are reported in the following table for the case of a delta-connection of the stator windings.

Parameters	**Values**
Power	45 kW
Rated Torque	55 Nm
Rated Speed	2970 rpm
Rated Phase Voltage	400 V
Rated Phase Current	78.81 A
Pole pairs (P)	1

Another DSP controls the DC/DC converter used to change the value of the DC voltage $V_{DC_{IPMSM}}$ that feeds the inverter connected to the IPMSM. The resulting system is completely flexible as the energy can flow in both direction i.e. both machines can work either as a motor or a generator. The two inverters and the DC/DC converter are three-legs power converters using IGBT transistors as switches. In figure 5.1 the power links are distinguished from the measuring links using thick lines for the former and thin lines for the latter. Figures 5.2, 5.3 and 5.4 show then the pictures of respectively the rectifier and the inverter connected to IM, the inverter connected to the IPMSM and DC/DC converter. Figure 5.5 shows the picture of the two machines in the test bench.

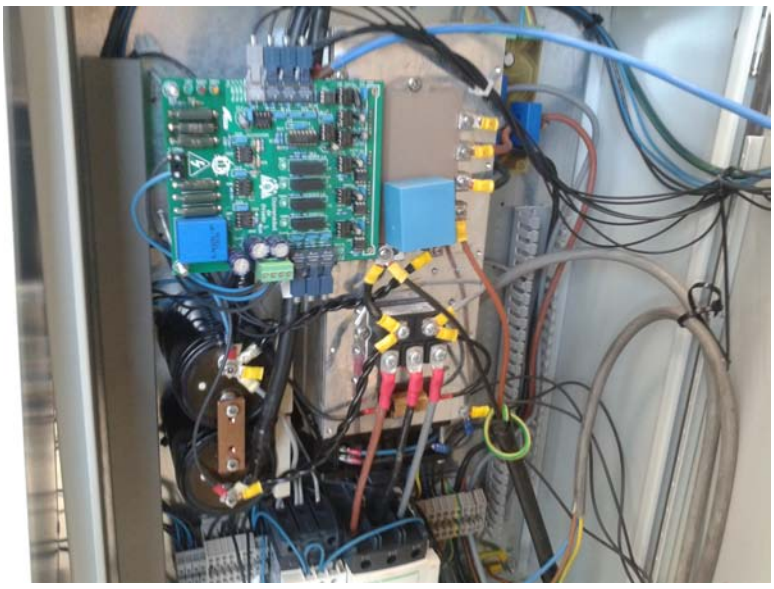

Figure 5.2: Rectifier and inverter connected to the IM

Figure 5.3: Inverter connected to the IPMSM

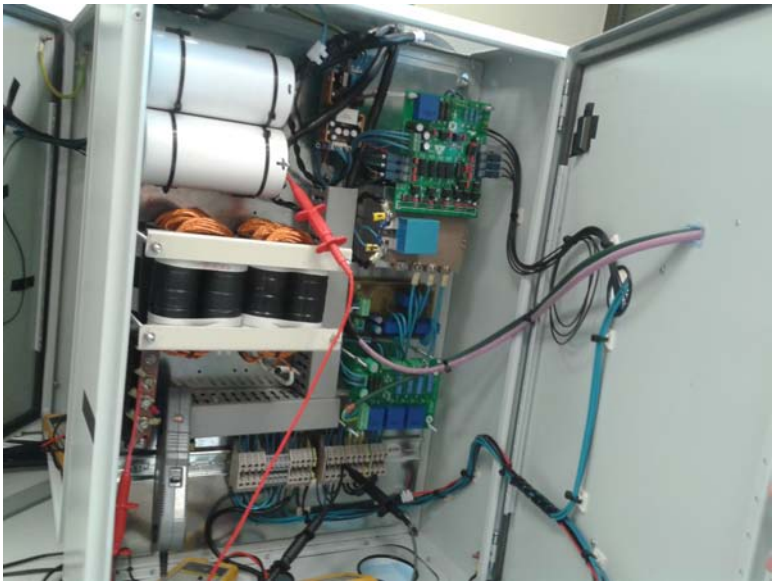

Figure 5.4: DC/DC converter

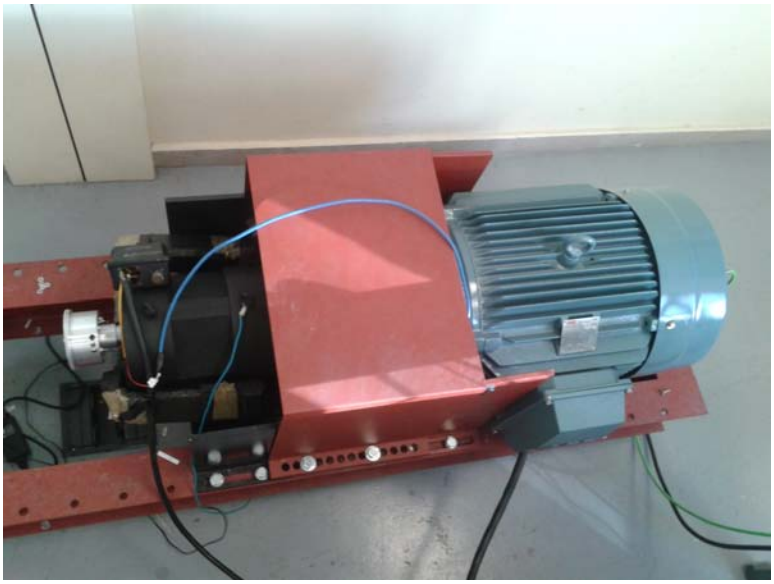

Figure 5.5: IPMSM coupled with the IM

The overall view of the system including the cabinet with the three power converters is given by the picture in figure 5.6.

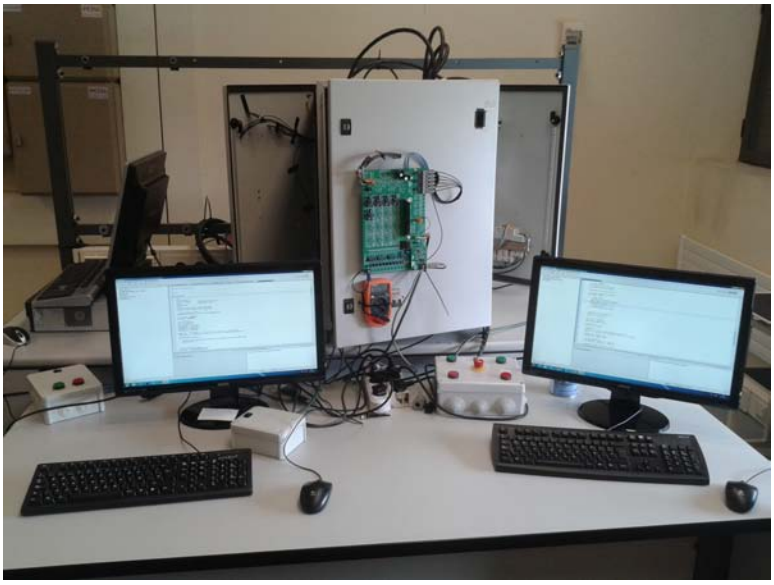

Figure 5.6: Overall view of the system

The software used to program the DSPs is Code Composer Studio 5.3.0 provided by Texas Instruments. The program is written and compiled in the PC, then being transferred to the corresponding DSP implementing the control.

5.2. Practical Implementation of the MBST

The MBST uses the measured phase current and commanded phase voltage to estimate the extended flux, from which the rotor position can be obtained. In a real implementation only the phase current is measured using sensors, while for the phase voltage, the reference voltages to the inverter are used.
All the theoretical aspects for this method were presented in Chapter 2, including the implementation of the integrator to obtaimnthe flux from the extended back-EMF. The cut off frequency f_{cut} chosen for the first order LPF that has to behave as integrator is 1 Hz. It has been chosen a very low value because it represents the lower frequency limit for the MBST as the first order LPF works as integrator only if the input signal has a frequency higher than f_{cut}.
A first order HPF was also placed to filter off the dc component of the extended back-EMF, which is present practically always due to small offsets in the current sensors. The same small continuous component in the back-EMF is found then in the estimated flux but, as the former has a much bigger magnitude than the latter, it significantly affects the estimation of the flux. The details on the digital implementation in the DSP of both the LPF replacing the integrator, the HPF and the derivative block used to obtain the back-EMF can be found in APPENDIX B.

5.2.1. Experimental Results

The DSP used for the control was also used to capture the data shown. The memory available in the DSP is quite limited, for this reason only 0.5 s can be saved. The data is further saved and visualized using Matlab.
The following tests have been realized to verify the performance of the MBST for the IPMSM:

- Steady state operation at 200 rad/s (electrical speed), with no load. The same test has been done with a negative reference speed of -200 rad/s;
- Steady state operation at 200 rad/s (electrical speed), with load;
- Steady state operation at 250 rad/s (electrical speed), with no load;
- 50 rad/s speed step, from 200 rad/s up to 250 rad/s:

All the results were taken speeding up first the motor using the encoder and switching to sensorless operation once the speed is high enough (around 100 rad/s in electrical units). The q-axis current of IM motor was used to control the torque, the d-axis current was set to its rated value in order to maintain constant rotor flux.

Steady State Operation at 200 rad/s with no Load

The results presented are the following:

- Figure 5.7 shows the electrical speed measured by the encoder, filtered using a second order LPF with a cut off frequency f_{cut} of 100 Hz, and the estimated electrical speed. The estimated speed presents a ripple at the fundamental frequency due to the little continuous component still present in the current measurement which affects to the estimated extended back-EMF, and consequently to the flux.

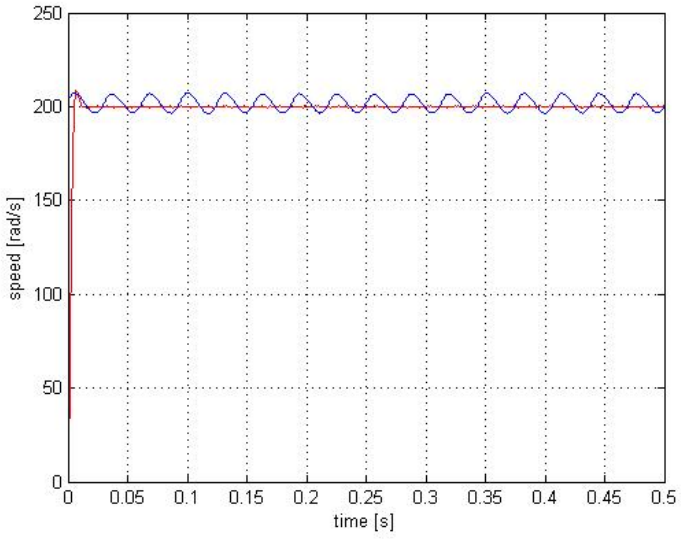

Figure 5.7: Measured speed (red) and estimated speed (blue) [rad/s]

- Figure 5.8 shows the measured electrical angle and the estimated electrical angle. The estimation of the angle is very precise as it is not possible to see any difference between the two.

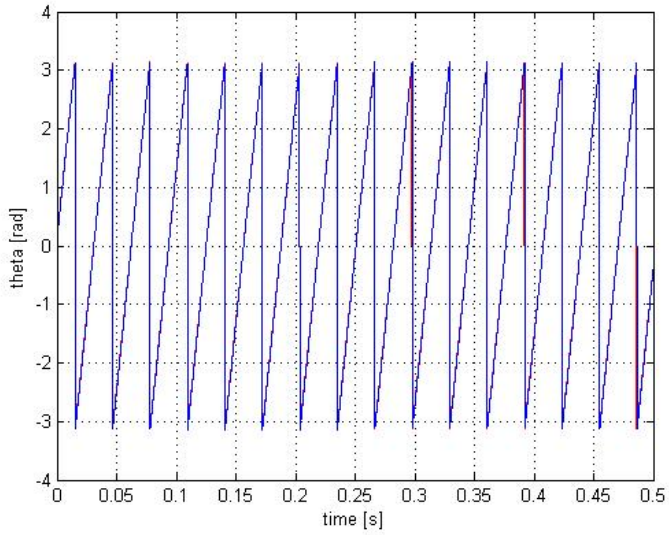

Figure 5.8: Measured angle (red) and estimated angle (blue) [rad]

- Figure 5.9 shows d-axis and q-axis of the estimated flux.

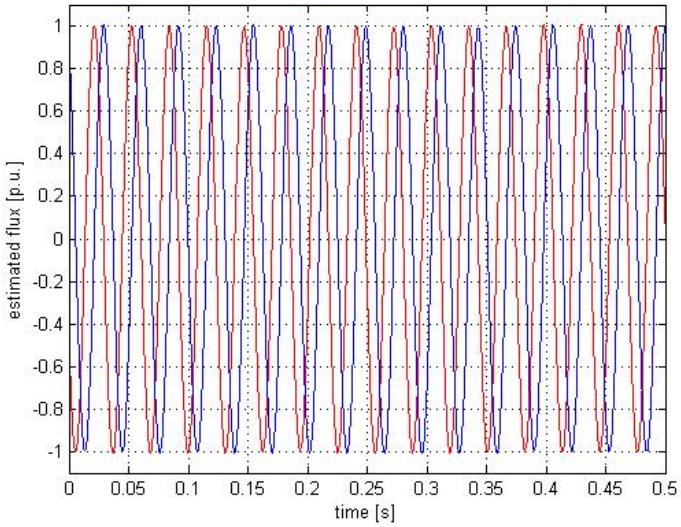

Figure 5.9: d-axis (red) and q-axis (blue) components of the estimated flux [Vs]

Steady State Operation at -200 rad/s with no Load

The results presented are the following:

- Figure 5.10 shows the electrical speed measured by the encoder, filtered using a second order LPF with a cut off frequency f_{cut} of 100 Hz, and the estimated electrical speed. The estimated speed presents the same ripple at the fundamental frequency for the previous experimental result.

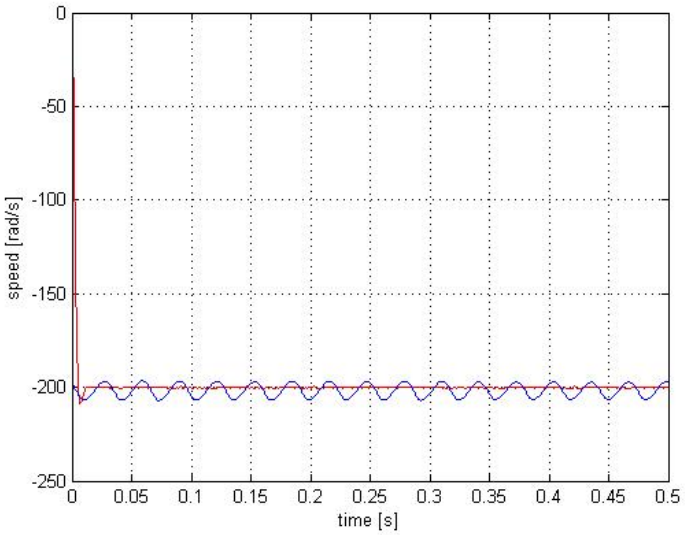

Figure 5.10: Measured speed (red) and estimated speed (blue) [rad/s]

- Figure 5.11 shows the measured electrical angle and the estimated electrical angle.

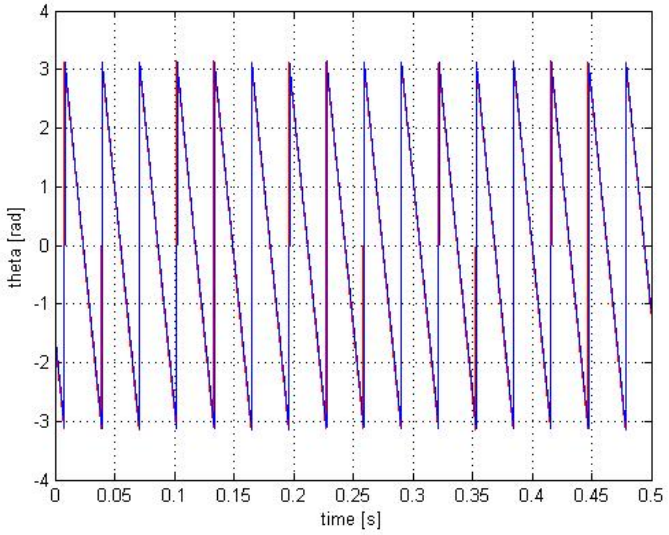

Figure 5.11: Measured angle (red) and estimated angle (blue) [rad]

- Figure 5.12 shows d-axis and q-axis of the estimated flux.

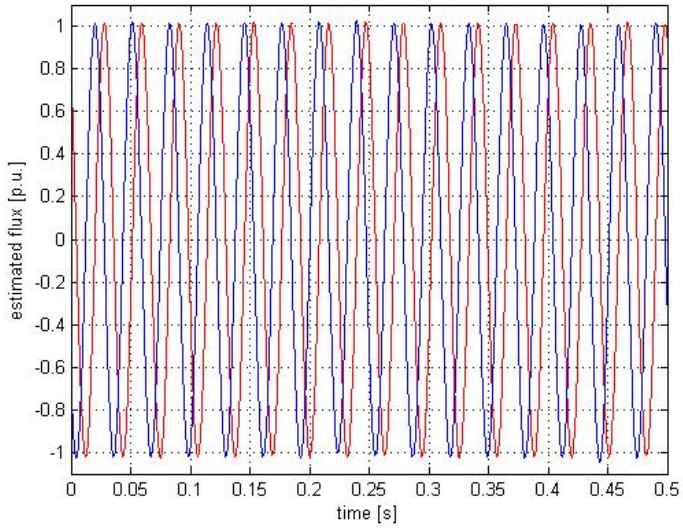

Figure 5.12: d-axis (red) and q-axis (blue) components of the estimated flux [Vs]

Steady State Operation at 200 rad/s with Load

The results presented are the following:

- Figure 5.13 shows the electrical speed measured by the encoder, filtered using a second order LPF with a cut off frequency f_{cut} of 100 Hz, and the estimated electrical speed. The ripple presented in the estimated speed is smoothed by the load applied to the IPMSM.

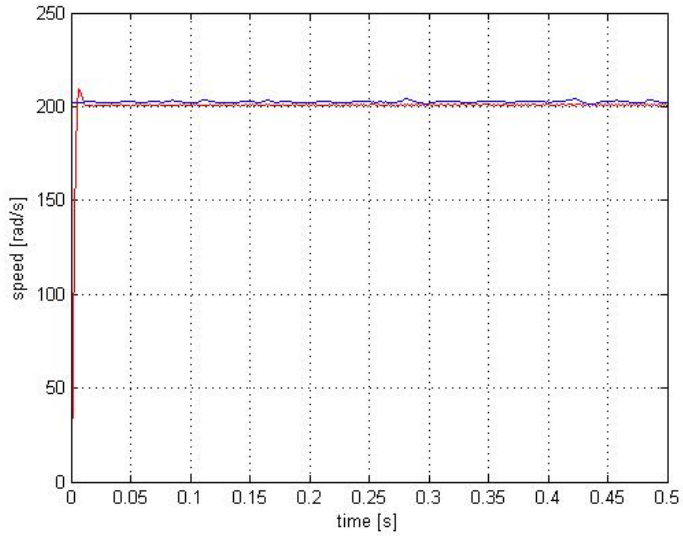

Figure 5.13: Measured speed (red) and estimated speed (blue) [rad/s]

- Figure 5.14 shows the measured electrical angle and the estimated electrical angle. The error between the estimated and the measured angle is larger than for the case of no load operation. The reason for that is the bigger magnitude of the phase currents which, in combination with a non perfect knowledge of the machine parameters, affects more the rotor position estimation.

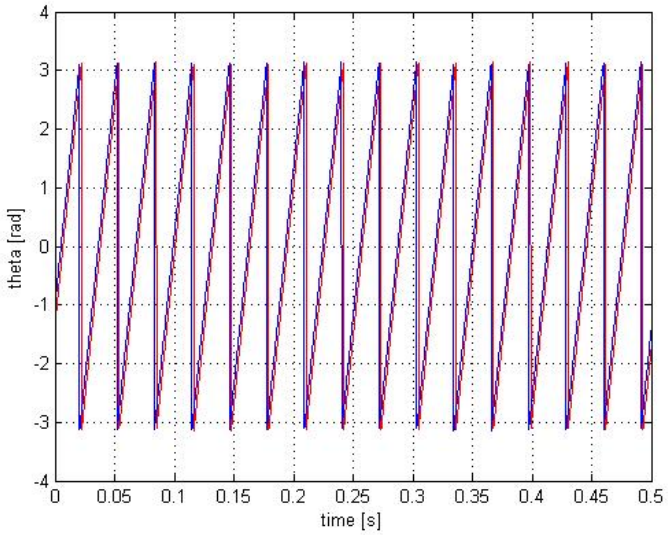

Figure 5.14: Measured angle (red) and estimated angle (blue) [rad]

- Figure 5.15 shows d-axis and q-axis components of the measured phase current (top) and the d-axis and q-axis components of the reference voltage to the inverter (bottom).

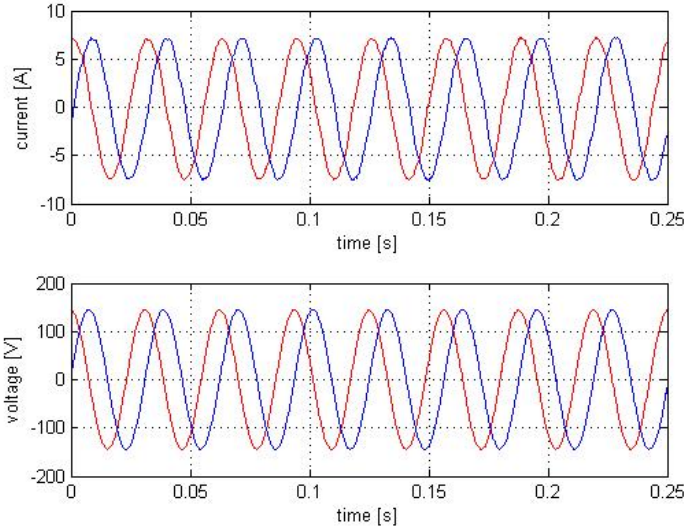

Figure 5.15: Top: d (red) and q (blue) components of the measured current. Bottom: d (red) and q (blue) components of the reference voltage for the inverter

Steady State Operation at 250 rad/s with no Load

The results presented are the following:

- Figure 5.16 shows the electrical speed measured by the encoder, off-line filtered with a second order LPF with a cut off frequency f_{cut} of 100 Hz, and the estimated electrical speed. The estimated speed presents a ripple at the fundamental frequency.

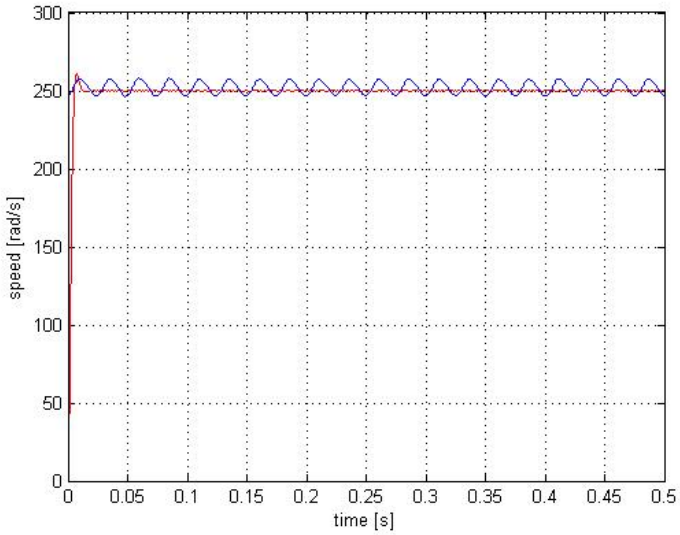

Figure 5.16: Measured speed (red) and estimated speed (blue) [rad/s]

- Figure 5.17 shows the measured electrical angle and the estimated electrical angle.

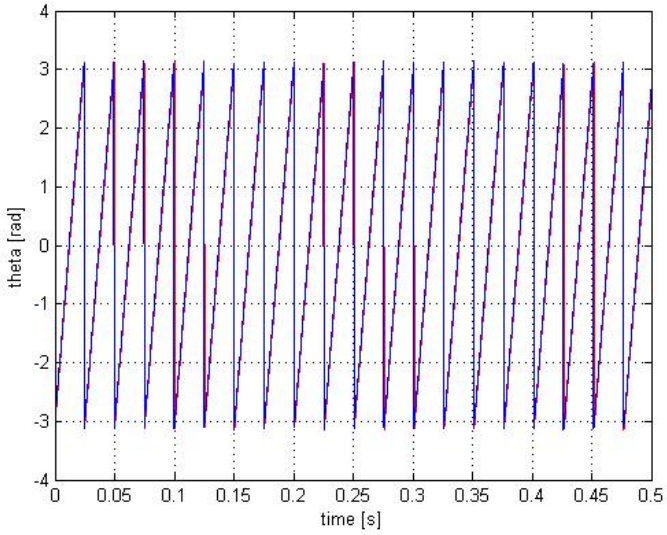

Figure 5.17: Measured angle (red) and estimated angle (blue) [rad]

- Figure 5.18 shows d-axis and q-axis of the estimated flux.

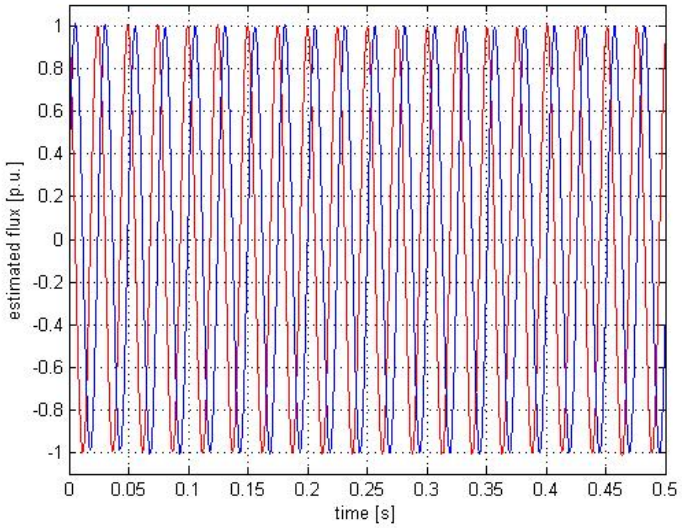

Figure 5.18: d-axis (red) and q-axis (blue) components of the estimated flux [Vs]

50 rad/s Speed Step with no Load

The results presented are the following:

- Figure 5.19 shows the electrical speed measured by the encoder, off-line filtered with a second order LPF with a cut off frequency f_{cut} of 100 Hz, and the estimated electrical speed. The estimated speed follows the actual speed of the motor with almost no delay.

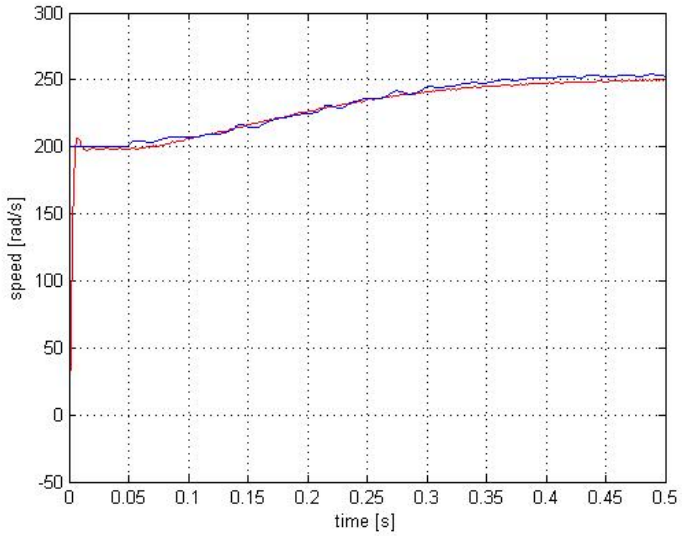

Figure 5.19: Measured speed (red) and estimated speed (blue) [rad/s]

- Figure 5.20 shows the measured electrical angle and the estimated electrical angle.

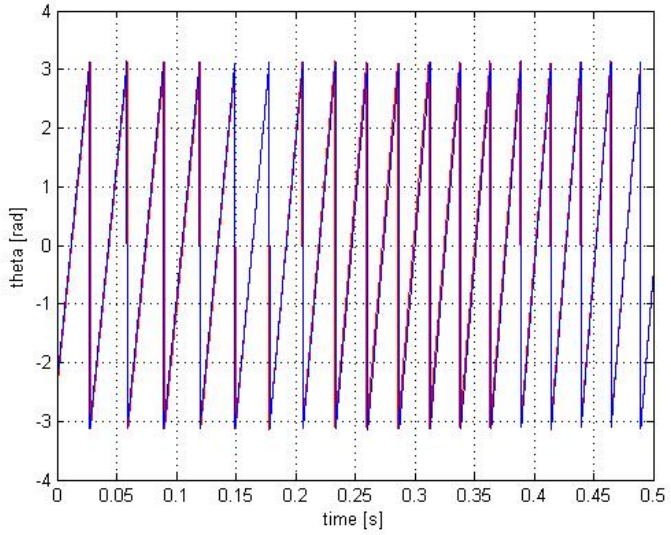

Figure 5.20: Measured angle (red) and estimated angle (blue) [rad]

- Figure 5.21 shows d-axis and q-axis of the estimated flux. In the transient region the magnitude of the estimated flux exceeds its rated value. This is due to the non perfect knowledge of the machine parameters which combined with the larger value of the phase currents in the transient, produces a bigger error in the estimated flux.

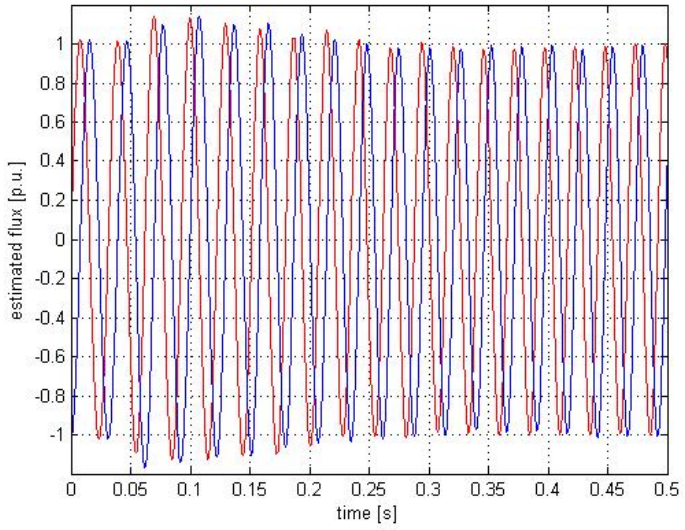

Figure 5.21: d-axis (red) and q-axis (blue) components of the estimated flux [Vs]

5.3. Practical Implementation of the HFIST

Practical implementation of HFIST could not be completed due to time restrictions, still several tests injecting the high frequency carrier signal-voltage in the IPMSM and doing using off-line signal processing to extract the rotor position information has been done. Therefore the signal processing has been performed using FFT Matlab functions. The high frequency carrier signal-voltage injected has a frequency f_c and a magnitude V_c of 1000 Hz and 30 V respectively, which coincide with the values used for simulation.
However, there are several aspects that need to be concidered for the complete implementation of the method, including:

- Secondary (saturation induced) saliencies;
- The non-ideal behavior of the inverter due to the dead time that produces extra harmonics in the current;
- The current regulator reaction to the negative sequence current. This source of distortion can be eliminate by using an adaptive BSF in the current feedback;
- The pulse width modulation strategy;
- Sensor accuracy and A/D converters resolution.

Among all these distortion sources, the most difficult to compensate is the secondary saliencies as the salient nature of IPMSM, and consequently their suitability for sensorless control, can be strongly affected by the operating conditions. While saturation in the d-axis normally occurs due to the magnet and does not significantly change when fundamental current is injected, the q-axis inductance can vary in a wide range as the operating conditions change. The final result is that the salient behavior of the machine seen by the high-frequency signals can dramatically change with the operating point. Two effects can be distinguished: a reduction of the salience ratio, with a nonsalient behavior in the limit, and a movement of the minimum reluctance axis away from the magnetic d-axis because of cross saturation. Both effects will result in a deterioration of the sensorless control, and often instability, unless compensating strategies are adopted. In this respect the design of PMSMs for sensorless control is receiving increasing attention and is expected to be a field of great activity in the coming years. The signal processing result of the HFIST is, ideally, a signal of the form of equation given by 5.1, where x_{qd} and X_{rotor} are, for the HFIST considered, respectively $i^{cn}_{qd_{cn}}$ and I_{cn}.

$$x_{qd} = X_{rotor} e^{jh_r \vartheta_r} \tag{5.1}$$

Unfortunately, the assumption of a single salience is not realistic in practice hence the secondary salience has to be considered. It causes the measured signal

to have an expression of the form of equation 5.2, where the first term in the right side of the equation is the desired signal containing the rotor position information of equation 5.1 and the rest of the components are secondary salience (noise) which are normally harmonics of the fundamental excitation frequency ω_e, for saturation-induced salience.

$$x_{qd} = X_{rotor} e^{jh_r\vartheta_r} + \sum x_{dq_{ss}} e^{jh\omega_e t} \tag{5.2}$$

Several methods have been proposed to address this issues, most of them having the form shown in figure 5.22.

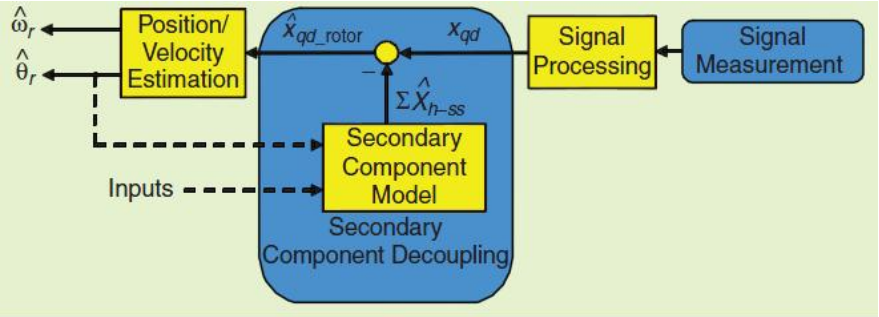

Figure 5.22: Schematic representation of secondary salience decoupling and position estimation [13]

An example of FFT of the measured current is given by figure 5.23, where the motor considered is an induction motor and the high frequency carrier signal-voltage injected has a frequency f_c and a magnitude V_c of 500 Hz and 20 V respectively. The desired negative sequence current component has a frequency equal to $14\omega_r$ as the harmonic order h_r of the salience of the considered induction machine is 14 (14 rotor bars per pole pair). The unwanted harmonic due to saturation that has to be compensated is the one at the frequency $2\omega_e$. It can be seen from figure 5.23 that it has almost the same magnitude as the frequency component at $14\omega_r$.

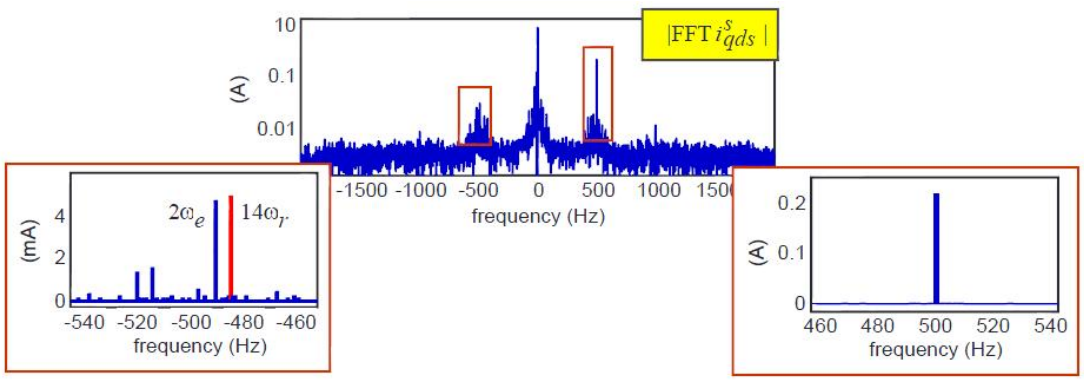

Figure 5.23: FFT of the measured current of an induction machine[12]

The compensation strategy, shown in figure 5.22 for a general case, consists in the measurement, during an off line commissioning process, of the saturation induced components of the negative sequence current. This information is stored either using time-based or frequency-based lookup tables and is then later accessed during the normal sensorless operation of the drive. Figure 5.24 shows this compensation strategy for the considered induction machine displaying also the wave form of the resulting currents.

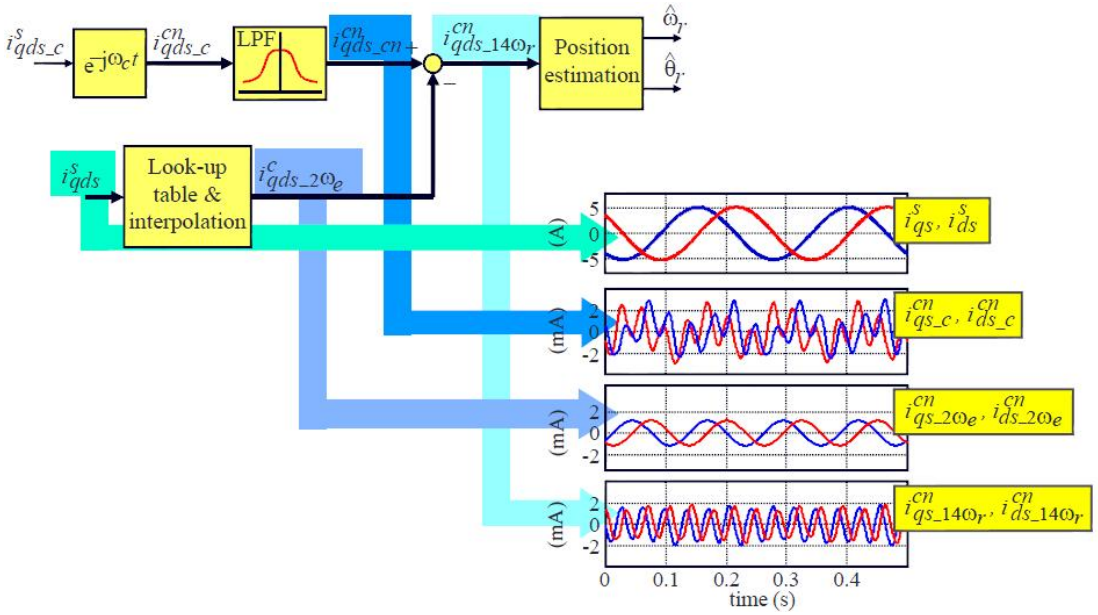

Figure 5.24: Schematic representation of secondary salience decoupling and position estimation for an induction machine [12]

5.3.1. Experimental Results

A high frequency signal voltage was injected to the IPMSM, the resulting phase currents were used using two current and a digital scope. The signal processing was implemented in Matlab. The results are discussed following.

Standstill Operation with no Load

The following results have been obtained injecting the high frequency signal voltage with the motor at standstill. Figure 5.25 shows the FFT of the measured current and the output of the two steps of the signal processing explained in Chapter 3. The resulting negative sequence current $i^{cn}_{qd_{cn}}$ is then the input to a PLL from which the rotor position is obtained.
The spectrum of the measured current i^s_{qd} is perfectly clean and equal to the spectrum of $i^s_{qd_c}$ which is the output of the first step of the signal processing as the machine is operating at no load, and therefore the magnitude of the fundamental current is zero.

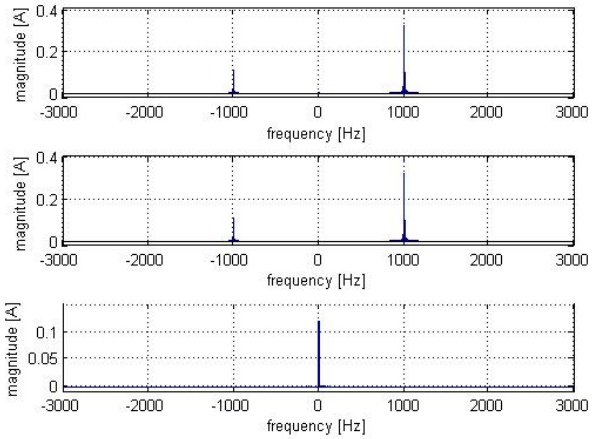

Figure 5.25: Top: FFT of the measured current in the stationary reference frame (i^s_{qd}), cetral chart FFT of the output of the first step of the signal processing ($i^s_{qd_c}$). Bottom: FFT of the final output of the signal processing ($i^{cn}_{qd_{cn}}$)

Standstill Operation with Load

The following results have been obtained injecting the high frequency signal voltage in the motor controlled at standstill, the induction machine (IM) being current controlled to apply load. Figure 5.26 shows the FFT of the measured current and the output of the two steps of the signal processing explained in Chapter 3. As can be seen from the central chart the fundamental current is not completely filtered after the first step, hence a BSF at a frequency ω_c is placed in order to get rid of that component after the transformation to the -ω_c rotating reference frame.

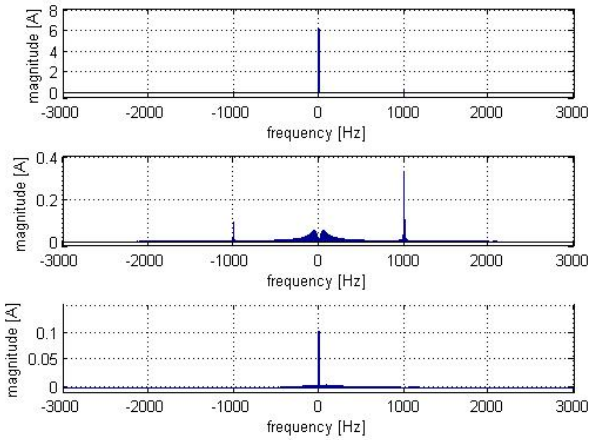

Figure 5.26: Top: FFT of the measured current in the stationary reference frame (i^s_{qd}), cetral chart FFT of the output of the first step of the signal processing ($i^s_{qd_c}$). Bottom: FFT of the final output of the signal processing ($i^{cn}_{qd_{cn}}$)

Constant Speed of 50 rad/s with Load

The following results have been obtained injecting the high frequency signal voltage with the motor controlled at standstill, the induction machine (IM) being current controlled to apply load.
The results presented are the following:

- Figure 5.27 shows the d-axis and q-axis components of the negative sequence current $i^{cn}_{qd_{cn}}$ after removing the initial transient due to the filters. The waveform still presents some harmonic components due to the non perfect filtering process.

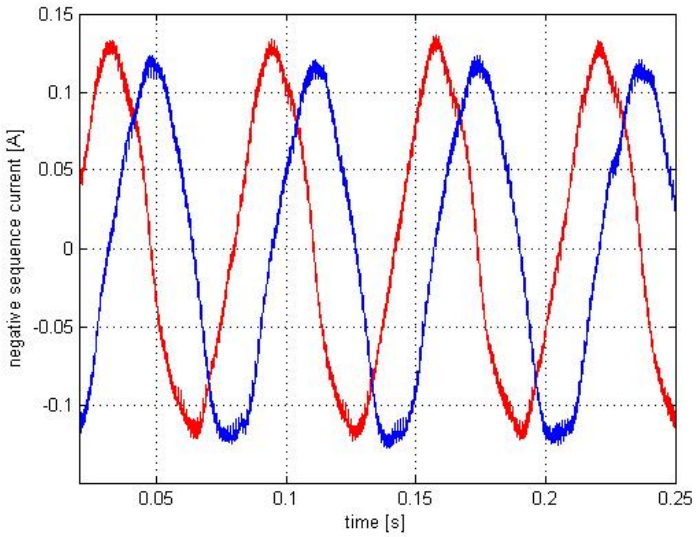

Figure 5.27: d (red) and q (blue) components of the negative sequence current $i^{cn}_{qd_{cn}}$

- Figure 5.28 shows the 3D chart with trajectory of the negative sequence current $i^{cn}_{qd_{cn}}$ after removing the initial transient due to the filters. An high frequency component is superimposed to the trajectory due to the non perfect filtering process.

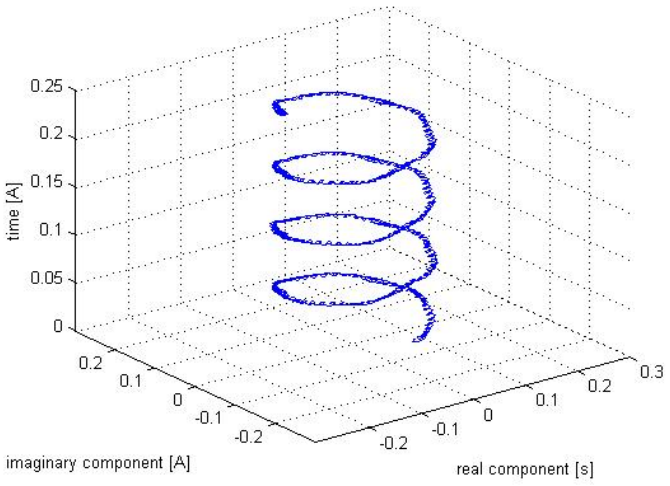

Figure 5.28: 3D chart with the trajectory of the negative sequence current $i^{cn}_{qd_{cn}}$

- Figure 5.29 shows FFT of the measured current in the stationary reference frame (i^{s}_{qd}), of the output of the first step of the signal processing ($i^{s}_{qd_c}$) and of the final output of the signal processing ($i^{cn}_{qd_{cn}}$). As in figure 5.26 the fundamental current is not completely filtered after the first step, hence a BSF at the frequency of ω_c is placed in order to get rid of that component after the transformation to the -ω_c rotating reference frame.

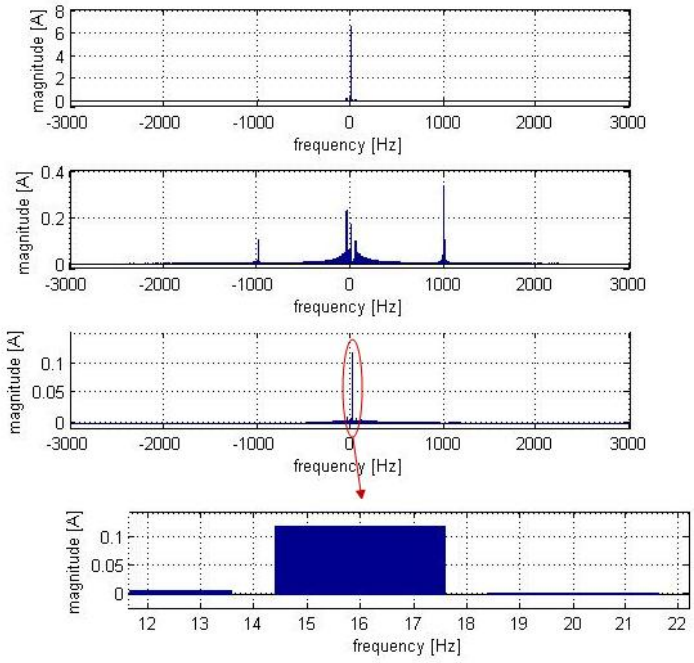

Figure 5.29: Top: FFT of the measured current in the stationary reference frame (i^{s}_{qd}), cetral chart FFT of the output of the first step of the signal processing ($i^{s}_{qd_c}$). Bottom: FFT of the final output of the signal processing ($i^{cn}_{qd_{cn}}$) with zoom at low frequency

Constant Speed of 100 rad/s with Load

The following results have been obtained injecting the high frequency signal voltage in the motor controlled at standstill, the induction machine (IM) being current controlled to apply load.
The results presented are the following:

- Figure 5.30 shows the d-axis and q-axis components of the negative sequence current $i^{cn}_{qd_{cn}}$ after removing the initial transient due to the filters.

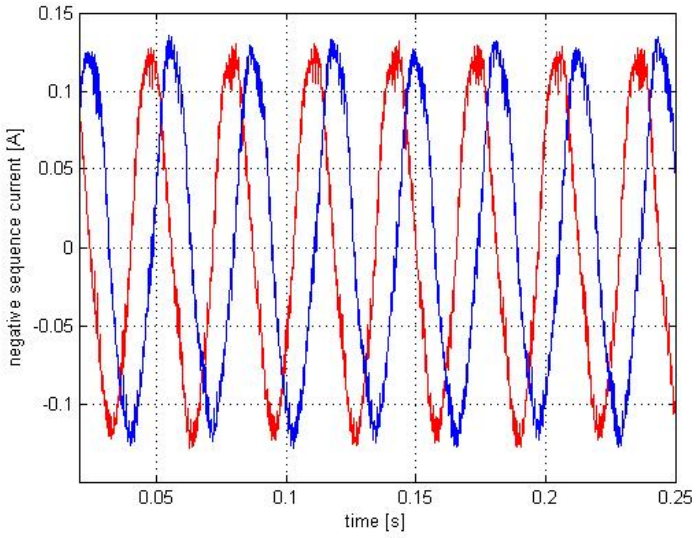

Figure 5.30: d (red) and q (blue) components of the negative sequence current $i^{cn}_{qd_{cn}}$

- Figure 5.31 shows the 3D chart with trajectory of the negative sequence current $i^{cn}_{qd_{cn}}$ after removing the initial transient due to the filters.

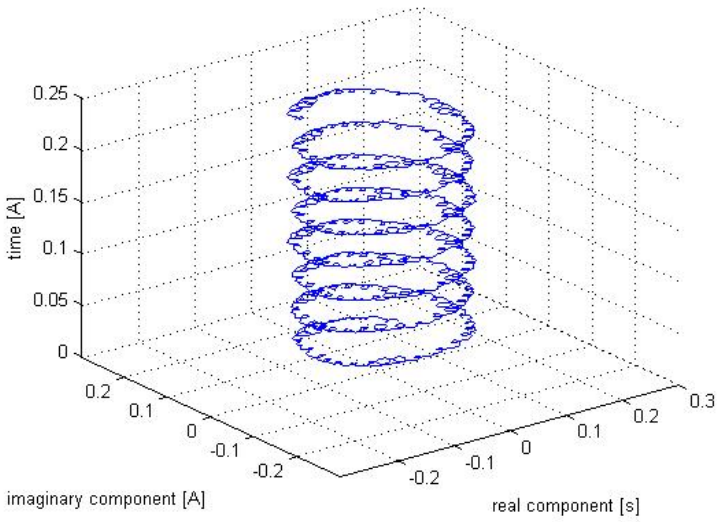

Figure 5.31: 3D chart with the trajectory of the negative sequence current $i^{cn}_{qd_{cn}}$

- Figure 5.32 shows FFT of the measured current in the stationary reference frame (i^{s}_{qd}), of the output of the first step of the signal processing ($i^{s}_{qd_c}$) and of the final output of the signal processing ($i^{cn}_{qd_{cn}}$).

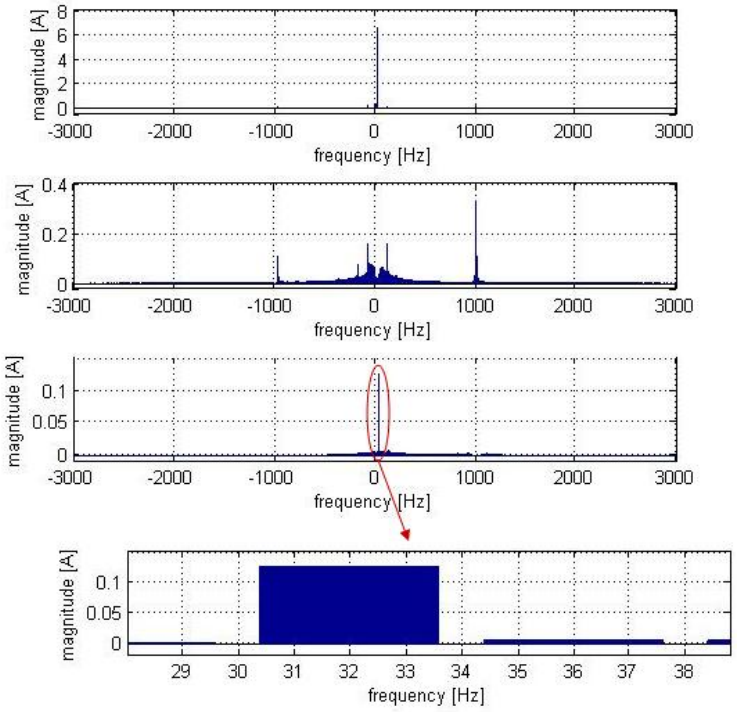

Figure 5.32: Top: FFT of the measured current in the stationary reference frame (i^{s}_{qd}), cetral chart FFT of the output of the first step of the signal processing ($i^{s}_{qd_c}$). Bottom: FFT of the final output of the signal processing ($i^{cn}_{qd_{cn}}$) with zoom at low frequency

5.4. Conclusions

In this section, the MBST has been successfully implemented in the experimental set up. The stable operation of the motor for different operating conditions has been experimentally verified. As the operating speed decreases the speed and rotor angle sensorless estimation deteriorate and consequently the control of the machine gets more unstable. For very low operating speeds it eventually becomes unstable.
Regarding the HFIST, the preliminary experimental results show the feasibility of the method considered as the negative sequence current has been obtained after the signal processing. Despite this, the implementation in a experimental set up couldn't be completed as is not so straightforward as it requires a very careful signal processing design.

CHAPTER 6

CONCLUSIONS

This master thesis work deals with the implementation, both at simulation and experimental levels, of the sensorless control of an IPMSM in all the speed range. Two different sensorless techniques have been combined for this purpose: one suitable for zero to low operating speeds and the other one for medium to high operating speeds. These techniques are named HFIST and MBST respectively. The combination of the two methods permits to operate the IPMSM over the entire speed range.
The simulation results show the feasibility of the techniques considered and in particular of the hybrid method combining HFIST with the MBST. The hybrid technique chosen combines the output position error signals of the two sensorless techniques into a single PLL.
Regarding the experimental implementation, satisfactory results have been obtained operating using the MBST. The HFSIT could not be implemented completely. Nevertheless, preliminary results injecting high frequency voltage in the machine were obtained, which demonstrate the feasibility of the HFIST method.

6.1. Summary of the work

The list below summarizes all the activities that have been realized:

- Analytical models both for MBST as well as for HFSIT have been developed.
- Both models have been successfully implemented using Simulink.
- MBST as well as HFSIT have been combined in simulation to cover the whole speed range.

- MBST has been successfully implemented in a experimental setup.
- HFSIT could only be partially (off-line) implemented in a experimental setup.

The simulation results obtained demonstrate that despite the bandwidth of the control is decreased by the presence of the filters in the signal processing of the HFIST, accurate and stable speed and position control, with adequate bandwidth, was achieved.

6.2. Future Research

The following are considered as especially challenging and prommising for future research:

- Improvement of the experimental implementation of the MBST, with especial focus on the compensation of the current sensors offsets and other non-ideal behaviors, which limit in the end the minimum speed at which the method can work.
- Regarding the HFIST, the signal processing implemented off line using Matlab should be implemented in the DSP. This should include measurement and decoupling of the secondary saliencies. For this purpose it is necessary to create a lookup table with the values of the unwanted additional component of the negative sequence current for different levels of torque. This process is carried out with the machine at stand still, controlling its position and changing the level of torque applied. The current is then measured and off-line processed obtaining the unwanted additional component that has to be included in the lookup table.
- Once the HFIST is implemented to operate in real time, HFSIT and MBST should be combined. This would required the discretization and implementation in the DSP of the algorithms already implemented in the DSP.
- Finally, optimization of the different methods is needed. Different filters bandwidths and controller gains need to be selected for the implementation of the methods, their selection involving a trade off between the desired bandwidth and the sensitivity to noise. Establishing a deterministic criteria for the selection of the different parameters and evaluation of the drive performance would be highly desirable.

APPENDIX A

APPENDIX A - MTPA

The Maximum Torque Per Ampere (MTPA) strategy has the target of optimizing the motor operation by providing the maximum torque with the minimum possible stator current for any operating condition. MTPA strategies therefore calculate the minimum value of d-axis and q-axis current needed to get the commanded torque coming from the speed regulator. In the implementation shown in figure A.1, this target is achieved by means of two blocks:

- 'Block1' provides the q-axis current from the output torque of the speed regulator;
- 'Block2' provides the d-axis current from the output q-axis current of 'Block1'.

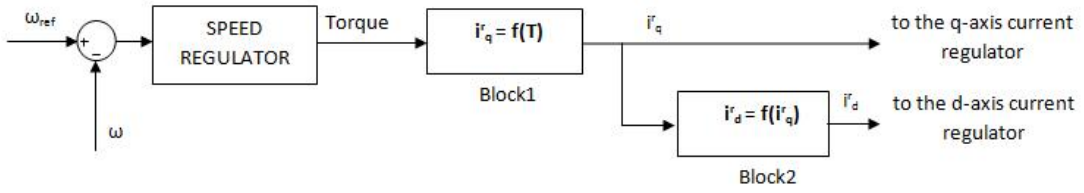

Figure A.1: Block diagram of the MTPA implementation

Both d-axis and q-axis currents are then the input for the d-axis and q-axis current regulators respectively.
The torque in an IPMSM A.1, is function both of the d-axis and q-axis currents.

$$T_e = \frac{3}{2}P(\Psi_{pm}i_q^r + (L_d - L_q)i_d^r i_q^r) \tag{A.1}$$

where the d-axis and q-axis currents are shown in figure A.2. Therefore it is possible to write:

$$\begin{aligned} i_d^r &= I\cos\varphi \\ i_q^r &= I\sin\varphi \end{aligned} \tag{A.2}$$

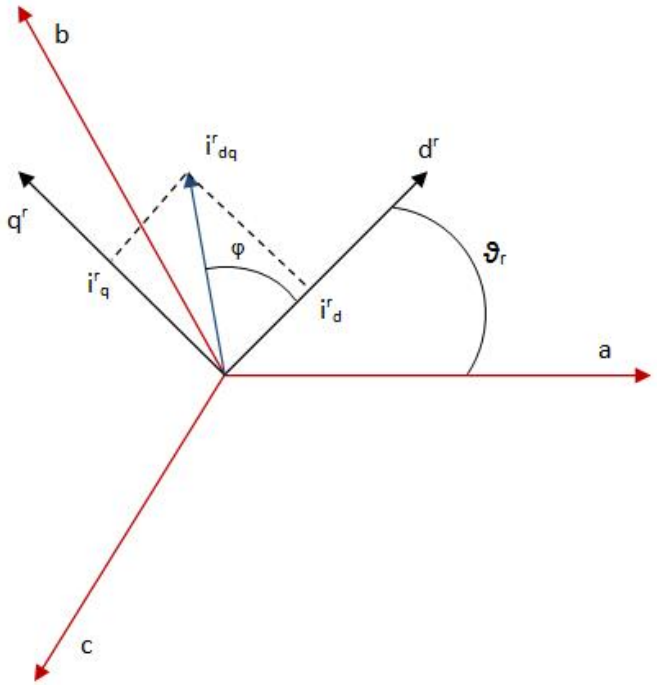

Figure A.2: Vector chart of the current space vector in the synchronous reference frame

Hence, equation A.1 can be rewritten replacing the d-axis and q-axis currents with their expressions given by equation A.2. The result is the following:

$$T_e = \frac{3}{2}P(\Psi_{pm}I\sin\varphi + (L_d - L_q)I\cos\varphi I\sin\varphi) \tag{A.3}$$

The MTPA strategy looks at the angle φ that satisfies the following equation [14]:

$$\frac{dT}{d\varphi} = 0 \tag{A.4}$$

Developing the derivate of equation A.4, the following relationship is obtained:

$$\frac{3}{2}P(\Psi_{pm}I\cos\varphi + (L_d - L_q)I^2(\cos^2\varphi - \sin^2\varphi)) = 0 \tag{A.5}$$

finally yielding to the expression of the q-axis component of the current as a function of the d-axis component that is given by:

$$i_q^r = \pm\sqrt{\frac{\Psi_{pm} i_d^r + (L_d - L_q)(i_d^r)^2}{L_d - L_q}} \tag{A.6}$$

From equation A.1, the d-axis current can be rewritten as a function of the torque and of the q-axis current in the following way:

$$i_d^r = \frac{T_e - 3/2P\Psi_{pm} i_q^r}{3/2P(L_d - L_q) i_q^r} \tag{A.7}$$

Hence the expression of the d-axis current in A.6 can be replaced by A.7 yielding finally to the expression of the q-axis current as a function of the torque commanded to 'Block1':

$$\frac{3}{2}P(L_d - L_q)^2 (i_q^r)^4 + \frac{3}{2}P\Psi_{pm} T_e i_q^r - T_e^2 = 0 \tag{A.8}$$

On the other hand the expression of the d-axis current as a function of the q-axis current is simply given rearranging equation A.6 getting at the end the following equation:

$$(L_d - L_q)(i_d^r)^2 + \Psi_{pm} i_d^r - (L_d - L_q)(i_q^r)^2 = 0 \tag{A.9}$$

that represent the equation on which 'Block2' is based.
Both A.8 and A.9 are non-linear and not easy to manage in Simulink. Polynomial fitting has been used to simplify the implementation, Matlab function 'polyfit' has been used for this purpose. This function finds the coefficients of a polynomial that fits the solutions of the equations A.8 and A.9. The coefficients got from the 'polyfit' of equations A.8 and A.9 have been then inserted in 'Block1' and 'Block2' respectively which contains a Simulink polynomial block. The polynomial order for both equations A.8 and A.9 is eight and the result of the 'polyfit' is presented in figure A.3 for equation A.8 and in figure A.4 for equation A.9. The solutions of the equation A.8 and A.9 are also plotted in figure A.3 and A.4 respectively, and, as it can be appreciated from the figures the function 'polyfit' approximates the respective equations with negligible error.

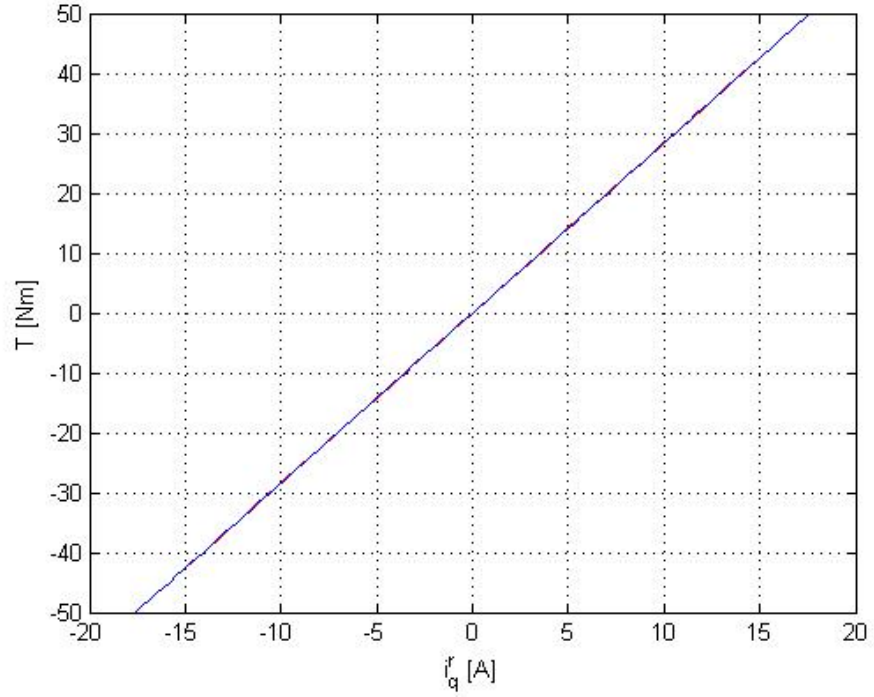

Figure A.3: Torque as a function of the i_q^r current

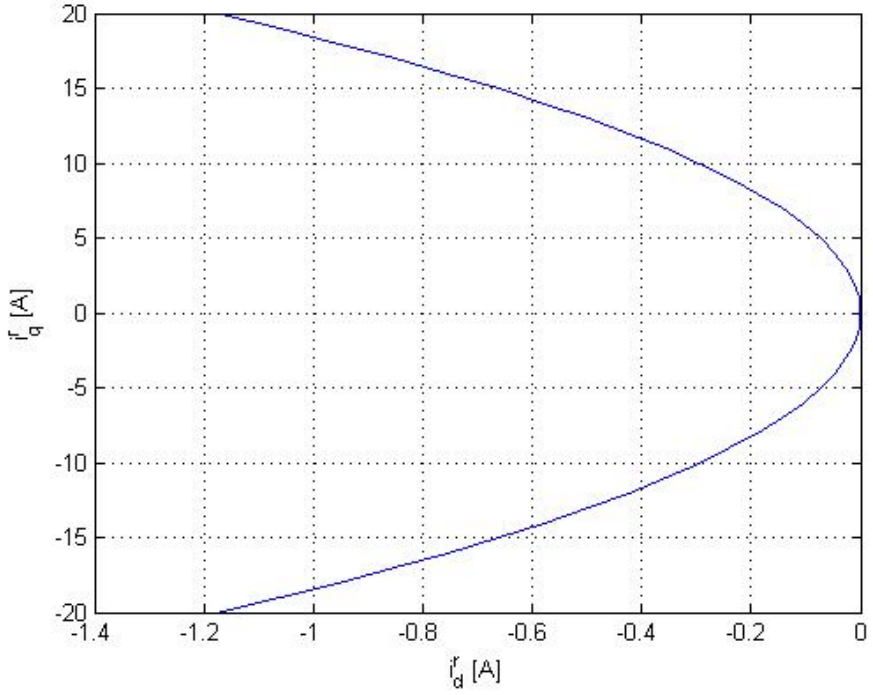

Figure A.4: i_q^r current as a function of the i_d^r current

APPENDIX B

APPENDIX B - Discretization

All the transfer functions implemented in Simulink are in the continuous domain, while the real implementation in the DSP requires it to be discretized. Tustin (bilinear) approximation has been used to transform continuous-time models to discrete-time models and vice versa.The bilinear transformation is a first-order approximation of the natural logarithm function that is an exact mapping of the z-plane to the s-plane. When the Laplace transform is performed on a discrete-time signal (with each element of the discrete-time sequence attached to a correspondingly delayed unit impulse), the result is precisely the Z transform of the discrete-time sequence with the substitution of equation B.1.

$$z = e^{sT} = \frac{e^{sT/2}}{e^{-sT/2}} \approx \frac{1 + sT/2}{1 - sT/2} \tag{B.1}$$

where T is the numerical integration step size of the trapezoidal rule used in the bilinear transform derivation. The bilinear approximation of equation B.1 can be solved for s with the inverse transformation given by equation B.2.

$$\begin{aligned} &s = \tfrac{1}{T} ln(z) = \tfrac{2}{T}\left[\tfrac{z-1}{z+1} + \tfrac{1}{3}\left(\tfrac{z-1}{z+1}\right)^3 + \tfrac{1}{5}\left(\tfrac{z-1}{z+1}\right)^5 + \tfrac{1}{7}\left(\tfrac{z-1}{z+1}\right)^7 + \dots\right] \approx \\ &\approx \tfrac{2}{T}\tfrac{z-1}{z+1} = \tfrac{2}{T}\tfrac{1-z^{-1}}{1+z^{-1}} \end{aligned} \tag{B.2}$$

Some example of the Tustin biliner transformation applied to different continuous-time transfer function in the Laplace domain are now shown:

- Pure integrator:

$$\frac{Output(s)}{Input(s)} = \frac{1}{s} \tag{B.3}$$

Replacing s in equation B.3 with the quantity of equation B.2, equation B.4 (in the discrete domain) is obtained:

$$\frac{Output(z)}{Input(z)} = \frac{1}{\frac{2}{T}\frac{1-z^{-1}}{1+z^{-1}}} = \frac{T}{2}\frac{1+z^{-1}}{1-z^{-1}} \tag{B.4}$$

Yielding

$$Output_k = \frac{T}{2}Input_k + \frac{T}{2}Input_{k-1} + Output_{k-1} \tag{B.5}$$

where k is the considered time step.

- Pure derivative:

$$\frac{Output(s)}{Input(s)} = s \tag{B.6}$$

Replacing s in equation B.6 with the quantity of equation B.2, equation B.7 (in the discrete domain) is obtained:

$$\frac{Output(z)}{Input(z)} = \frac{2}{T}\frac{1-z^{-1}}{1+z^{-1}} \tag{B.7}$$

Yielding

$$Output_k = \frac{2}{T}Input_k - \frac{2}{T}Input_{k-1} - Output_{k-1} \tag{B.8}$$

where k is the considered time step.

- First order LPF:

$$\frac{Output(s)}{Input(s)} = \frac{\omega}{s+\omega} \tag{B.9}$$

where $\omega = 2\pi f_{cut}$.
Replacing s in equation B.9 with the quantity of equation B.2, equation B.10 (in the discrete domain) is obtained:

$$\frac{Output(z)}{Input(z)} = \frac{\omega}{\frac{2}{T}\frac{1-z^{-1}}{1+z^{-1}} + \omega} \tag{B.10}$$

Yielding

$$Output_k = \frac{\omega T}{2+\omega T}Input_k + \frac{\omega T}{2+\omega T}Input_{k-1} - \frac{2-\omega T}{2+\omega T}Output_{k-1} \tag{B.11}$$

where k is the considered time step.

- First order HPF:

$$\frac{Output(s)}{Input(s)} = \frac{s}{s+\omega} \tag{B.12}$$

where $\omega = 2\pi f_{cut}$.
Replacing s in equation B.12 with the quantity of equation B.2, equation B.13 (in the discrete domain) is obtained:

$$\frac{Output(z)}{Input(z)} = \frac{\frac{2}{T}\frac{1-z^{-1}}{1+z^{-1}}}{\frac{2}{T}\frac{1-z^{-1}}{1+z^{-1}}+\omega} = \frac{2(1-z^{-1})}{2(1-z^{-1})+\omega T(1+z^{-1})} \tag{B.13}$$

Yielding

$$Output_k = \frac{2}{2+\omega T}Input_k + \frac{2}{2+\omega T}Input_{k-1} + \frac{2-\omega T}{2+\omega T}Output_{k-1} \tag{B.14}$$

where k is the considered time step.

Bibliography

[1] Yue Zhao; Zhe Zhang; Wei Qiao; Long Wu, "An extended flux model-based rotor position estimator for sensorless control of interior permanent magnet synchronous machines," Energy Conversion Congress and Exposition (ECCE), 2013 IEEE , vol., no., pp.3799,3806, 15-19 Sept. 2013

[2] Silva, C.; Asher, G.M.; Sumner, M., "Hybrid rotor position observer for wide speed-range sensorless PM motor drives including zero speed," Industrial Electronics, IEEE Transactions on , vol.53, no.2, pp.373,378, April 2006

[3] Piippo, A.; Luomi, J., "Adaptive observer combined with HF signal injection for sensorless control of PMSM drives," Electric Machines and Drives, 2005 IEEE International Conference on , vol., no., pp.674,681, 15-15 May 2005

[4] Zhiqian Chen; Tomita, M.; Ichikawa, S.; Doki, S.; Okuma, S., "Sensorless control of interior permanent magnet synchronous motor by estimation of an extended electromotive force," Industry Applications Conference, 2000. Conference Record of the 2000 IEEE , vol.3, no., pp.1814,1819 vol.3, 2000

[5] *US DoE*, Shi, Y. F.; Zhu, Z.Q.; Howe, D., "EKF-based Hybrid Controller for Permanent Magnet Brushless Motors Combining Hall Sensors and a Flux-Observer-based Sensorless Technique," Electric Machines and Drives, 2005 IEEE International Conference on , vol., no., pp.1466,1472, 15-15 May 2005

[6] Vosmik, D.; Peroutka, Z., "Sensorless control of permanent magnet synchronous motor employing extended Kalman filter in combination with HF injection method," Power Electronics and Applications (EPE 2011), Proceedings of the 2011-14th European Conference on , vol., no., pp.1,10, Aug. 30 2011-Sept. 1 2011

[7] Iura, H.; Inazumi, M.; Kamei, T.; Ide, K., "Hybrid sensorless control of IPMSM for direct drive applications," Power Electronics Conference (IPEC), 2010 International , vol., no., pp.2761,2767, 21-24 June 2010

[8] Bolognani, S.; Faggion, A.; Fornasiero, E.; Sgarbossa, L., "Full speed range sensorless IPM motor drives," Electrical Machines (ICEM), 2012 XXth International Conference on , vol., no., pp.2209,2215, 2-5 Sept. 2012

[9] Faggion, Adriano; Bolognani, S.; Bianchi, N., "Ringed-pole permanent magnet synchronous motor for position sensorless drives," Energy Conversion Congress and Exposition, 2009. ECCE 2009. IEEE , vol., no., pp.3837,3844, 20-24 Sept. 2009

[10] Chan-Hee Choi, Bum-Sik Kim, Young-Kook Lee, Jin-Hwan Jung, Jul-Ki Seok, "Experimental Evaluation of Position Sensorless Control on Hybrid Electric Vehicle Applications", Journal of Power Electronics, Vol. 11, No. 4, pp. 464, 470, July 2011

[11] Slides for teaching by Fernando Briz, "Control sin Sensor de Motores de Imanes Permanentes", 03/2012

[12] Slides for teaching by Fernando Briz, "Saliency Tracking-based Sensorless Control of AC Drives", Mondragon Unibertsitatea, 06/06/2013

[13] Fernando Briz, Michael W. Degner, "Rotor Position Estimation", IEEE Industrial Electronics Magazine, 17/06/2011

[14] Slides for teaching by F. Giulii Capponi, "Dynamic Control of AC Machines - Vector control of PM machines", 2011

[15] Notes for lectures of Electric Drives by Silverio Bolognani, a.a. 2004-05

[16] Slides for teaching by Prof. Giuseppe Zollino, Department of electrical Engineering University of Padova - Consorzio RFX, 2011

[17] J. Holtz and J. Juliet, "Sensorless acquisition of the rotor position angle of induction motors with arbitrary stator windings," IEEE Trans. Ind. Applicat., vol. 41, no. 6, pp. 1675-1682, Nov.-Dec. 2005.

[18] Jansen, P.L.; Lorenz, R.D.; Novotny, D.W., "Observer-based direct field orientation: analysis and comparison of alternative methods," Industry Applications Society Annual Meeting, 1993., Conference Record of the 1993 IEEE , vol., no., pp.536,543 vol.1, 2-8 Oct 1993